

High density, On-chip, Alkali Doping of Graphene and the Characterization of the Electronic Structure of Franckeite

Ayşe Melis Aygar



Department of Electrical & Computer Engineering
McGill University
Montréal, Québec, Canada

August 15, 2023

Under the supervision of Professor Thomas Szkopek

A thesis presented to McGill University in partial fulfillment of the requirements for the degree of Doctor of Philosophy.

©2023 Ayşe Melis Aygar

Abstract

This thesis presents contributions to the understanding of the fundamental properties of van der Waals materials, motivated by the long-term goal of developing methods to tune and control the physical properties of van der Waals materials. In the first part of this thesis, a method to alkali dope graphene on-chip in an inert glovebox environment is presented, enabling an electron density of $4 \times 10^{14} \text{ cm}^{-2}$ to be achieved. The method is suitable for charge transport and optical spectroscopy measurements at ultra-high charge carrier density. In our experiments, cesium vapour inside a cavity promotes cesium atom adsorption and ionization at the graphene surface, doping the graphene to ultra-high density levels. At the electron density of $4 \times 10^{14} \text{ cm}^{-2}$ a drop in room temperature mobility to $140 \text{ cm}^2\text{V}^{-1}\text{s}^{-1}$ is recorded, in accord with the effective mass increase. Once doped, graphene can be hermetically sealed to protect against oxidation from the ambient environment, enabling experimental manipulation outside the glovebox environment. This method is substantively more facile than state-of-the-art ultra-high vacuum doping methods. In heavily doped graphene, a large magnetoresistance at low temperature,

$T = 1.3$ K, is attributed to electron density fluctuations. Temperature dependent weak localization reveals the prevalence of trigonal warping, in accord with high electron density. Non-resonant Raman scattering at a $\lambda = 785$ nm pump wavelength independently confirms the high electron density achieved via the dynamic contribution to the Raman G-band shift.

The second part of the thesis presents the experimental characterization of several electronic properties of franckeite, a naturally occurring sulfosalt mineral with a van der Waals superlattice structure composed of alternating incommensurate two-dimensional layers: pseudo-tetragonal PbS and hexagonal SnS₂ layers. Experimental observations of the franckeite atomic structure, using state-of-the-art high-angle annular dark-field (HAADF) scanning transmission electron microscopy (STEM) and atom probe tomography (APT) are presented. Angle-resolved photoemission spectroscopy (ARPES) measurements of the band structure reveal an anisotropic two-valley valence band with in-plane effective mass values, 19.1 and 1.6 m_0 . Optical reflection hyperspectra of exfoliated franckeite is used to determine the direct optical band-gap at $E_g = 1.9 - 2.0$ eV. Thermoelectric measurements of exfoliated franckeite flakes reveal a Seebeck coefficient of $S = +45$ $\mu\text{V}/\text{K}$ and verify the intrinsic carriers to be p-type.

Abrégé

Cette thèse présente des contributions à la compréhension des propriétés fondamentales des matériaux de van der Waals, motivées par un objectif à long terme de contrôle des propriétés physiques. Dans la première partie de cette thèse, une méthode de dopage alcalin du graphène sur puce dans un environnement inerte de boîte à gants est présentée, permettant d'atteindre une densité d'électrons de $4 \times 10^{14} \text{ cm}^{-2}$. Cette méthode convient aux mesures de transport de charge et de spectroscopie optique à une densité de porteurs de charge ultra-élevée. Dans nos expériences, la vapeur de césium à l'intérieur d'une cavité favorise l'adsorption et l'ionisation d'atomes de césium à la surface du graphène, dopant ainsi le graphène à des niveaux de densité ultra-élevés. À une densité d'électrons de $4 \times 10^{14} \text{ cm}^{-2}$, la mobilité à température ambiante chute à $140 \text{ cm}^2\text{V}^{-1}\text{s}^{-1}$, ce qui correspond à l'augmentation de la masse effective. Une fois dopé, le graphène peut être scellé hermétiquement pour le protéger de l'oxydation de l'environnement ambiant, ce qui permet une manipulation expérimentale en dehors de la boîte à gants. Cette méthode est nettement plus simple que les méthodes de dopage sous ultraviolette les plus récentes. Dans le

graphène fortement dopé, une magnétorésistance importante à basse température, $T = 1,3$ K, est attribuée aux fluctuations de la densité électronique. La localisation faible dépendante de la température révèle la prévalence de la déformation trigonale, en accord avec une densité électronique élevée. La diffusion Raman non résonante à une longueur d'onde de pompe de $\lambda = 785$ nm confirme indépendamment la haute densité d'électrons obtenue par la contribution dynamique au décalage de la bande G de Raman.

La deuxième partie de la thèse présente la caractérisation expérimentale de plusieurs propriétés électroniques de la franckeite, un minéral sulfosalte naturel avec une structure de super-réseau de van der Waals composée d'une alternance de couches bidimensionnelles incommensurables : couches pseudo-tétraogonales de PbS et hexagonales de SnS₂. Des observations expérimentales de la structure atomique de la franckeite, utilisant la microscopie électronique à transmission à balayage à champ sombre annulaire à angle élevé et la tomographie par sonde atomique, sont présentées. Les mesures de la structure des bandes par spectroscopie de photoémission résolue en angle révèlent une bande de valence anisotrope à deux vallées avec des valeurs de masse effective dans le plan, soit 19,1 et 1,6 m_0 . L'hyperspectre de réflexion optique de la franckeite exfoliée est utilisé pour déterminer la bande interdite optique directe à $E_g = 1,9 - 2,0$ eV. Les mesures thermoélectriques des flocons de franckeite exfoliée révèlent un coefficient Seebeck de $S = +45$ uV/K et vérifient que les porteurs intrinsèques sont de type p.

Acknowledgements

I am deeply grateful to my supervisor, Professor Thomas Szkopek for his exceptional expertise and unwavering support during the course of my research. His profound knowledge in the field has been instrumental in shaping the direction of this thesis. His guidance has greatly enriched my understanding of the subject matter. I am particularly thankful for his patience and consistent encouragement. His belief in my potential has been a driving force that propelled me forward, even in the face of challenges. His mentorship has not only enhanced my academic growth but has also instilled in me a sense of confidence that extends beyond the scope of my research. I am truly fortunate to have had the privilege of working under his guidance. This thesis is a reflection of not only my efforts but also of his profound influence.

I would like to express my gratitude to Professor Alexander Grüneis for hosting me as a visiting researcher in his lab. His generosity in sharing his lab's resources and insights significantly enriched my research experience. I am thankful for the opportunity to collaborate and learn from his team, which added a valuable dimension to my academic

journey.

I wish to express my gratitude to Professor Gianluigi Botton and Dr. Hannes Zschiesche for their expertise, and the fruitful collaboration which have significantly enriched the quality of this work.

I would like to acknowledge the Polytechnique Montreal Laboratoire de Microfabrication for providing access to their facilities and for the extensive technical support by Christophe Clément and Marie-Hélène Bernier.

I want to express my gratitude to my fellow lab colleagues, particularly Oliver Durnan, Eli Martel and Nicholas Hemsworth. I appreciate them not just for the valuable discussions and teamwork, but also for their friendship.

I would like to express my gratitude to McGill Engineering Doctoral Award (MEDA), Natural Sciences and Engineering Research Council of Canada (NSERC), Fonds de Recherche du Québec Nature et technologies (FRQNT) for funding my research.

Finally, I extend my heartfelt thanks to my family, my partner Arda Balkancı, and my cats. Their unwavering support, and presence have been sources of strength throughout this journey. I am also thankful to my friends Selen Özkan and Buğra Yarkın, who were my dedicated thesis companions despite living across the ocean. Their support, encouragement, and shared challenges have made this undertaking much more manageable and enjoyable.

Contents

1	Introduction	1
1.1	A Brief Review of 2D materials	1
1.2	A Brief Review of 2D Superlattices	6
1.3	Original Contributions	9
1.4	Thesis Outline	13
2	Graphene Review	15
2.1	The Band Structure of Graphene	15
2.2	The Hall effect in Graphene	28
2.3	Magnetoresistance in Graphene	32
2.3.1	Weak Localization in Graphene	34
2.4	Raman Spectroscopy of Graphene	40
2.4.1	Raman G-peak shift	41
3	High-density, On-chip, Alkali Doping of Graphene	44

3.1	Experimental Methods	49
3.1.1	Fabrication of Graphene Hall bar devices	49
3.1.2	The flip-chip method and the experiment setup	50
3.2	Real-time Hall Analysis During Cs Doping	55
3.3	Magnetotransport of Ultra-High Doped Graphene	58
3.3.1	Evidence of Ultra-High Doping	59
3.3.2	Magnetoresistance in Ultra-High Doped Graphene	62
3.3.3	Weak Localization in Ultra-High Doped Graphene	64
3.4	Raman Spectroscopy of Ultra-High Doped Graphene	67
3.5	Conclusion	70
4	Franckeite Review	72
4.1	Crystal Structure of Franckeite	73
4.2	Band Structure of Franckeite	75
4.3	Optical Properties of Franckeite	77
4.4	Charge Transport in Franckeite	79
5	Characterization of the Electronic Structure of Franckeite	81
5.1	Characterization of Franckeite	83
5.1.1	Atom Probe Tomography	83
5.1.2	High-Angle Annular Dark-Field STEM	85

5.1.3	Angle Resolved Photoemission Spectroscopy	89
5.2	Reflectance Hyperspectra of Exfoliated Franckeite	92
5.2.1	Atomic Force Microscopy	92
5.2.2	Optical Reflection Spectroscopy	93
5.3	Thermoelectric Effect in Exfoliated Franckeite	98
5.4	Conclusion	101
6	Conclusions and Future Work	103
	References	108

List of Figures

1.1	2D materials family	2
1.2	Classification of 2D superlattices	7
2.1	Direct and reciprocal lattices of graphene	18
2.2	First-nearest neighbour displacement vectors	19
2.3	Second-nearest neighbour displacement vectors	20
2.4	Third-nearest neighbour displacement vectors	20
2.5	Energy dispersion of graphene	23
2.6	Calculated density of states in graphene	25
2.7	Calculated charge carrier density in graphene	26
2.8	Calculated electron effective mass in graphene	28
2.9	Schematic of an experiment with a Hall bar	30
2.10	The longitudinal and transverse resistivities of graphene	31
2.11	Magnetoresistance due to carrier density inhomogeneity	33

2.12	Weak (anti)localization in graphene	38
2.13	Main Raman features in graphene	40
3.1	Doping monolayer graphene towards the Lifshitz transition	45
3.2	Flip-chip assembly in Apple's smartphone	50
3.3	Schematic of the flip-chip assembly and the doping mechanism	51
3.4	Photograph of the flip-chip assembly and the Hall-bar device	52
3.5	AC Hall measurement configuration	53
3.6	Photographs of a sealed sample	55
3.7	Doping graphene through the CNP	56
3.8	Doping graphene to ultra-high carrier density	57
3.9	Resistivity ρ_{xx} versus T of a representative Cs doped graphene sample.	58
3.10	Confirming ultra-high carrier density via DC Hall	60
3.11	Magnetoresistivity in ultra-high doped graphene	62
3.12	Weak-localization in ultra-high doped graphene	64
3.13	Raman spectroscopy of ultra-high doped graphene	68
4.1	Crystal structure of franckeite	74
4.2	DFT calculated band structure of franckeite	76
4.3	Absorption and photoluminescence spectra of franckeite	78
4.4	Anisotropic electronic transport in franckeite	80

5.1	Atom probe tomography of franckeite	83
5.2	High-angle annular dark-Field STEM of franckeite	86
5.3	HAADF STEM of H and Q layers	87
5.4	Proposed atomic ordering in franckeite layers	88
5.5	Franckeite ARPES	91
5.6	Optical microscopy and AFM images of exfoliated franckeite	93
5.7	Schematic of a hyperspectral imaging system	94
5.8	Reflection hyperspectra images of exfoliated franckeite	95
5.9	Reflectivity of exfoliated franckeite	97
5.10	Temperature dependence of franckeite resistance	99
5.11	Thermoelectric experiments of exfoliated franckeite	100
6.1	AFM images of exfoliated franckeite flakes before and after Cs exposure . . .	107

List of Tables

2.1	3NN-TB parameters	22
3.1	Physical properties of highly doped graphene	59
3.2	Magnetoresistance fit parameters of highly doped graphene	62
3.3	Scattering parameters at different carrier densities	66
3.4	Scattering parameters at different temperatures	67
4.1	Lattice parameters of H and Q layers	74

List of Acronyms

2D	Two-dimensional.
3NN	Third-nearest neighbour.
AFM	Atomic force microscopy.
APT	Atom probe tomography.
ARPES	Angle-resolved photoemission spectroscopy.
DFT	Density functional theory.
HAADF	High-angle annular dark-field.
LEAP	Local electrode atom probe.
PL	Photo-luminescence.
STEM	Scanning transmission electron microscopy.
TB	Tight binding.

Chapter 1

Introduction

1.1 A Brief Review of 2D materials

2D materials are an important category of nanomaterials, and are also known as layered materials, van der Waals materials, or lamellar materials. In a 2D lattice, repeating sheets comprising a single or a few atomic layers that are covalently or ionically bonded in-plane are vertically stacked via van der Waals forces, making 2D materials highly anisotropic. The creation of free-standing graphene and the discovery of its remarkable properties [1] triggered a new era of 2D materials research. The field of research gradually broadened to include, in addition to graphene, hexagonal boron nitride (h-BN), transition metal dichalcogenides (e.g. MoS₂, WSe₂), elemental 2D materials (e.g. black phosphorus, silicene, germanene), graphitic carbon nitride (g-C₃N₄), metal-organic frameworks (MOFs) and

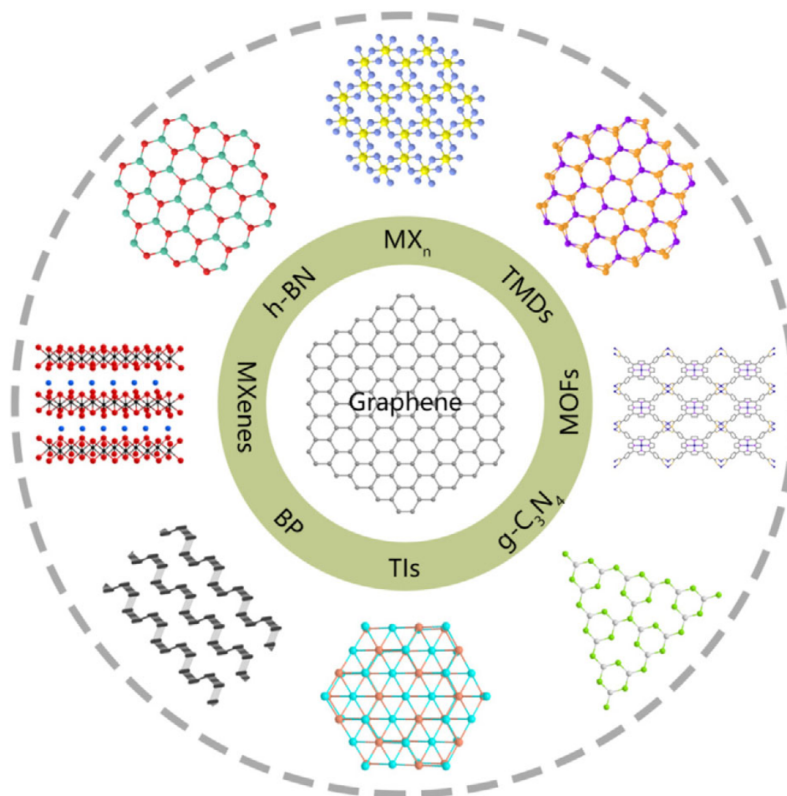


Figure 1.1: Notable examples from the 2D materials family: Graphene, topological insulators (TIs), transition metal dichalcogenides (TMDs), black phosphorus (bP), MXenes, graphitic carbon nitride ($g\text{-C}_3\text{N}_4$), metal organic frameworks (MFOs). Reprinted with permission from Ref [5].

others (see Figure 1.1). 2D materials exhibit different physical, electrical, chemical, magnetic and optical properties, than their 3D counterparts due to the enhancement of surface effects and quantum confinement of charge carriers. Notably, 2D materials have attracted significant interest in the past before monolayer exfoliation and synthesis methods were developed [2–4].

It is relatively easy to isolate small samples of 2D materials from bulk crystals. The

atomic layers that constitute 2D materials are held together by weak van der Waals forces, allowing separation of graphene layers by utilizing merely an adhesive tape [6]. This method is the most primitive form of mechanical exfoliation, which is widely used to achieve good quality single crystalline flakes generally in the order of tens of micrometers in lateral extent. Over time, mechanical exfoliation methods have improved to deliver higher quality, larger and thinner flakes. Recently, researchers have succeeded in exfoliating monolayer graphene flakes up to 1 mm size using metallic layers to cleave selective number of graphene layers [7]. Another approach is liquid-phase exfoliation, where bulk pieces of the material in suspension are agitated with ultrasonic waves. This method provides a good balance between fabrication cost and flake quality [8]. In addition to the top-down methods listed, it is also possible to directly grow large area 2D materials using chemical vapour deposition.

Previous research has established many impressive electronic properties of 2D materials in a variety of applications. Graphene has been established as a material with ultra-high room temperature mobility of $140000 \text{ cm}^2/\text{Vs}$ and ballistic electron transport distances over $15 \mu\text{m}$ [9]. In addition to graphene, transition metal dichalcogenides have been utilized in different electronic applications. A current ON/OFF ratio higher than 10^6 has been recorded for a p-type field effect transistor with a monolayer WSe_2 channel [10]. MoS_2 channel computing cell has demonstrated photoswitching AND/OR logic computing in a single cell, achieving higher area efficiency compared to traditional logic gates with 2 transistors [11]. Other representative examples of the state-of-art electronic devices incorporating 2D materials

include MoS₂ transistors with 1 nm channel length [12], ultra-fast non-volatile memory in van der Waals heterostructures [13, 14]. Most recently, InSe FET have been demonstrated with excellent sub-threshold swing, contact resistance and current density performance [15]. 2D materials are available not only with metallic or semiconducting behaviour but also in insulating forms. h-BN layers have been proposed as a high- κ gate dielectric to gate graphene channels [16] to achieve fully two-dimensional transistor systems. Furthermore, 2D material interfaces with appropriately matched substrates exhibit superconductivity: a critical temperature above 100 K have been recorded for monolayer FeSe on SrTiO₃ substrate [17].

Interesting properties of 2D materials are not limited to electronics. Optical properties of 2D materials have been investigated extensively. Monolayer MoS₂ has a direct band gap and higher photoluminescence by a factor of 10^4 , compared to its bulk form with an indirect gap [18]. As a result, graphene/MoS₂ photodetectors have demonstrated photogain higher than 10^8 [19]. WSe₂ solar cells with graphene electrodes have shown comparable power conversion efficiency to prevailing thin-film solar cells with the added benefits of being lightweight and flexible [20].

Tunability of 2D materials enables engineering their various properties. It is possible to modulate the band gap of 2D materials by modifying the number of layers, applying electric field or strain. In fact, phosphorene has a layer dependent direct band gap that allows optical transitions in the spectral range from the visible to the mid-infrared [21]. Additionally, the

giant Stark effect, which is the shifting of energy levels due to applied electric fields, has been recorded in phosphorene [22]. Furthermore, in Fe_3GeTe_2 flakes, gate-tunable ferromagnetism has been observed [23]. Large surface area to volume ratio of 2D materials makes them more sensitive to surface effects compared to bulk materials. As a result, 2D material surfaces are effective mediums for electrochemical sensing [24]. Functionalization of 2D materials, enables fine tuning of the surface chemistry to engineer selective membranes for chemical or bio sensing applications.

Doping is a widely utilized strategy to tune the electrical properties of materials for applications or to investigate the fundamental properties of charge carriers. In 3D semiconductors, doping is achieved through dopant diffusion or ion implantation into the bulk crystal. However, for 2D materials, distinct doping approaches are required due to their reduced dimensionality. Electrochemical and electrostatic gating are commonly used to dope 2D materials. Additionally, the heightened surface sensitivity of 2D materials allows effective doping through dopant adsorption onto the surface [25, 26]. Furthermore, the weak van der Waals bonding between atomic layers in 2D materials allows for a unique doping method involving the intercalation of dopants between the individual layers. Reversible intercalation of lithium in bilayer and the kinetics of Li diffusion within graphene layers have been reported [27]. A combination of intercalation and adsorption allowed researchers to dope graphene on both sides, to access superconducting states near the M point [28]. More recently, remote doping of MoS_2 through a stacked 2D

heterostructure have been proposed to suppress Coulomb scattering from charged impurities [29].

2D materials exhibit weak substrate interactions because they couple to the substrates via van der Waals forces, without any dangling bonds on the interface. Therefore, 2D materials are far more flexible than compound semiconductors with lattice matching requirements to the substrate. It is possible to fabricate various 2D material/substrate systems and even stack different 2D materials on top of each other to create heterostructures and superlattices. Next section presents an overview of 2D superlattices and their applications.

1.2 A Brief Review of 2D Superlattices

The term superlattice was first used for bulk semiconductor systems with a periodic potential in one direction. The periodic potential is achieved by alternating the material type or the doping levels of the layers. In such a system, if the periodicity is smaller than the electron mean free path, electrons would tunnel through the potential barriers thereby creating new energy bands. Esaki and colleagues have been the first to grow a 50 layer $\text{Al}_x\text{Ga}_{1-x}\text{As}$ superlattice with a periodicity of 100 Å via molecular beam epitaxy and observe nonlinear transport with negative resistance regions experimentally [30, 31]. Later, researchers have employed superlattices for a wide array of applications including GHz oscillators [32], THz detectors [33], quantum cascade lasers [34] and high thermopower materials [35].

Creating superlattices using 2D materials introduces fresh opportunities for investigating

fundamental physics of confined charge carriers and engineer novel materials with desirable band structures. 2D superlattices can be mainly categorized in five classes: vertically stacked, intercalation compounds, moire patterned, strain engineered and lithographically engineered [36] as shown in Figure 1.2.

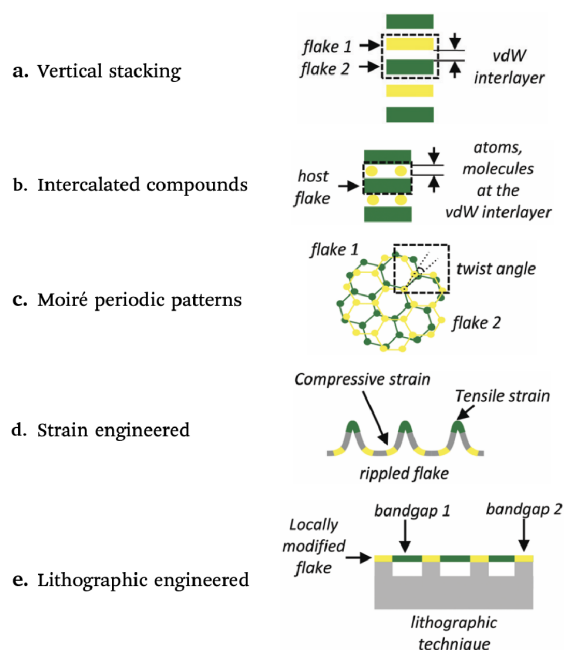


Figure 1.2: Classification of 2D superlattices. (a) Vertical stacking of different 2D layers. (b) Intercalation compounds. (c) Moiré structures by twisting two 2D layers. (d) Strain-engineered layers by applying periodic strains. (e) Lithographic engineered structures by placing 2D material on a patterned topography. Reprinted with permission from Ref [36].

The first approach (Figure 1.2a) is analogous to 3D multiple quantum well structures, where different 2D species are stacked in a vertical repeating pattern to create a periodic potential. In 3D superlattices, the layered species have to be lattice matched due to covalent bonding in order to preserve the crystalline structure. However, in 2D superlattices, any

combination of 2D layers can be used due to their weak interlayer interactions. The process of creating vertically stacked superlattices can be laborious, involving manually picking up and stacking individual exfoliated layers using adhesive tape or PDMS. To streamline this process, one research group has developed an autonomous robotic system capable of locating and stacking individual layers, enabling the fabrication of complex h-BN/graphene superlattices with up to 29 layers [37]. Additionally, it is possible to grow stacked 2D superlattices using molecular beam epitaxy [38]. A unique approach to creating 2D superlattices is by rolling up few layer van der Waals heterostructures to form higher order counterparts [39]. Alternatively, there are natural van der Waals superlattices, such as cylindirite and franckeite [40], which can be mined in bulk form. It is possible to simply mechanically exfoliate such materials to achieve single-crystalline flakes.

Another category of 2D superlattices are known as intercalation compounds (Figure 1.2b). Intercalation is the process of adatoms diffusing in between the layers of a van der Waals material. The adatoms self order and form layers in between host crystal layers, thus a 2D superlattice with a periodic potential emerges. The most well known of this class are the graphite intercalation compounds, in which alkali adatoms are intercalated into a graphite host crystal [41]. Intercalated superlattices have been proposed for different applications. Intercalating organic molecules into TiS_2 crystals, researchers have achieved high power factor flexible thermoelectric materials [42]. Additionally, K intercalated graphite [43] and Li intercalated MoS_2 /graphene [44] superlattices have been developed for energy storage

applications.

2D moiré superlattices arise from the arrangement of two or more 2D layers at a specific twist angle (Figure 1.2c). These layers can be of the same species or different species. When the twist angle is small and the lattices of the stacked layers are similar, a unique long-wavelength superlattice pattern with tunable band structure characteristics is created. The interaction between twisted layers may result in charge redistribution and structural effects such as ripples, which contribute to the emergence of a new band structure. The most well studied 2D moiré superlattice is the twisted bilayer graphene. By adjusting the twist angle, it is possible to engineer the band structure such that the van Hove singularities become accessible at lower Fermi energies compared to pristine monolayer graphene [45]. Unconventional superconductivity due to band flattening near the van Hove singularities have been observed in this system [46]. Another notable example is the twisted h-BN/graphene moiré superlattice which enabled the experimental observation of Hofstadter's butterfly [47], a fractal energy spectrum that arises due to the interplay between discrete energy levels of the superlattice and Landau levels.

1.3 Original Contributions

In this thesis, the following original contributions are reported.

- **A new methodology to alkali dope graphene devices in a N₂ glovebox**

environment. The method, called the flip-chip method, involves a graphene Hall bar device fabricated using lithography methods being exposed to Cs vapour inside a glovebox. A home-built electromagnet integrated to the doping setup, allows real-time carrier density and Hall mobility measurements as graphene is more and more alkali doped. Heavy electron density levels up to $4 \times 10^{14} \text{ cm}^{-2}$ is achieved using the flip-chip method. The Cs doped samples can be sealed afterwards to allow further experiments of doped graphene.

- **Experimental observations of magnetotransport and Raman spectroscopy in heavily alkali doped graphene.** Transport experiments of heavy doped graphene Hall bar devices with carrier densities between $1.4 - 4 \times 10^{14} \text{ cm}^{-2}$ is presented. A large magnetoresistance at low temperature is attributed to electron density fluctuations in heavily doped graphene. Doping density dependent weak localization reveals the prevalence of trigonal warping.
- **Experimental observations of franckeite crystal structure.** Atomic structure measurement using high-angle annular dark-field scanning transmission electron microscopy and atom probe tomography of exfoliated franckeite is carried out.
- **Thermoelectric experiments of exfoliated franckeite.** Thermoelectric experiments were conducted on exfoliated franckeite flakes on SiO_2/Si substrate. Metallic heater, thermometers and electrical contacts are patterned onto the

franckeite flakes via electron beam lithography to measure the temperature gradient and the induced voltage across the material. A p-type Seebeck coefficient $S=+45 \mu\text{V}/\text{K}$, which is significantly smaller than reported for PbS and SnS₂, is observed.

- **Reflection hyperspectra of franckeite.** Exfoliated franckeite flakes on SiO₂/Si are analyzed by AFM and optical reflection hyperspectral images were acquired. Optical response in areas with varying flake thicknesses is presented. A transition from absorption dominated response to interference dominated response occurs at a direct optical absorption edge $E_g= 1.91\text{-}2.0 \text{ eV}$.

The work presented in this thesis resulted in the following publications, submissions and presentations.

1. H. Zschiesche, A. M. Aygar, B. Langelier, T. Szkopek, and G. A. Botton, "Atomic scale chemical ordering in franckeite-a natural van der Waals superlattice," *Journal of Physics: Condensed Matter*, vol. 34, no. 5, pp. 055403, 2021.

- A. M. Aygar and T. Szkopek proposed the research idea and made contributions to the manuscript.
- A. M. Aygar prepared franckeite flakes by mechanical exfoliation under the supervision of T. Szkopek.
- B. Langelier provided technical services for STEM and APT

-
- H. Zschiesche conducted the STEM and APT experiments, performed data analysis and wrote the manuscript under the supervision of G. A. Button.
2. A. M. Aygar, O. Durnan, A. Grüneis, and T. Szkopek, “Ultra-high charge carrier density in monolayer graphene by integrated flip-chip alkali doping.” *Under review.*
- A. M. Aygar fabricated the devices, conducted the doping experiments, transport and Raman measurements and conducted the data analysis under the supervision of T. Szkopek.
 - O. Durnan designed and assembled the electromagnet used in doping experiments and contributed to the doping experiments.
 - A. Grüneis provided expertise on alkali doping.
 - A. M. Aygar and T. Szkopek wrote the manuscript.
3. A. M. Aygar, A. Grüneis, T. Szkopek, “Seebeck coefficient of exfoliated franckeite flakes.” *In preparation*
- A. M. Aygar fabricated the franckeite devices, conducted the atomic force microscopy, the thermoelectric experiments and all data analysis under the supervision of T. Szkopek
 - F. Poirier conducted optical reflection hyperspectral measurements.
 - T. Szkopek and A. Grüneis collected nano-ARPES and nano-XPS measurements

at the SOLEIL Antares beamline.

- A. M. Aygar and T. Szkopek are in the process of preparing the manuscript.

1.4 Thesis Outline

The structure of this thesis is explained below.

Chapter 2: A review of concepts related to the electronic properties of graphene is presented. Electronic band structure of graphene is calculated using a third-nearest neighbour tight-binding model. Transport phenomena such as the Hall effect, magnetoresistance and weak-localization effect are discussed.

Chapter 3: Original work on an integrated flip-chip method to dope graphene by alkali vapour, suitable for charge transport measurements at ultra-high charge carrier density is introduced. Non-resonant Raman scattering independently confirms the high electron density achieved. Transport characteristics of heavily doped graphene samples are presented. A large magnetoresistance at low temperature is attributed to electron density fluctuations in heavily doped graphene. Scattering lengths extracted from the weak-localization are presented with respect to doping density and temperature. Doping density dependent weak localization reveals the prevalence of trigonal warping.

Chapter 4: A review of franckeite, a natural van der Waals material is presented and

literature regarding its crystal structure, and DFT calculations of its band structure are discussed. Previous optical spectroscopy, photoluminescence and charge transport experiments are reviewed.

Chapter 5: Original work on the characterization of franckeite electronic structure is presented. Atomic structure measurement using high-angle annular dark-field scanning transmission electron microscopy and atom probe tomography provide information about the crystal structure of franckeite, including refinements to the structure of the Q- and H-layers and chemical ordering effects. Additionally, optical reflection hyperspectra of exfoliated franckeite is used to determine the direct optical band-gap. Effective mass estimations from angle-resolved photoemission spectroscopy experiments are presented. Lastly, the Seebeck coefficient and intrinsic charge carrier type are determined from thermoelectric measurements of exfoliated franckeite flakes.

Chapter 6: A summary and synthesis of the main findings and outcomes of the research are presented. The implications of the results, as well as the limitations and suggested future research are explained.

Chapter 2

Graphene Review

Since Novoselov and Geim were awarded the 2010 Nobel Prize in physics [48, 49]. for their experimental findings on graphene, there has been significant interest in exploring the different characteristics of this material. Nevertheless, well before their ground-breaking work, theories regarding the electronic structure of graphene had already been established. This chapter provides a brief overview of the relevant electronic properties of graphene as a prelude to the original experimental work presented in Chapter 3.

2.1 The Band Structure of Graphene

Graphene, a single atomic layer of graphite, has a 2D hexagonal lattice composed of carbon atoms. In the atomic plane, carbon atoms are bonded together with single $C - C$ bonds. Each carbon atom forms three σ bonds with the neighbouring atoms through the overlap of

sp^2 hybridized orbitals. One half filled p orbital of each carbon, perpendicular to the atomic plane, form a π band with the neighbouring atoms.

The band structure of graphene was first calculated using a tight binding approximation by Wallace in 1947 [50] followed by Slonczewski and Weiss in 1958 [51] with the purpose of understanding the electronic properties of graphite. At the time the isolation of a single layer of graphene was out of question yet they predicted that this single layer of graphite was a semimetal with valence and conduction bands touching at the corners of the Brillouin zone and the band dispersion had the shape of cones near these points.

The tight-binding method is a relatively simple and computationally efficient method for calculating band structures. It relies on the assumption that the electrons in the deep atomic orbitals are “tightly bound” to the nuclei and therefore their interactions with the rest of the lattice are ignored. It is also assumed that the individual atomic orbitals in the lattice interact or overlap with other orbitals minimally. Like any approximation, the tight-binding approach has its limitations. It doesn’t accurately describe materials where long-range or electron-electron interactions are significant. Furthermore, it may be challenging to choose the right basis orbitals and hopping parameters for systems with complex crystal structures. Nevertheless, in the scope of this thesis the tight-binding method serves as a reliable tool to estimate the band structure of the simple graphene lattice.

To calculate the band structure using the tight-binding method, one begins by defining the crystal lattice unit cell and specifying the atomic positions of the basis and the

neighbouring atoms. Then, the relevant basis orbitals are chosen, and hopping and overlap integrals between neighbouring atoms are determined. Hopping integrals quantify the strength of the electron hopping between atomic sites, similarly, overlap integrals quantify the strength of the overlap between neighbouring electron wavefunctions. Using this information, a transfer matrix and an overlap matrix are constructed. Bloch's theorem is applied to simplify the problem to an eigenvalue problem in the following form [52],

$$H(\mathbf{k})c(\mathbf{k}) = S(\mathbf{k})E(\mathbf{k})c(\mathbf{k}) \quad (2.1)$$

where \mathbf{k} is the electron wave-vector, and $H(\mathbf{k})$ and $S(\mathbf{k})$ are the transfer and overlap matrices, respectively. The eigenvectors in $c(\mathbf{k})$ describe the electron wavefunctions and the eigenvalues $E(\mathbf{k})$ are the energies.

In its simplest form, the tight-binding method assumes that each electron only interacts with the first-nearest neighbour in the lattice. For a more complete picture, second-nearest or third-nearest neighbours can be taken into account. Another commonly applied simplification is ignoring the effects of overlap.

In this thesis, we follow a semi-empirical approach to estimate the band structure of graphene using a third-nearest neighbour tight-binding calculation. We use the hopping and overlap parameters determined from fits to ARPES measurements of graphene by Grüneis et al [52]. The unit cell of the graphene lattice consists of two carbon atoms labelled A and

B and it is shown with the dashed line in Figure 2.1a. \mathbf{a}_1 and \mathbf{a}_2 are the primitive vectors of the direct lattice and the lattice constant $a_0 = |\mathbf{a}_1| = |\mathbf{a}_2| = \sqrt{3}a_{C-C}$, where a_{C-C} is the length of the carbon-carbon bond, 1.42 Å. \mathbf{b}_1 and \mathbf{b}_2 are the primitive vectors of the reciprocal lattice.

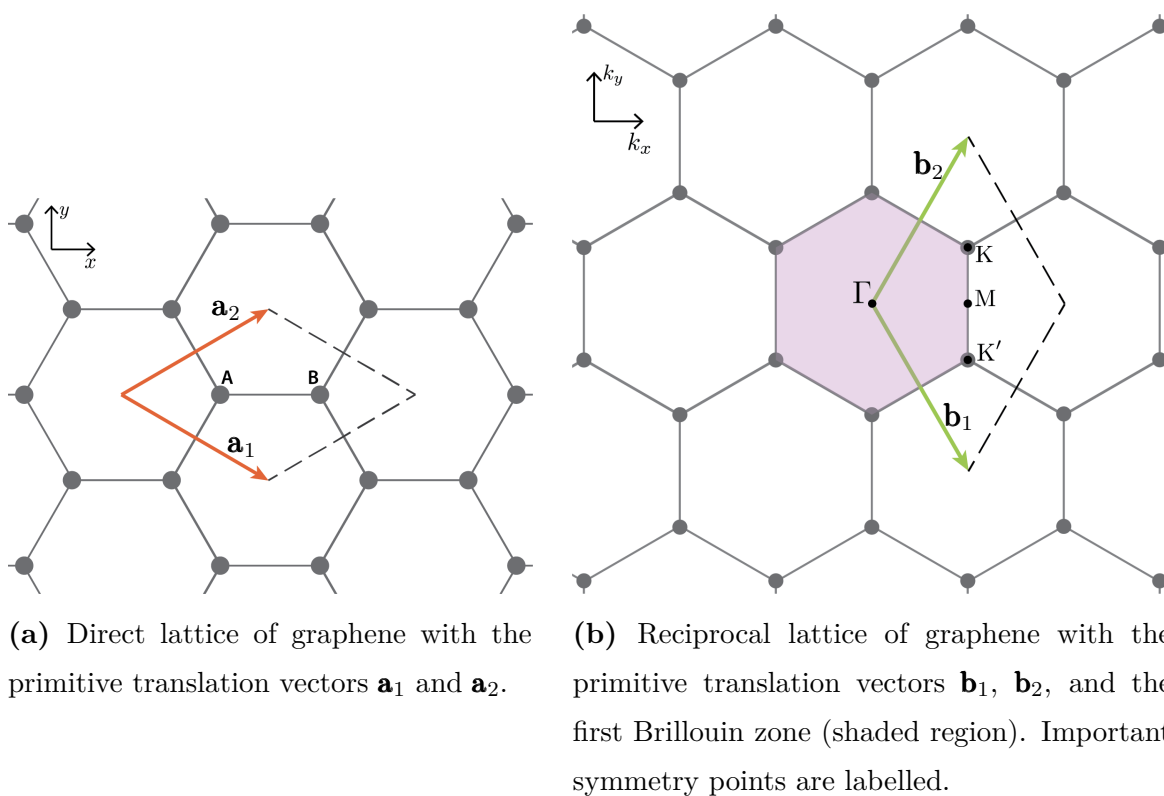


Figure 2.1: Direct and reciprocal lattices of graphene. Dashed lines define the unit cells.

$$\begin{aligned}
 \mathbf{a}_1 &= \left(\frac{\sqrt{3}}{2}, -\frac{1}{2}\right) a_0 & \Rightarrow & \mathbf{b}_1 = \frac{2\pi}{a_0} \left(\frac{1}{\sqrt{3}}, -1\right) \\
 \mathbf{a}_2 &= \left(\frac{\sqrt{3}}{2}, \frac{1}{2}\right) a_0 & & \mathbf{b}_2 = \frac{2\pi}{a_0} \left(\frac{1}{\sqrt{3}}, 1\right)
 \end{aligned}
 \tag{2.2}$$

The Brillouin zone (shaded region in Figure 2.1b) is the Wigner-Seitz primitive cell in the

reciprocal lattice constructed using the 6 directions: \mathbf{b}_1 , \mathbf{b}_2 , $\mathbf{b}_1 + \mathbf{b}_2$, $-\mathbf{b}_1$, $-\mathbf{b}_2$, $-\mathbf{b}_1 - \mathbf{b}_2$.

The wavevectors of the important symmetry points labelled in Figure 2.1b are listed below.

$$\mathbf{b}_\Gamma = (0, 0)$$

$$\mathbf{b}_K = \frac{2\pi}{a_0} \left(\frac{1}{\sqrt{3}}, \frac{1}{3} \right)$$

$$\mathbf{b}_{K'} = \frac{2\pi}{a_0} \left(\frac{1}{\sqrt{3}}, -\frac{1}{3} \right)$$

$$\mathbf{b}_M = \frac{2\pi}{a_0} \left(\frac{1}{\sqrt{3}}, 0 \right)$$

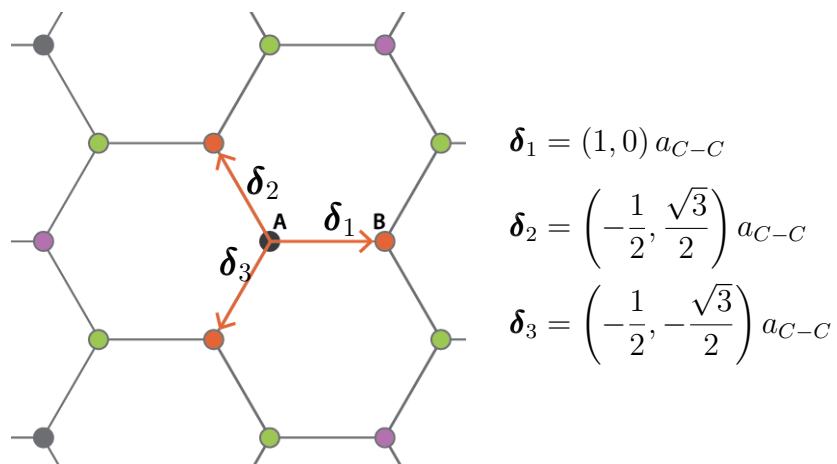


Figure 2.2: First-nearest neighbour displacement vectors

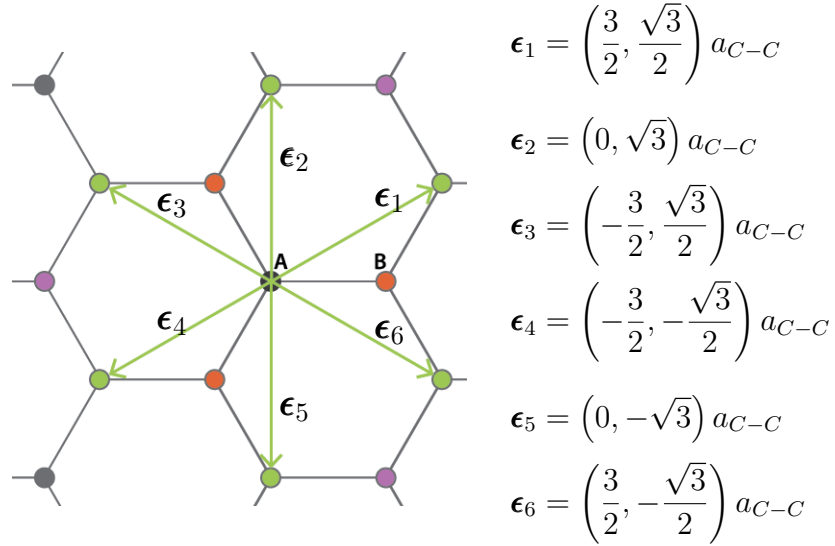


Figure 2.3: Second-nearest neighbour displacement vectors

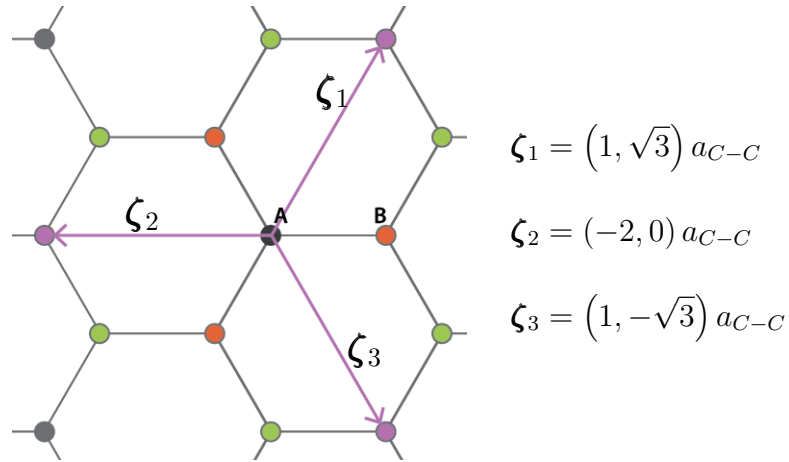


Figure 2.4: Third-nearest neighbour displacement vectors

The displacement vectors for first-, second- and third-nearest neighbours are illustrated in Figures 2.2, 2.3 and 2.4 respectively. $f_1(\mathbf{k})$, $f_2(\mathbf{k})$ and $f_3(\mathbf{k})$ are the displacement phase factors for the first-, second-, and third-nearest neighbours, calculated using the displacement

vectors.

$$f_1(\mathbf{k}) = \sum_{n=1}^3 \exp(i\mathbf{k} \cdot \boldsymbol{\delta}_n) \quad (2.3a)$$

$$f_2(\mathbf{k}) = \sum_{n=1}^6 \exp(i\mathbf{k} \cdot \boldsymbol{\epsilon}_n) \quad (2.3b)$$

$$f_3(\mathbf{k}) = \sum_{n=1}^3 \exp(i\mathbf{k} \cdot \boldsymbol{\zeta}_n) \quad (2.3c)$$

In graphene, the electronic states close to the Fermi level primarily originate from the π band, which means we can focus solely on the $2p_z$ orbitals of each carbon atom in the unit cell. Using the displacement factors, the on-site energy (E_0) and the hopping parameters ($\gamma_1, \gamma_2, \gamma_3$) the transfer matrix is constructed as,

$$H(\mathbf{k}) = \begin{bmatrix} H_{AA} & H_{AB} \\ H_{BA} & H_{BB} \end{bmatrix} = \begin{bmatrix} E_0 + \gamma_2 f_2(\mathbf{k}) & \gamma_1 f_1(\mathbf{k}) + \gamma_3 f_3(\mathbf{k}) \\ \gamma_1 f_1^*(\mathbf{k}) + \gamma_3 f_3^*(\mathbf{k}) & E_0 + \gamma_2 f_2^*(\mathbf{k}) \end{bmatrix}. \quad (2.4)$$

Similarly, the overlap matrix is constructed using the displacement factors and the overlap parameters (s_1, s_2, s_3).

$$S(\mathbf{k}) = \begin{bmatrix} S_{AA} & S_{AB} \\ S_{BA} & S_{BB} \end{bmatrix} = \begin{bmatrix} 1 + s_2 f_2(\mathbf{k}) & s_1 f_1(\mathbf{k}) + s_3 f_3(\mathbf{k}) \\ s_1 f_1^*(\mathbf{k}) + s_3 f_3^*(\mathbf{k}) & 1 + s_2 f_2^*(\mathbf{k}) \end{bmatrix} \quad (2.5)$$

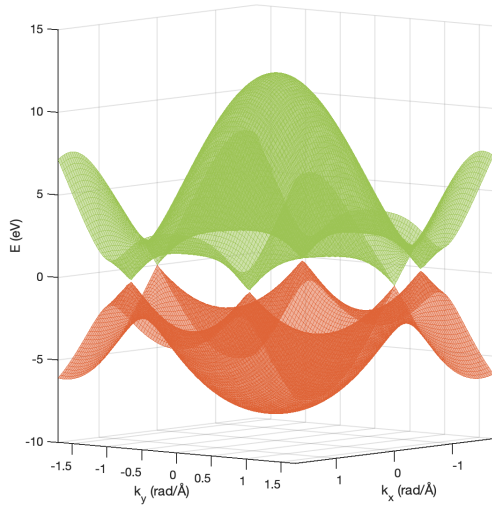
The on-site energy, hopping parameters and overlap parameters from Grüneis et al. [52] are given in Table 2.1. Inserting equations 2.4 and 2.5 into equation 2.1 and solving for the

eigenvalues, $E(\mathbf{k})$, in the first Brillouin zone gives the dispersion relation of the two graphene bands.

E_0 (eV)	γ_1 (eV)	γ_2 (eV)	γ_3 (eV)	s_1	s_2	s_3
-2.2624	-3.4416	-0.7544	-0.4246	0.2671	0.0494	0.0345

Table 2.1: 3NN-TB parameters used in our calculations determined by Grüneis et al. [52] by fitting graphene bands to ARPES data.

We utilize a Matlab code to construct the reciprocal lattice mesh and calculate the corresponding energies. Figure 2.5 illustrates the calculated band dispersion of graphene, as a 3D surface plot as well as cuts in various directions. The surface plot illustrates the touching valence and conduction bands at the vertices of the hexagonal Brillouin zone, corresponding to the charge neutral condition of graphene, which we take as the reference point for energy $E = 0$. Near neutrality, the dispersion is shaped as circular cones centered at the K and K' points, giving rise to massless Dirac fermions, which have been extensively investigated [53, 54].



(a) 3D surface plots of the graphene bands

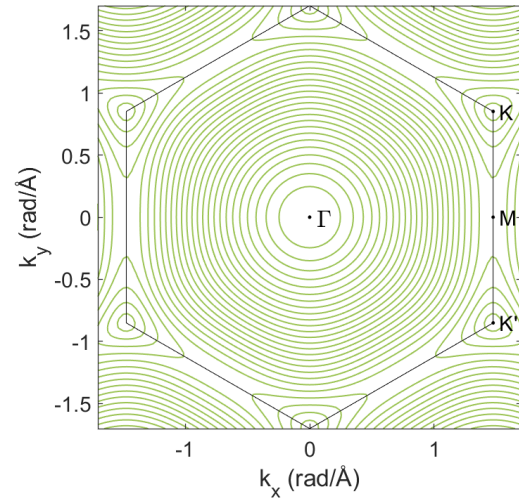
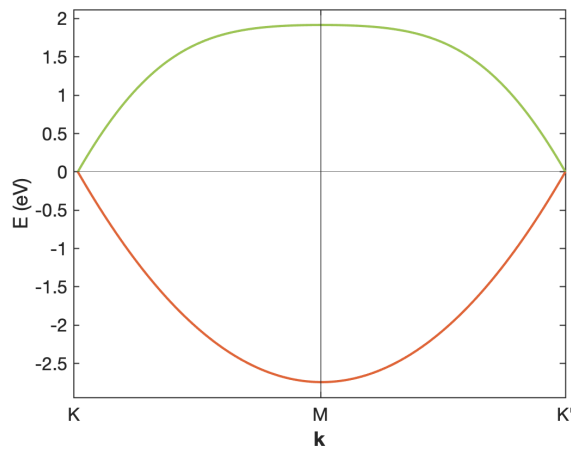
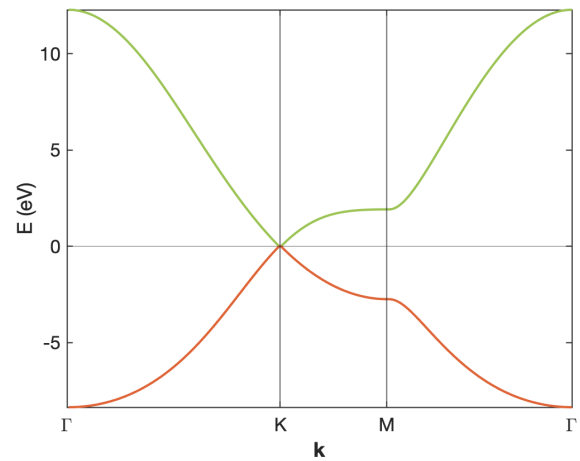
(b) Contour plot of the projection of the conduction band onto the k_x - k_y plane. Black lines represent the edges of the Brillouin zone.(c) Energy dispersion in the K - M - K' direction(d) Energy dispersion in the Γ - K - M - Γ directions

Figure 2.5: Energy dispersion of graphene calculated using a third-nearest neighbour tight-binding method. In each plot, green and orange correspond to conduction and valence bands, respectively.

As the Fermi level moves away from neutrality towards higher energies, the conical bands exhibit trigonal warping as seen in Figure 2.5b. Further away from neutrality, interesting physics emerges near the M point. The bands flatten (Figure 2.5c), leading to a heavier effective mass. The M point is a saddle point, causing a sudden change in the Fermi surface from describing electron pockets to hole pockets, known as a Lifshitz transition (2.5b). Various physical properties are sensitive to changes in the Fermi surface geometry, including charge transport, optical transitions, and Raman scattering. Moreover, the M point is associated with a van Hove singularity (vHS) in the electronic density of states. vHS corresponds to a divergence in the density of states, and in the specific case of a saddle point in two dimensions the divergence scales as $\ln|E - E_M|$ [55], that results in enhanced electronic, optical response and many body effects. More detailed insights into the physics near the M point will be discussed in Chapter 3, focusing on ultra-high doped graphene.

We can extract the density of states, carrier density and effective mass from the dispersion relation. The density of states is defined as,

$$\text{DOS}(E) = \frac{\partial N(E)}{\partial E} \frac{1}{L_x L_y} \quad (2.6)$$

where $N(E)$ is the number of accessible states per unit area $L_x L_y$ with an energy $E' < E$. In our calculations, we extract the density of states numerically using the $E(k_x, k_y)$ matrix we constructed earlier. We count the number of accessible states per unit area, including

the spin degeneracy factor of 2.

$$N(E) = \frac{2A_k(E)}{\Delta k_x \Delta k_y} \quad (2.7)$$

where A_k is the area in the reciprocal space subtended by the iso-energy contour at energy E and $\Delta k_i = 2\pi/L_i$ is the unit spacing in k-space along direction i . The density of states (Figure 2.6) is numerically calculated per unit energy ΔE via,

$$\text{DOS}(E) = \frac{N(E + \Delta E) - N(E)}{\Delta E} \left(\frac{\Delta k_x}{2\pi} \frac{\Delta k_y}{2\pi} \right). \quad (2.8)$$

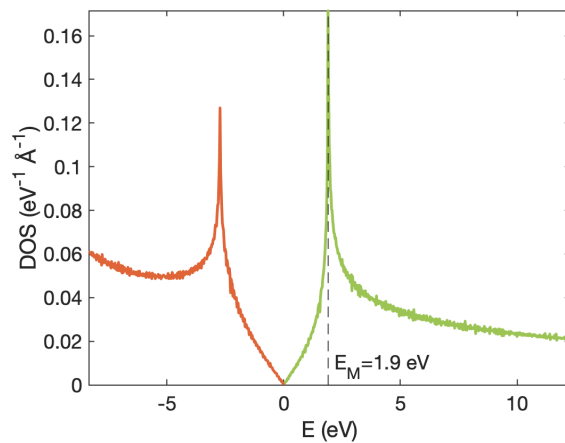


Figure 2.6: Calculated density of states in graphene showing the divergence at the M point, $E_M = 1.9$ eV. Green and orange correspond to conduction and valence bands respectively.

We now turn our attention to the experimentally measurable quantity, the charge carrier density. Assuming all accessible states at $E < E_F$ are occupied and all other states are empty, charge carrier density is the sum of the density of states up/down to the Fermi

energy E_F (Figure 2.7).

$$n(E_F) = \sum_0^{E_F} \text{DOS}(E) \quad , \text{ for electrons} \quad (2.9)$$

$$n(E_F) = \sum_{E_F}^0 \text{DOS}(E) \quad , \text{ for holes}$$

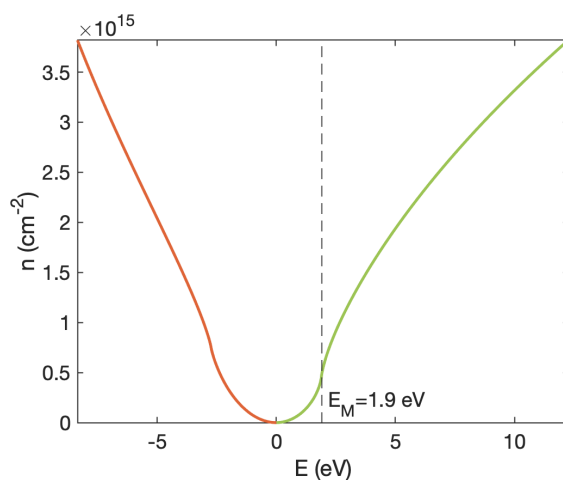


Figure 2.7: Calculated charge carrier density in graphene. Green and orange correspond to electron and hole concentrations respectively. Carrier density at the M point is $n(E_M) = 4.7 \times 10^{14} \text{ cm}^{-2}$. For reference, carbon atom density in graphene is $n_C = 3.82 \times 10^{15} \text{ cm}^{-2}$.

The majority of research regarding the electronic properties of graphene work with energies near neutrality and therefore use a linear dispersion relation, $E = v_F \hbar k$ for the effective mass calculations, where $v_F = 10^6 \text{ m/s}$ is the Fermi velocity. The focus of Chapter 3 of this thesis is ultra-high doped graphene, in which Fermi energies are getting closer to the M point. Therefore, a linear dispersion approximation is not applicable. It is suitable to calculate the effective mass of an isotropic material with an arbitrary dispersion relation

using the cyclotron mass as proposed by [56]. Cyclotron mass is defined as [57],

$$m^*(E) = \frac{\hbar^2}{2\pi} \left(\frac{\partial A_k(E)}{\partial E} \right) \quad (2.10)$$

From the density of states calculations we can extract $\partial A(E)/\partial E$ by using equations 2.6 and 2.7.

$$\text{DOS}(E) = \frac{\partial}{\partial E} \left(\frac{2A_k(E)}{\Delta k_x \Delta k_y} \right) \frac{\Delta k_x}{2\pi} \frac{\Delta k_y}{2\pi} \quad (2.11)$$

Thus, we can write effective mass in terms of the density of states correcting for a valley degeneracy factor of 2 (at K and K') as,

$$m^*(E) = \hbar\pi \frac{\text{DOS}(E)}{2}. \quad (2.12)$$

Figure 2.8 shows the calculated electron effective mass for energies up to the M point. At higher energies, the linear dispersion approximation no longer holds. As expected, electrons start to become massive near the M point, due to the divergence of the density of states and band flattening.

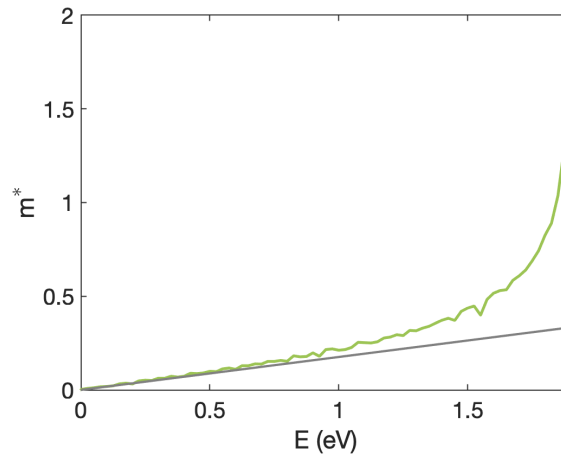


Figure 2.8: Calculated electron effective mass in graphene. The green curve represents the calculated cyclotron electron effective mass of graphene. Gray line shows the effective mass with the linear dispersion approximation.

2.2 The Hall effect in Graphene

The Hall effect is a fundamental phenomenon in condensed matter physics that occurs when a conducting material is subjected to a magnetic field applied orthogonal to the charge carrier velocity. It is an essential tool for studying charge carrier transport in various materials. The experiments presented in Chapter 3 utilize Hall measurements to detect the majority carrier type and estimate the carrier concentration and mobility.

In a 2D system, with the material defining the x - y plane (Figure 2.9), we define a 2D

conductivity tensor as shown below.

$$\begin{bmatrix} J_x \\ J_y \end{bmatrix} = \begin{bmatrix} \sigma_{xx} & \sigma_{xy} \\ \sigma_{yx} & \sigma_{yy} \end{bmatrix} \begin{bmatrix} E_x \\ E_y \end{bmatrix} \quad (2.13)$$

where $J_{x,y}$ and $E_{x,y}$ are current density and electric field in the principal directions. In a homogeneous, isotropic material without time-reversal symmetry breaking mechanisms, like graphene, the Onsager relations imply $\sigma_{xx} = \sigma_{yy}$ and $\sigma_{xy} = -\sigma_{yx}$. It is also useful to note the resistivity tensor elements,

$$\begin{aligned} \rho_{xx} &\equiv \frac{E_x}{J_x} = \frac{\sigma_{xx}}{\sigma_{xx}^2 + \sigma_{xy}^2} \\ \rho_{xy} &\equiv \frac{E_y}{J_x} = \frac{\sigma_{yx}}{\sigma_{xx}^2 + \sigma_{xy}^2}. \end{aligned} \quad (2.14)$$

In the case of a Hall bar geometry (Figure 2.9) with current directed I_x along the $+x$ axis, experimentally measurable resistances are related to resistivity values via the width of the sample W and length of the sample L .

$$\begin{aligned} \rho_{xx} &= \frac{E_x}{J_x} = \frac{V_x/L}{I_x/W} = R_{xx} \frac{W}{L} \\ \rho_{xy} &= \frac{E_y}{J_x} = \frac{V_y/W}{I_x/W} = R_{xy} \end{aligned} \quad (2.15)$$

When this material is exposed to a magnetic field B_z perpendicular to the atomic plane ($+z$ -direction), the resulting Lorentz force along the y axis induces a Hall voltage V_y along

y. Depending on the charge carrier type, the direction of the Hall voltage is determined.

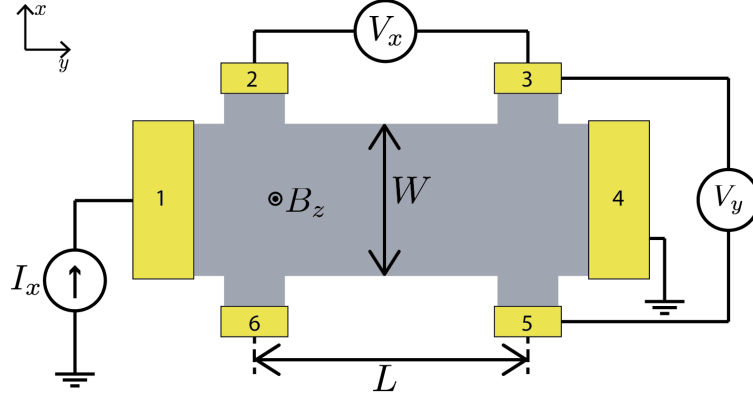


Figure 2.9: Schematic of an experiment with a Hall bar that shows the geometric parameters of the sample, the directions of the applied current I_x and magnetic field B_z , and the measured longitudinal (V_x) and transverse (V_y) voltages. Longitudinal and transverse resistances are measured simultaneously, in a 4-point configuration and without mixing. The transverse voltage pick-up, V_y is the Hall voltage induced due to the perpendicular magnetic field B_z .

A Hall-bar geometry allows for measuring the longitudinal (R_{xx}) and transverse (R_{xy}) resistances without mixing contributions of ρ_{xx} and ρ_{xy} . Moreover, both resistances can be measured simultaneously in a 4-point configuration, which negates the effects of contact resistance. A voltage is applied to terminals 1 to 4, creating a current I_x . Induced Hall voltage, V_y , due to the out-of-plane magnetic field, B_z , is picked up from terminals 3 and 5. Longitudinal voltage, V_x , is measured from terminals 2 and 3. The Hall coefficient is extracted from the measured quantities using

$$R_H \equiv \frac{V_y}{I_x B_z} = \frac{R_{xy}}{B_z} \quad (2.16)$$

Near the charge neutrality point, both electrons and holes contribute to conduction in graphene. In such a system, the Hall coefficient depends on the charge density (n_e, n_h) and mobility (μ_e, μ_h) of electrons and holes according to a simple Drude-Lorentz model [57],

$$R_H = \frac{n_e \mu_e^2 - n_h \mu_h^2}{e(n_e \mu_e + n_h \mu_h)^2} \quad (2.17)$$

where e is the elementary charge.

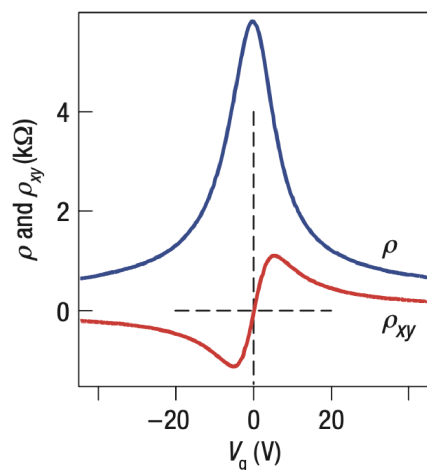


Figure 2.10: The longitudinal ($\rho = \rho_{xx}$) and transverse (ρ_{xy}) resistivities of graphene with respect to gate voltage which is directly proportional to carrier density at a constant magnetic field. To describe ρ and ρ_{xy} near neutrality, a single carrier model is not applicable and contributions from both carrier types need to be considered. Reprinted with permission from Ref [32].

The experimental results from [25] demonstrates the antisymmetric behaviour of ρ_{xy} (Figure 2.10). Here, ρ_{xy} is presented with respect to an externally applied gate voltage, which is in turn directly proportional to carrier density is measured at a constant magnetic

field. Near the charge neutrality point, both electrons and holes contribute to the Hall coefficient.

Away from the charge neutrality point, the effect from minority carriers can be neglected. The Hall coefficient simplifies to,

$$R_H = \frac{1}{en_{e,h}}. \quad (2.18)$$

As a result, carrier density is inferred directly from the measured transverse resistance.

$$n_{e,h} = \frac{B_z}{eR_{xy}} \quad (2.19)$$

Once the carrier density is estimated, carrier mobility can then be calculated using,

$$\mu_{e,h} = \frac{1}{en_{e,h}\rho_{xx}} = \frac{L}{en_{e,h}R_{xx}W}, \quad (2.20)$$

which is known as the Hall mobility, being derived from a Hall measurement.

2.3 Magnetoresistance in Graphene

While the Drude-Lorentz model predicts R_{xx} independent of magnetic field in the case of a single carrier type, relevant to graphene away from neutrality, experiments reveal a non-zero magnetoresistance, meaning a dependence of R_{xx} upon magnetic field B_z . We use the effective medium theory developed by Ping et al. [58] to model the magnetoresistance of

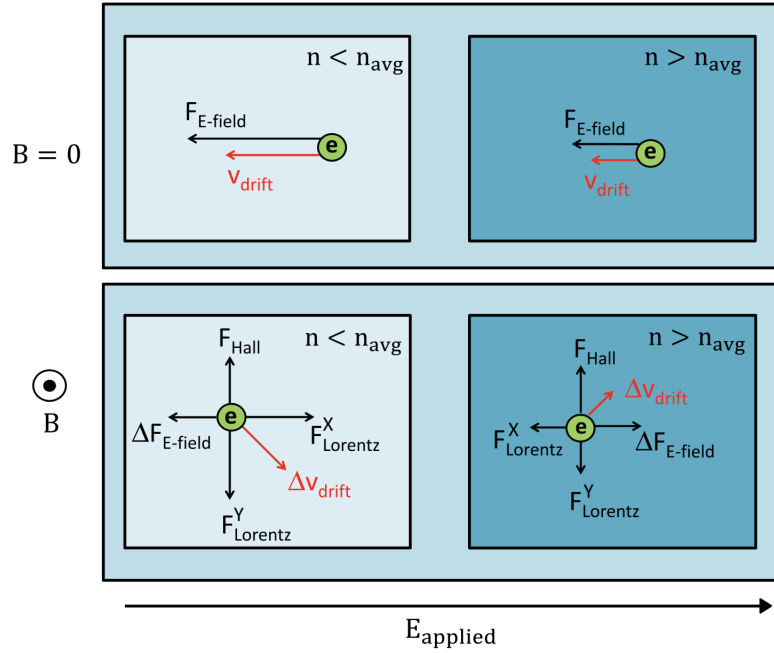


Figure 2.11: Magnetoresistance due to carrier density inhomogeneity. The forces acting on an electron in low density (left panels) and high density (right panels) regions, in the absence (higher panels) and presence (lower panels) of magnetic field B . The change in drift velocity in the presence of magnetic field results in magnetoresistance. Reprinted with permission from Ref [58].

graphene.

Effective medium theory is typically applied to 2-band systems. An example is inhomogeneous doped graphene near the Dirac point where the system exhibits electron dominant and hole dominant spatial regions [59] and magnetoresistance contributions from both needs to be considered. According to Ping et al. the effective medium theory is still applicable to graphene away from the Dirac point, with the assumption that carrier density inhomogeneity creates higher and lower carrier density regions as represented in Figure

2.11. The Hall force, due to charge separation at the Hall bar edges, depends on average carrier density n_{avg} is common to regions of higher and lower density. Therefore, the local Lorentz force due to the magnetic field varies in direction across regions of different local density, modulating the local drift velocity due as a function of magnetic field. Magnetoresistance, meaning R_{xx} dependence upon B_z , emerges. The model of Ping et al. assumes that the carrier density n has a Gaussian form with an average carrier density n with an rms fluctuation δn_{rms} . The analytical form of magnetoresistance is given as

$$\rho_{xx}(B) = \rho_0 [1 + A(\mu B)^2]. \quad (2.21)$$

Here, ρ_0 is the inferred zero-field resistivity $\rho_{xx}(0)$ and A is a dimensionless coefficient $A = 0.5 (n/\delta n_{rms})^{-2}$. The result is a quadratic magnetoresistance due to inhomogeneous carrier density that persists far away from the Dirac point. The quadratic form is not specific to linear dispersion. The agreement of this model to experimental results of ultra-high doped graphene will be discussed in Chapter 3.

2.3.1 Weak Localization in Graphene

When electrons scatter due to impurities or defects in a material, they can experience constructive or destructive interference if phase coherence is maintained. In the weak localization regime, coherent backscattering of electrons becomes more likely, resulting in a

reduction of electron diffusion and an increased probability of their return to their starting position (Figure 2.12a). This effect leads to a characteristic negative correction to the electrical conductivity at low temperatures and is a crucial manifestation of quantum interference in disordered materials [60].

The observation of the weak localization effect requires certain conditions to be met. Lower temperatures lead to longer electron phase coherence times, which are necessary for coherent backscattering and interference effects to be significant. Moreover, the material should have a certain degree of disorder, such as impurities, defects, or rough surfaces. These sources of disorder are essential for inducing scattering events. Low-dimensional systems, such as thin films, are more likely to exhibit the weak localization effect. Reduced dimensionality increases the probability of electron interference and enhances the visibility of the effect. The weak localization effect is sensitive to magnetic fields. In the presence of a magnetic field, magnetic flux imparts a phase shift in the electronic wavefunction in proportion to the subtended area of the electron path, which can suppress the weak localization effect. Therefore, weak localization experiments are typically conducted versus magnetic field. By tuning the effect under varying magnetic fields, researchers can precisely quantify the quantum interference contribution to classical resistance. A thorough review of the fundamental theoretical and experimental principles of weak localization are presented in [60].

The theory for the weak localization effect was first developed by Hikami et al. [61].

Later, McCann et al. [62, 63] extended the theory to graphene and presented an analytical expression for the quantum correction to conductivity, which is sensitive to contributions from multiple scattering mechanisms: dephasing, intervalley scattering, intravalley scattering. The scattering lengths associated with these mechanisms are defined below.

- phase coherence length, L_ϕ : Phase coherence length depends on the rate of inelastic scattering events. Frequent inelastic scattering events disrupt phase coherence, leading to the suppression of weak localization. Electron-electron and electron-phonon scattering mechanisms both fall into this category. Specifically, electron-phonon scattering is significantly affected by the thermal energy of the lattice, making temperature a critical factor that can shorten the phase coherence length.
- intervalley scattering length, L_i : Intervalley scattering is an elastic process due to atomically sharp scatterers, boundaries or ripples. Because of this nature, the intervalley scattering rate highly depends on specific device characteristics.
- intravalley scattering length, L_* : Intravalley scattering is another elastic scattering process that is due to chirality breaking defects and trigonal warping. At high doping densities where the Fermi level shifts to high energies, trigonal warping is expected to be dominant.

The scattering lengths can be expressed in terms of scattering times using

$$\tau_{\phi,i,*} = \frac{L_{\phi,i,*}^2}{D} \quad (2.22)$$

where D is the diffusion coefficient and is given by

$$D = \frac{1}{2} v_F^2 \tau_{tr} \quad (2.23)$$

where v_F is the Fermi velocity and τ_{tr} is the transport scattering time that is determined from the carrier mobility.

In the formalism of Ki et al. [64], the quantum correction to conductivity $\Delta\sigma$ is expressed in terms of the scattering lengths L_ϕ , L_i and L_* .

$$\Delta\sigma_{xx}(B) = \frac{e^2}{\pi h} \left[F \left(\frac{8\pi B}{\Phi_0 L_\phi^{-2}} \right) - F \left(\frac{8\pi B}{\Phi_0 (L_\phi^{-2} + 2L_i^{-2})} \right) - 2F \left(\frac{8\pi B}{\Phi_0 (L_\phi^{-2} + L_i^{-2} + L_*^{-2})} \right) \right] \quad (2.24)$$

where $F(z) = \ln z + \psi(0.5 + z^{-1})$, $\psi(x)$ is the digamma function and $\Phi_0 = h/e$ is the flux quantum.

Weak localization measurements are useful to gain insight into the different scattering mechanisms in a material. Several studies have contributed to the understanding of scattering mechanisms in graphene through weak localization experiments [64–68]. When electrons in graphene complete a closed trajectory they pick up a Berry phase of π owing

to the chiral nature of the electronic wavefunction around the K point. This results in destructive interference of the electron wavefunctions and weak anti-localization is observed, a unique aspect of graphene [67]. On the other hand, intervalley scattering favors weak localization given that carriers that are scattered to another valley can have zero phase difference due to the reversed chirality of the two valleys [68]. Figure 2.12 illustrates how the balance between different scattering times determines the presence of either a localization or an anti-localization effect.

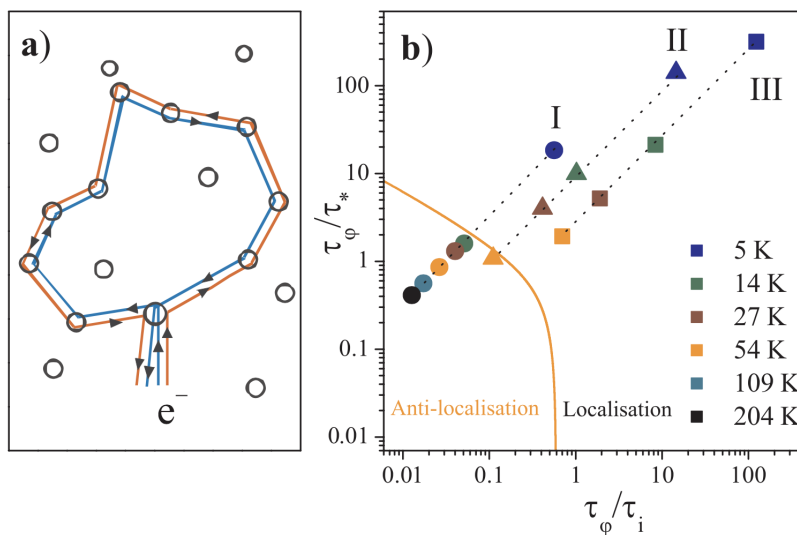


Figure 2.12: Weak (anti)localization in graphene. (a) A sketch of two electron scattering trajectories that can interfere constructively (localization) or destructively (anti-localization). (b) Summary plot for weak (anti)localization experiments conducted at different temperatures and for samples with different carrier densities (carrier density is increasing as $I \rightarrow III$). The interplay between different scattering times determines the (anti)localization effect. Reprinted with permission from Ref [67].

Trigonal warping of the Dirac cones, which is prominent at high doping densities,

strongly effects intravalley scattering. The intravalley scattering rate can be expressed as a combination of two mechanisms, τ_z^{-1} is the scattering rate induced by chirality breaking defects, and τ_w^{-1} the scattering rate induced by trigonal warping [69].

$$\tau_*^{-1} = \tau_z^{-1} + \tau_w^{-1} \quad (2.25)$$

At ultra-high doping densities, intravalley scattering is dominated by trigonal warping, therefore, we also introduce the analytic expression for the trigonal warping scattering length resulting from a perturbation calculation based on a tight-binding electronic structure [62, 68],

$$L_w^{-2} = \frac{\tau_{tr}}{D} \left(\frac{\tilde{\mu} E_F^2}{\hbar v_F^2} \right)^2 \quad (2.26)$$

where $\tilde{\mu} = \gamma_0 a_0^2 / 8\hbar^2$ is a structure constant, γ_0 is the nearest neighbour hopping energy and a_0 is the graphene lattice constant. The Fermi velocity $v_F = 3^{1/2}(\gamma_0 a / 2\hbar)$ in the nearest neighbour tight-binding model [70]. Combining these definitions leads to the simplified expression:

$$L_w = \left(3^3 / 2 \right)^{1/2} a_0 (\gamma_0 / E_F)^2. \quad (2.27)$$

where $a_0 = 2.46 \text{ \AA}$ is the graphene lattice constant and $\gamma_0 = -3.441 \text{ eV}$ is the nearest-neighbour hopping energy.

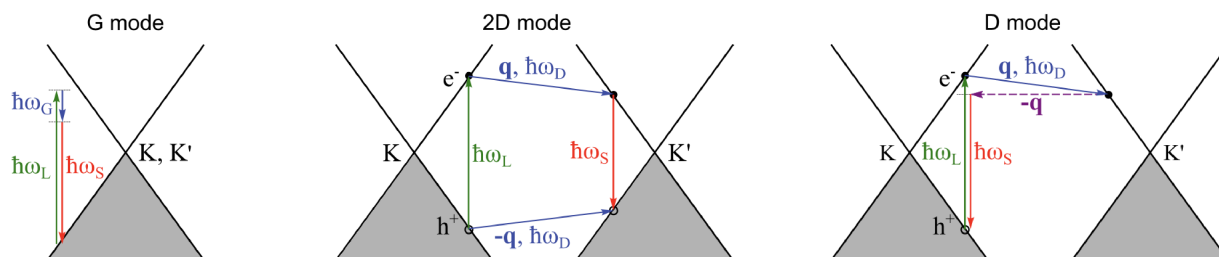


Figure 2.13: Schematic representation of the G , G' and D features in the momentum-energy space, in graphene. Reprinted with permission from Ref [71].

2.4 Raman Spectroscopy of Graphene

Raman spectroscopy is a commonly used tool in the characterization of materials. It relies on inelastic scattering processes in a material due to the interaction of the incident light with the material's vibrational, rotational, or electronic states. By the identification of spectral signatures, information about molecular structure can be obtained. Raman spectroscopy is also sensitive to other physical properties of a material such as strain, crystal structure, lattice symmetry and Fermi level.

In graphene, the most widely studied characteristic Raman features are the G , G' and D bands as illustrated in Figure 2.13. The G band is located at 1585 cm^{-1} and remains unaffected by excitation energy. The G band phonon, arising from in-plane optical-phonon modes at Γ , is a first-order Raman process primarily affected by graphene's strong electron-phonon interaction [70]. Thus, doping significantly influences the G band frequency and lineshape, revealing information about graphene's electronic properties.

The G' band, also referred to as the $2D$ band, is especially prominent in graphene. The

G' band is dispersive and it is located at 2700 cm^{-1} for an excitation energy of 2.4 eV [70]. It is a second-order, two-phonon feature that involves intervalley scattering. The intensity and lineshape of the G' band has been widely utilized to determine the number of layers of graphene [72]. Moreover, the G' band intensity is adversely affected by electron-electron scattering, causing the G' band to vanish at high doping levels as experimentally observed in several studies [26, 73, 74].

The D band is also dispersive and is located at 1350 cm^{-1} for an excitation energy of 2.4 eV [70]. It is associated with a one-phonon intervalley scattering process. The D band is due to the breathing modes of the graphene lattice. It becomes Raman active when the lattice symmetry is broken, therefore the D peak is only observed in the presence of defects [73]. The intensity ratio of the G and D bands, I_D/I_G , has been utilized to quantify the defect density in graphene [75]. Furthermore, I_D/I_G is sensitive to the crystallinity and have been used to quantify the crystallite size in graphite [76].

2.4.1 Raman G-peak shift

In this section, we introduce the model of Hell et al. [77] to express the G -peak shift due to doping, $\Delta\omega_G$, in terms of the charge carrier density n . $\Delta\omega_G$ depends on two contributions, namely the static contribution $\Delta\omega_S$ and dynamic contribution ω_D .

$$\Delta\omega_G = \alpha\Delta\omega_S + \Delta\omega_D \quad (2.28)$$

Here, the static contribution, $\Delta\omega_S$, is associated with lattice expansion and adiabatic electron-phonon coupling, α is the ratio of static G -peak shift of graphene in the presence of graphene-substrate interactions to that of an ideally decoupled graphene, and the dynamic contribution, ω_D , is associated with non-adiabatic electron-phonon coupling effects.

The static contribution $\Delta\omega_S$ to ΓE_{2g} phonon frequency, including static lattice expansion and the adiabatic contribution to phonon softening was computed by density functional theory by Lazzeri et al. [78], and fit to the analytic form,

$$\frac{\Delta\omega_S}{2\pi c} = -2.13n - 0.0360n^2 - 0.00329n^3 - 0.226|n|^{3/2} \quad (2.29)$$

where n is the charge carrier density in units cm^{-2} . The dynamic contribution $\Delta\omega_D$ to ΓE_{2g} phonon frequency, consisting of the non-adiabatic contribution to phonon softening, was calculated using the numerical prescription of Lazzeri et al. [78] and a 3NNTB electronic structure for graphene [52]. The dynamic contribution is,

$$F^{E_F}(\omega_0) = \frac{2}{N} \sum_{\mathbf{k}, n \neq m} \frac{D^2 [f(E_{\mathbf{k},m}) - f(E_{\mathbf{k},n})]}{E_{\mathbf{k},m} - E_{\mathbf{k},n} + \hbar\omega_0 + i\delta} \quad (2.30)$$

$$\Delta\omega_D = \text{Re} \left[\frac{F^{E_F}(\omega) - F^0(\omega)}{2M\omega_0} \right] \quad (2.31)$$

where the summation runs over N wavevectors \mathbf{k} covering the first Brillouin zone, over

the $m, n = \pi, \pi^*$ bands of graphene, ω_0 is the unperturbed phonon frequency, D^2 is the deformation potential, $\delta = 10$ meV is the lifetime broadening, $f(E_{\mathbf{k},m})$ is the Fermi function evaluated for the state in band m at wavevector \mathbf{k} , and M is the mass of a carbon atom.

The model of the electron density dependent Raman G -band shift will be used to gain insight to ultra-high doped graphene in Chapter 3.

Chapter 3

High-density, On-chip, Alkali Doping of Graphene

The electron transport properties of nearly charge neutral graphene has been the subject of intense investigation, owing to the massless, conical, dispersion near neutrality at the K and K' points in the Brillouin zone (BZ) [54]. Less well studied are the electron transport properties of heavily electron doped graphene, where the massive, hyperbolic dispersion at the M and M' saddle points in the Brillouin zone leads to a van Hove singularity (vHS) in the density of states [28, 79–81]. The emergence of superconductivity in doped monolayer graphene, prompted by strong electron-phonon coupling at the extended vHS, has been the subject of inquiry [82–84]. Recently, superconductivity has been observed in twisted bilayer graphene at the magic angle [46] where a vHS emerges at low energy due to interlayer

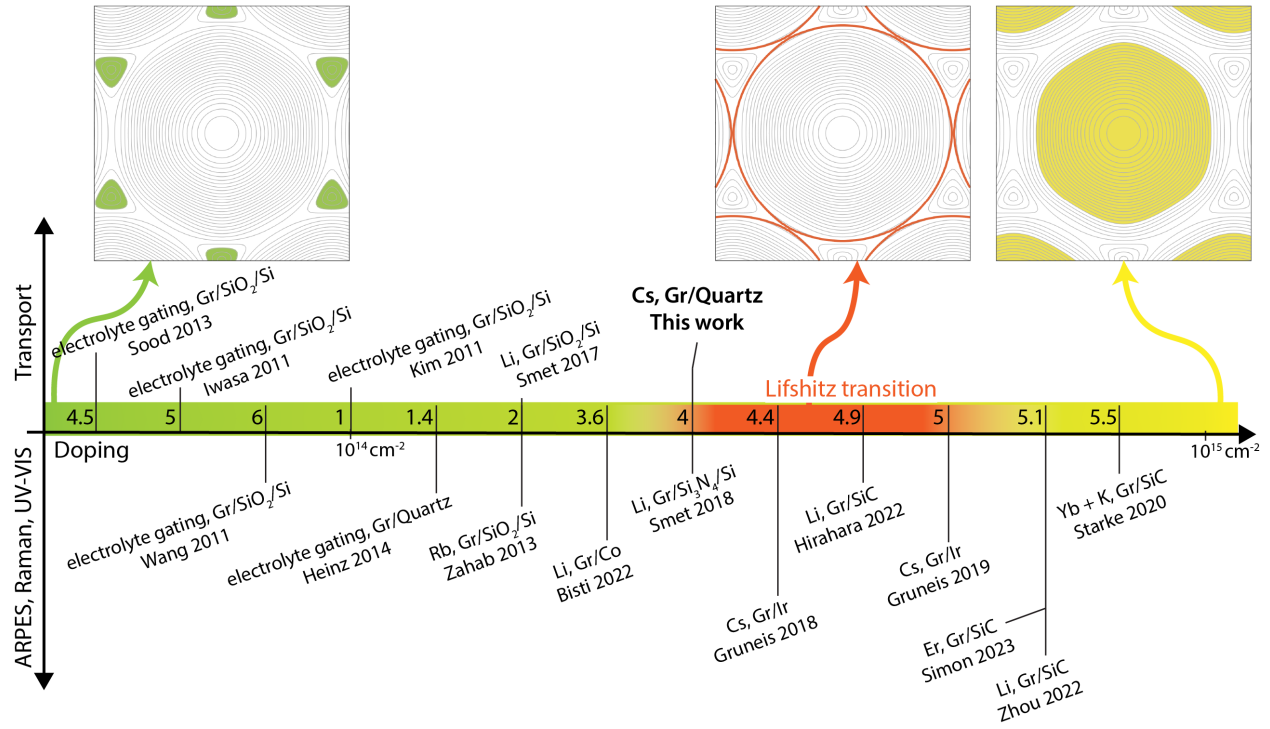


Figure 3.1: Doping monolayer graphene towards the Lifshitz transition. A schematic of the Fermi surface contours in π^* conduction band of monolayer graphene vs doping. Electron and hole pockets are shown in green and yellow, respectively. The Lifshitz transition is estimated to occur at $n = 3.7 - 5.1 \times 10^{14} \text{ cm}^{-2}$. The charge carrier densities achieved in ARPES, Raman and UV-VIS (below) and charge transport studies (above) are summarized.

coupling [45]. In the case of monolayer graphene, however, vHS is too far from the intrinsic Fermi level and ultra high carrier density is necessary to access such effects.

As the carrier density increases in monolayer graphene, the Fermi surface passes through the M , M' points where the Fermi surface topology changes from describing electron-pockets to hole-pockets exemplifying a Lifshitz transition as shown schematically in Fig. 3.1. Charge transport is one of several physical properties that are sensitive to changes in Fermi surface

geometry [85], yet no transport measurements in heavily doped graphene in the vicinity of the Lifshitz transition have been reported to date. Achieving a stable, electron doping sufficient to reach the Lifshitz transition in an electrically contacted graphene device on an insulating substrate has remained elusive to date. Angle resolved photoemission spectroscopy (ARPES) studies have mapped the Fermi surface of heavily doped monolayer graphene in the vicinity of the M and M' points [28, 77, 86–88], with the role of many-body interactions in flattening and thereby extending the vHS a matter of active debate [89–91]. The required electron density to reach the Lifshitz transition has been variably estimated to be in the range $n = 3.7 - 5.1 \times 10^{14} \text{ cm}^{-2}$ [87, 88] (Fig. 3.1).

Alkaline metal doping (Li, K, Ca, Cs) and rare earth doping (Er, Yb) of graphene in an ultra-high vacuum (UHV) environment has enabled doping in excess of $n = 4 \times 10^{14} \text{ cm}^{-2}$ for ARPES studies of graphene [28, 77, 86–90]. In contrast, ionic liquid gating has enabled electron doping in the range of $0.5 - 2 \times 10^{14} \text{ cm}^{-2}$ in electrically contacted graphene on Si/SiO₂ substrates [92–94], well below the threshold for the Lifshitz transition. Lithium polymer electrolytic gating has been used to achieve electron doping as high as $2 \times 10^{14} \text{ cm}^{-2}$ in electrically contacted bilayer graphene [27], while transmission electron microscopy reveals domains with superdense Li ordering in suspended graphene bilayers corresponding to $n = 4 \times 10^{14} \text{ cm}^{-2}$ per graphene sheet [95]. Li doping of epitaxial graphene on SiC in an integrated deposition and cryogenic charge transport measurement system was used to achieve electron densities as high as $2.2 \times 10^{14} \text{ cm}^{-2}$, enabling measurement of weak localization at high

electron density [96].

The transport properties of adatom-decorated graphene have been investigated to understand the impacts of adatom doping on mobility and magnetoresistivity. In K-doped graphene, the influence of charged impurity scattering on mobility has been demonstrated to follow $n \propto 1/\mu$ according to the findings by Chen et al. [97], consistent with the theory established by Adam et al. [98]. Quasilinear magnetoresistance has been observed in In-decorated graphene [99]. This study attributes the presence of magnetoresistance away from the neutrality point to the effects of carrier density inhomogeneity induced by adatoms. Additionally, the suppression of Shubnikov–de Haas oscillations due to adatom doping is reported. In the magnetotransport investigation of tungsten-decorated graphene, scattering lengths were extracted from weak-localization fits at various doping and adatom densities [100]. The results indicate that scattering times decrease with adatom density, while they increase with carrier density. The studies on adatom-decorated graphene mentioned above are confined to carrier densities on the order of 10^{12} cm^{-2} , where the Dirac cone approximation of the graphene band structure remains valid.

In this chapter, we present a new method of doping electrically contacted large-area graphene to ultra-high charge carrier density, reaching $n = 4 \times 10^{14} \text{ cm}^{-2}$ as confirmed by high-field Hall measurement. The flip-chip method is versatile: it can be applied to different host material and dopant systems. The method features *in situ* charge transport characterization during alkali doping. As shown schematically in Figure 3.3, flip-chip

encapsulation of an alkaline metal vapour source in an inert gas environment electron dopes electrically contacted graphene, enabling ultra-high doping approaching that required to observe charge transport in the vicinity of the Lifshitz transition. The impermeability of the encapsulation to external oxidizing agents permits sample manipulation in an ambient atmospheric environment, enabling the study of heavily doped graphene by different experimental techniques. We report here real-time measurement of the graphene resistivity tensor elements ρ_{xx} and ρ_{xy} in an ac magnetic field during the doping process, the measurement of Hall effect, weak-localization and magnetoresistance at cryogenic temperature $T = 1.7$ K at magnetic fields up to $B = 7$ T, and the measurement of non-resonant Raman scattering of heavily doped graphene with a pump wavelength $\lambda = 785$ nm through the optically transparent quartz substrate. We find a reduction in electron mobility μ at high electron density n in accord with that expected from the increase in effective mass $m_* = \hbar^2(2\pi)^{-1}\partial A_k/\partial E_F$ [101], a quadratic magnetoresistance $\rho_{xx} \propto 1 + A(\mu B)^2$ indicative of doping inhomogeneity [58], an intravalley scattering length $L_* = 10 - 20$ nm comparable to that expected by enhanced trigonal warping at high doping density, the suppression of second order $G'(2D)$ Raman scattering amplitude compared to first order G scattering due to non-resonant detuning, and G peak Raman shift in good agreement with previous reports of heavily doped graphene [77].

3.1 Experimental Methods

3.1.1 Fabrication of Graphene Hall bar devices

We used graphene grown by chemical vapour deposition (CVD) on poly-crystalline copper foil in a cold wall CVD reactor (Aixtron BM) at Graphenea, and transferred onto a 100 mm diameter quartz (001) substrate following sacrificial etch of the copper growth substrate. Quartz is the substrate of choice due to its chemical inertness and optical transparency. We prepare $50\ \mu\text{m} \times 500\ \mu\text{m}$ graphene Hall-bar devices using photo-lithographic methods for fabrication of electrical contacts and for patterning graphene into a Hall-bar shape. We use a OiR photoresist by Fujifilm and work with a Karl Suss MA6 Mask Aligner. Following the initial lithography unwanted graphene was etched using O_2 plasma, at a rate of 8 sccm at 200 mbar for 9 seconds. After the second lithography we deposit Ti/Au (5 nm /80 nm) using an e-beam evaporator to realize the Ohmic contacts. An optical microscopy image is presented in Figure 3.5. The six-contact Hall-bar geometry enables the simultaneous measurement of four-probe longitudinal resistance $R_{xx} = V_x/I_x$ and transverse resistance $R_{xy} = V_y/I_x$. Prior to all doping experiments, we thermally annealed the Hall bar samples and chip carriers in a nitrogen glove box environment at $120^\circ\ \text{C}$ to remove adsorbed water.

3.1.2 The flip-chip method and the experiment setup

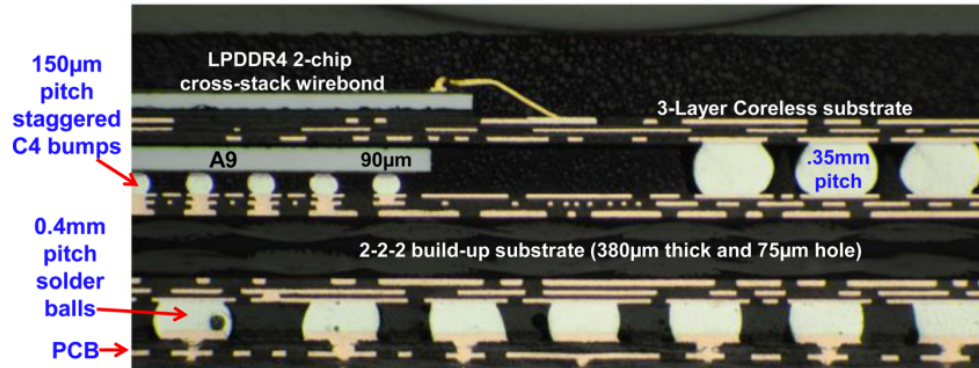


Figure 3.2: Flip-chip assembly in Apple’s smartphone: The A9 application processor is housed in a package-on-package format and the solder bumped flip chip is reflowed on an organic package substrate. Reprinted with permission from Ref [102].

The flip-chip method was introduced in the 1960s as a versatile, high-performance, and compact way to package microelectronic circuits [103, 104]. In the flip-chip method, the conducting pads of a chip are connected to the pads of a chip carrier using various interconnect materials, with the chip surface facing the chip carrier. Electrical connection between the chip and chip carrier is commonly established through mass reflow or thermocompression bonding. Mass reflowing involves a heating cycle that melts the solder interconnects, providing electrical contact and enabling self-alignment of the chip due to the surface tension of the molten solder [105]. Thermocompression bonding requires the application of heat and force to hold the chip at a specific distance from the chip carrier [102]. Flip-chip joint performance can be enhanced by applying an underfill between the chip and chip carrier. Underfill application reduces thermal stress on the solder joints,

ensures good adhesion, and protects joints from oxidation. Flip-chip technology is still used for the assembly of integrated circuits, as demonstrated in the cross-section of the Apple iPhone 6 Plus (Figure 3.2). In our experiments, we employ the flip-chip method to package graphene Hall bar devices, in order to encapsulate the air sensitive Cs-doped graphene while preserving the electrical connections.

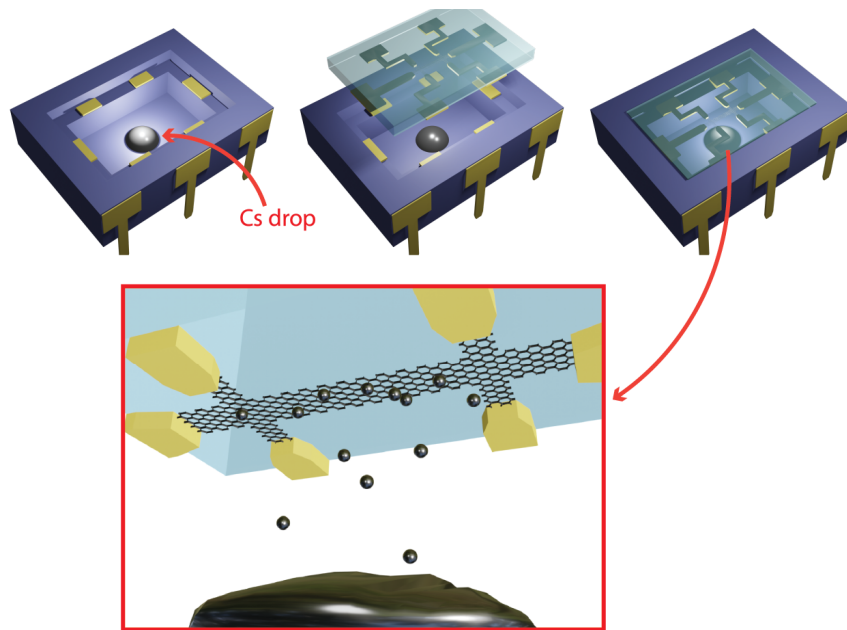


Figure 3.3: Schematic of the flip-chip assembly. A drop of Cs is placed on the chip carrier. A graphene Hall bar device on quartz is brought face down to enclose the Cs in the cavity and expose graphene to Cs vapour. (inset) Schematic of Cs atom adsorption onto the graphene Hall bar device.

A dual in-line package ceramic chip carrier with a recessed cavity and gold electrodes atop a recessed mesa (Fig. 3.4) is utilized for the flip-chip assembly in our experiments. The Hall bar contacts of the graphene device on quartz are designed to align with the gold pads

on the chip carrier. A drop of Cs ($\approx 14 \mu\text{L}$ in volume) is drop-cast by glass pipette the gold ground pad of the chip carrier inside a nitrogen glove box ($\text{H}_2\text{O} \leq 0.1 \text{ ppm}$ and $\text{O}_2 \leq 1 \text{ ppm}$). The quartz substrate with the graphene Hall bar device is flipped onto the chip carrier as shown in Figure 3.3 and 3.4. Pure In spheres (0.5 mm diameter) are used to establish reliable electrical contact between the electrodes of the chip carrier and the quartz substrate. The graphene Hall bar faces the Cs source directly and is exposed to the Cs vapour within the cavity. A compact resistive heater under the chip carrier is used to increase temperature and thus Cs vapour pressure.

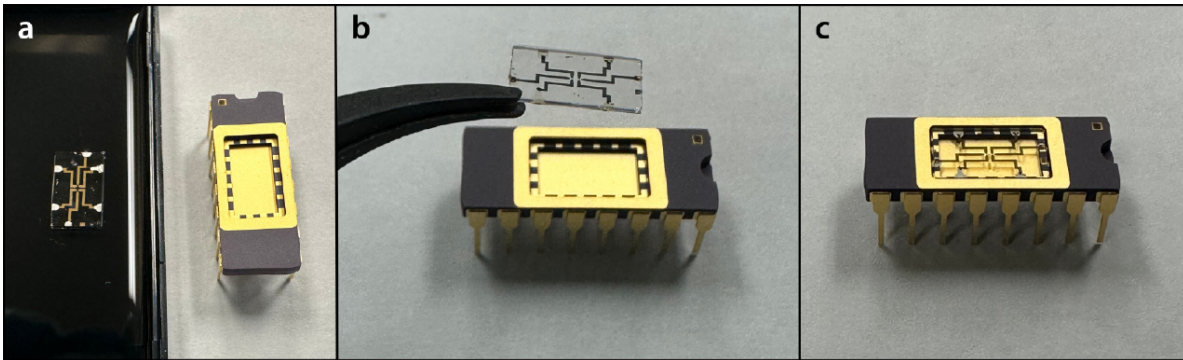


Figure 3.4: Photograph of the flip-chip assembly and the Hall-bar device. (a) shows a graphene Hall bar device on a quartz substrate and a ceramic 16 pin dual in-line chip carrier side by side. The Hall bar contacts are designed to align with the gold pads on the chip carrier. (b, c) A drop of Cs (not shown) is placed on the gold ground pad of the chip carrier and the Hall bar device is contacted to the chip carrier as shown.

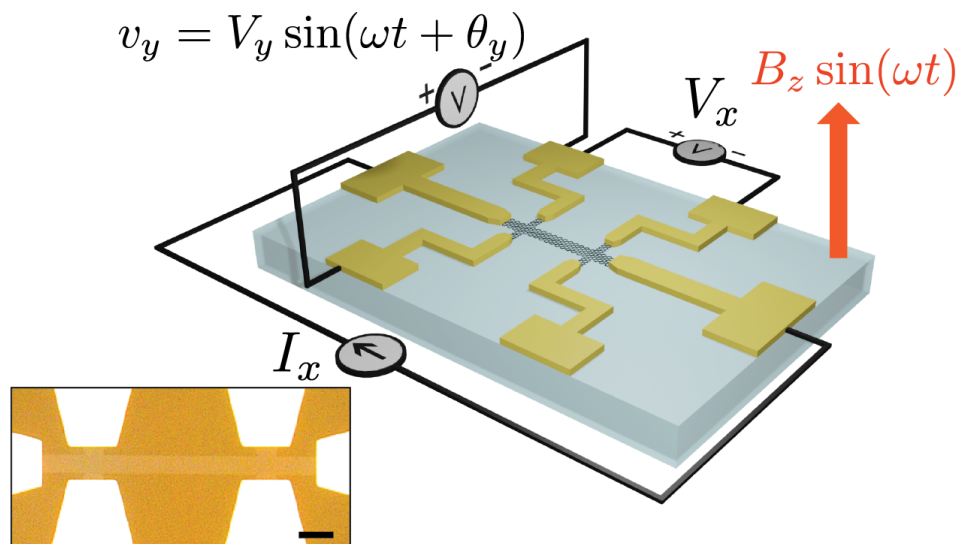


Figure 3.5: AC Hall measurement configuration. A schematic of the AC Hall measurement configuration for the Hall bar device on quartz. (inset) Optical microscopy image of a Hall-bar device on quartz. Scale bar represents 100 μm .

A home-built, ferrite core ($\mu = 2500\mu_0$) electromagnet with pole area $A = 560 \text{ mm}^2$, pole gap $d = 20 \text{ mm}$, inductance $L = 43.5 \text{ mH}$, and field/current ratio $B/I = 22.6 \text{ mT A}^{-1}$ was used for real-time Hall measurement during doping in a glove box environment. We used an AC-DC Hall measurement configuration (Fig. 3.5) where the sample was placed in an AC magnetic field, $B_z \sin(\omega t)$, in the magnet gap while it was biased with a DC current, I_x . A similar method has been employed for Hall measurement of organic field effect transistors [106]. Magnetic field amplitudes of $B_z = 20 - 25 \text{ mT}$, at a frequency of $f = 3 \text{ Hz}$ was used. The DC current bias of the sample was $I_x = 200 \text{ }\mu\text{A}$. As a result, the Hall voltage is expected to be $V_y \sin(\omega t + \theta_y)$ where θ_y is 0 or π according to charge carrier

type. In all experiments, the direction of the bias current is selected such that Hall voltage phase $\theta_y = 0$ ($\theta_y = \pi$) corresponds to electron (hole) doped graphene. In all experiments, the background inductive voltage (amplitude and phase) due to Faraday effect was measured with zero sample bias, $I_x = 0$ μA , and subtracted to obtain sample response.

Following Cs doping, we sealed the flip-chip cavity with a UV activated epoxy (Solarez) followed by Stycast (Loctite). Figure 3.6 shows photographs of a sealed device. The Cs and the Cs-doped graphene are protected from the ambient environment when the cavity is sealed. The sealed device was removed from the glove box for high magnetic field transport measurements and Raman spectroscopy. High magnetic field ($B = 7$ T) and low-temperature ($T = 1.3$ K) measurement of longitudinal and transverse resistance was performed in a closed-cycle cryostat with a superconducting solenoid. Hall voltage, magnetoresistance, and weak-localization response of the doped graphene Hall bars was analyzed. Raman spectroscopy was performed with a Renishaw InVia confocal Raman microscope, 50-X magnification objective at $\lambda = 785$ nm, with $P = 90$ mW laser power. Background removal was performed on all Raman spectra.

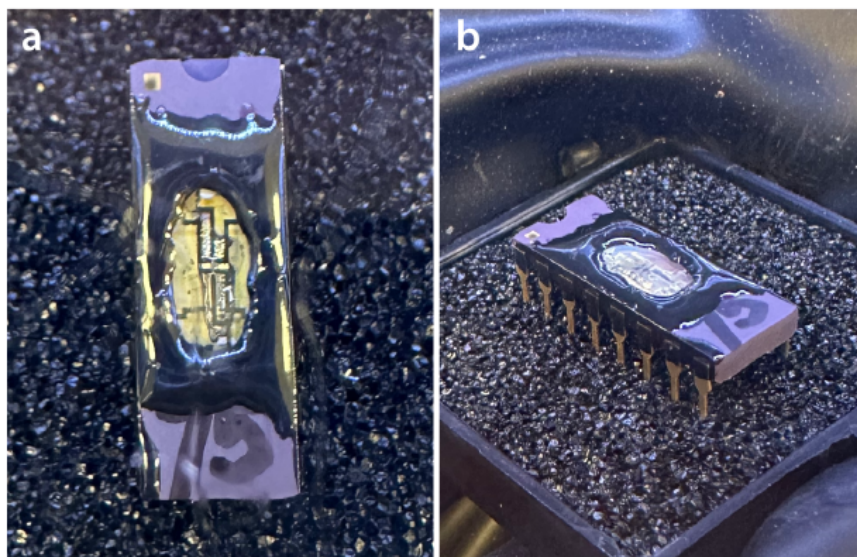


Figure 3.6: Photographs of a Cs doped graphene sample in the ambient environment after sealing.

3.2 Real-time Hall Analysis During Cs Doping

CVD graphene transferred onto quartz is initially p-type doped ($p \approx 8 \times 10^{12} \text{ cm}^{-2}$), as measured by Hall effect in all our samples prior to doping experiments. During exposure to Cs vapour, ionization of adsorbed Cs atoms leads to valence electron donation to graphene. The initially p-type graphene on quartz is expected to pass through charge neutrality and become n-type. In order to observe the transition through the charge neutrality point (CNP), we conducted doping experiments at room temperature. We measured the longitudinal voltage, V_x , and the Hall voltage, v_y , while graphene is exposed to Cs vapour. The resistances R_{xx} and R_{xy} , as well as the phase θ_y of v_y , is shown in Fig. 3.7. The dashed line represents the CNP,

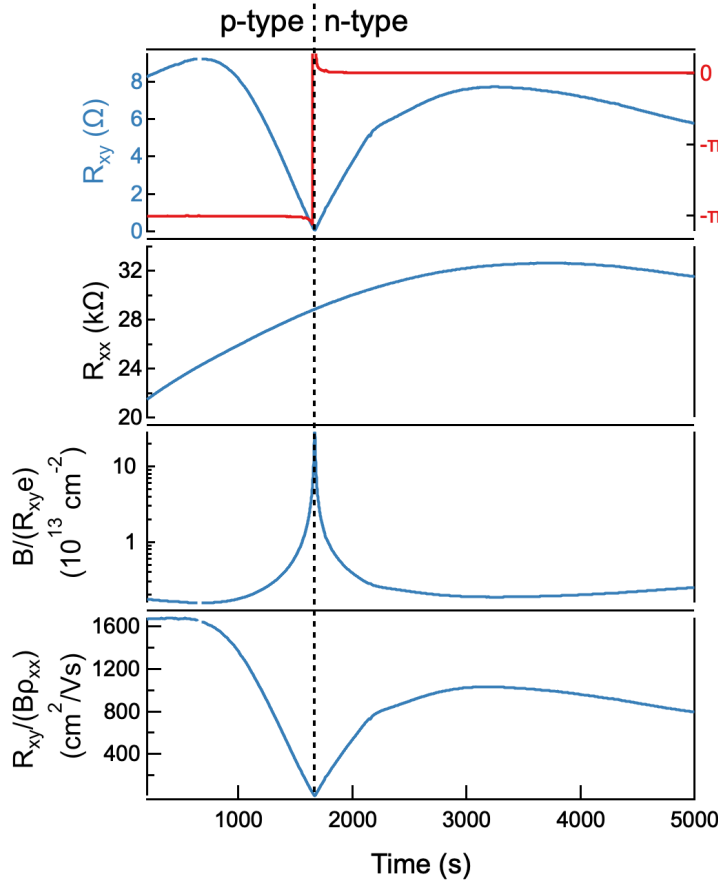


Figure 3.7: Doping graphene through the CNP. Variation of the transverse (Hall), R_{xy} , and longitudinal, R_{xx} , resistances of a graphene Hall bar versus time t during exposure to Cs vapour, measured by AC Hall effect. The abrupt change in the Hall voltage phase, θ_y , corresponds to Hall resistance sign reversal and change in carrier type as the CNP is crossed. The quantities $B_z/(R_{xy}e)$ and $R_{xy}/(B_z\rho_{xx})$, are plotted versus time and correspond to carrier density, n , and mobility, μ , respectively, at doping away from the CNP.

when θ_y changes abruptly from π to 0, signalling the change from hole doped to electron doped graphene. Interestingly, the peak in R_{xx} does not coincide with the zero crossing of R_{xy} , originating possibly due to electron and hole mobility difference, and inhomogeneity

in carrier density throughout the graphene sheet. Away from the CNP, the Hall resistance $R_{xy} = B_z/(ne)$ where n is the charge carrier density and e is the electron charge. Hall mobility away from CNP is given by $\mu = (ne\rho_{xx})^{-1}$, where ρ_{xx} is the longitudinal resistivity. Fig. 3.7 shows the variation in $B_z/(R_{xy}e)$ and $R_{xy}/(B_z\rho_{xx})$ versus time, which correspond to carrier density, n , and Hall mobility, μ , respectively, away from the CNP. Electron doping by Cs vapour exposure is clearly observed.

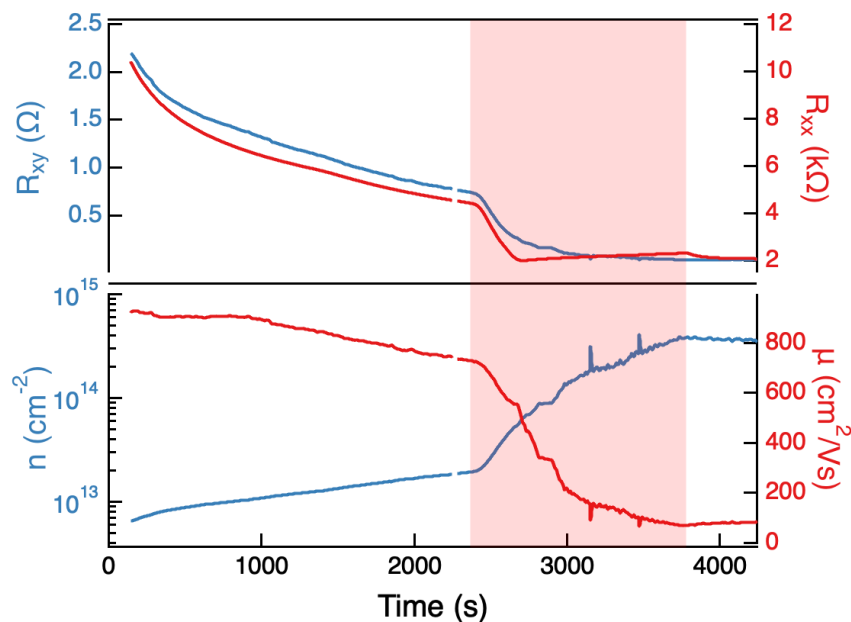


Figure 3.8: Doping graphene to ultra-high carrier density. The transverse, R_{xy} , and longitudinal, R_{xx} , resistances, carrier density n and Hall mobility μ versus time during Cs vapour exposure, measured by AC Hall effect. The rate of Cs doping is increased by heating the chip carrier (red shaded area).

Higher carrier density was achieved by increasing the Cs temperature, and thus Cs vapour pressure. The measured R_{xx} and R_{xy} versus time of a Hall bar during such a doping process

is presented in Fig. 3.8. The inferred charge carrier density n and Hall mobility μ are also shown versus time. Externally applied heat, see shaded red area in Fig. 3.8, increased the Cs vapour pressure in the cavity. The elevated temperature increased the rate of Cs doping and the final charge carrier density achieved. Over the course of different doping experiments, we increased the sample temperature up to 70° C in order to achieve ultra-high doping densities.

3.3 Magnetotransport of Ultra-High Doped Graphene

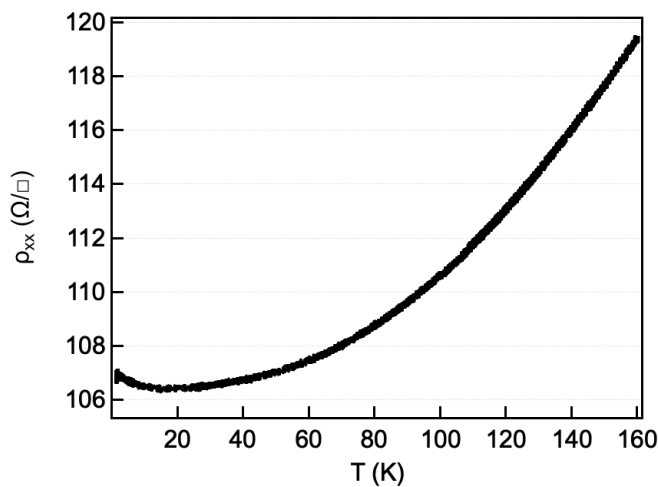


Figure 3.9: Resisitivity ρ_{xx} versus T of a representative Cs doped graphene sample.

Following the doping experiments inside the glovebox, samples are sealed and transferred to a cryostat with a variable temperature insert and superconducting solenoid for magnetotransport measurements. Fig 3.9 shows a representative measurement of a doped graphene Hall bar longitudinal resistivity ρ_{xx} versus temperature T , while the

sample is cooling down to 1.3 K.

3.3.1 Evidence of Ultra-High Doping

The final charge carrier density achieved depends on the temperature and duration of the doping process. Further magnetotransport experiments were conducted at high field ($B = 7$ T) and cryogenic temperature ($T = 1.3$ K). The Hall resistance R_{xy} versus B is shown in Fig. 3.10a for three samples (identified 1-3), showing a linear dependence of R_{xy} with respect to B in accord with the classical Hall effect. The slope $\partial R_{xy}/\partial B = (ne)^{-1}$ gives charge carrier densities n of 1.4×10^{14} , 2.0×10^{14} and 4.0×10^{14} cm^{-2} , for samples 1-3 respectively.

	n (cm^{-2})	μ ($\text{cm}^2\text{V}^{-1}\text{s}^{-1}$)	CsC _x	E_f (eV)	m_*/m_0
Sample 1	1.4×10^{14}	319	CsC _{27.3}	1.25	0.290
Sample 2	2.0×10^{14}	298	CsC _{19.1}	1.45	0.371
Sample 3	4.0×10^{14}	137	CsC _{9.5}	1.85	1.036

Table 3.1: Physical properties of highly doped graphene. Various experimentally measured and model parameters for samples 1, 2 and 3. Carrier densities n are calculated from the slope $\partial R_{xy}/\partial B$ at $T = 1.3$ K (Fig. 3.8a). The Hall mobility is determined from $\mu = R_{xy}/(B_z \rho_{xx})$. The CsC_x coverage is estimated from the ratio of the carrier density to the carbon atomic density in a graphene sheet, $x^{-1} = n/n_C$. The Fermi level E_F and effective mass m_* are determined from the experimental density n and a 3NNTB band structure calculation.

Table 3.1 presents a summary of the inferred charge carrier density n , Hall mobility μ and other properties of samples 1-3. The corresponding cesium carbon composition (CsC_x),

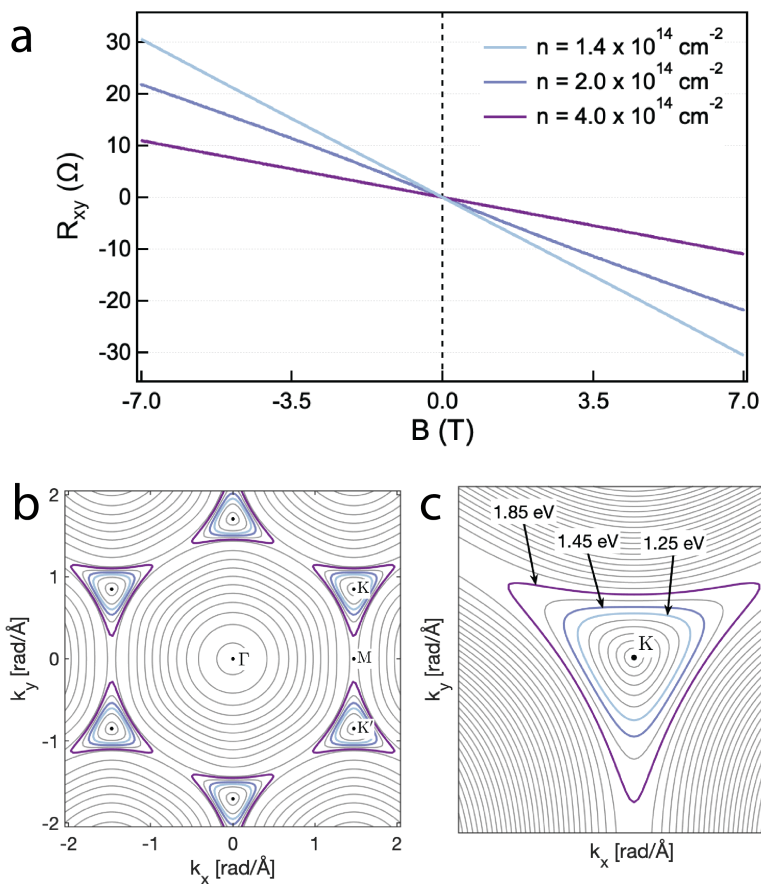


Figure 3.10: Confirming ultra-high carrier density via DC Hall. (a) The Hall resistance R_{xy} versus swept magnetic field B at $T = 1.3$ K for samples 1 to 3. The charge carrier density n is determined from the slope $\partial R_{xy}/\partial B$, indicating ultra-high carrier density. (b,c) The Fermi surfaces in the conduction π^* band corresponding to the carrier densities n of samples 1-3, labelled with corresponding Fermi energy E_F . A third-nearest-neighbour tight-binding (3NNTB) model was used for electronic structure calculation. The trigonal warping and proximity to the Lifshitz transition can be observed.

assuming complete ionization of samples 1-3 and a graphene carbon atom density of $n_C = 3.82 \times 10^{15} \text{ cm}^{-2}$ reveals the proximity of sample 3 to the CsC_8 stoichiometry previously achieved in UHV Cs-doping experiments [86]. To gain further insight into the electronic

properties of these heavily doped samples, a third-nearest neighbour tight-binding (3NNTB) calculation of electronic band structure using hopping and overlap parameters determined from ARPES [52] was performed and results are presented in Section 2.1. The model ignores Cs adatom interactions with the graphene lattice [86]. From the 3NNTB electronic structure and known density n , the Fermi level E_F (Figure 2.7) and normalized cyclotron effective mass $m_*/m_0 = \hbar^2(2\pi m_0)^{-1}\partial A_k/\partial E_F$ (Figure 2.8) was determined, where m_0 is the free electron mass and A_k is the area enclosed by the Fermi surface in the first BZ. Fig. 3.10b and c, show the Fermi surfaces determined from the 3NNTB calculations for samples 1-3. At such high doping levels, electronic structure in the vicinity of E_F is no longer well approximated by the Dirac cone approximation, with significant trigonal warping, band flattening, increase in cyclotron effective mass, and proximity to the Lifshitz transition where electron pockets meet at the M point. While the effective cyclotron mass m_* increases by 3.6 fold for samples 1-3, the Hall mobility μ decreases by 2.3 fold, indicative of non-trivial variation of electron scattering rates upon doping.

3.3.2 Magnetoresistance in Ultra-High Doped Graphene

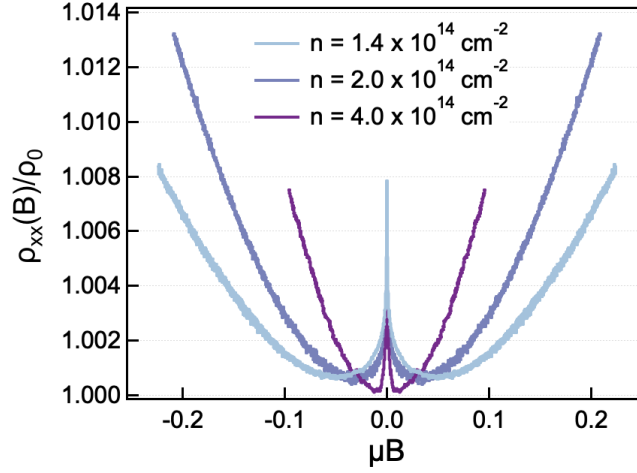


Figure 3.11: Normalized magnetoresistivity $\rho_{xx}(B)/\rho_0$ vs. μB for highly doped graphene samples 1-3 at temperature $T = 1.3$ K.

	n (cm^{-2})	μ ($\text{cm}^2\text{V}^{-1}\text{s}^{-1}$)	m_*/m_0	ρ_0 (Ω/\square)	A	$\delta n_{\text{rms}}/n$
Sample 1	1.4×10^{14}	319	0.290	135.4	0.167	0.6
Sample 2	2.0×10^{14}	298	0.371	106.1	0.304	0.8
Sample 3	4.0×10^{14}	137	1.036	114.6	0.823	1.3

Table 3.2: Magnetoresistance fit parameters of highly doped graphene. The magnetoresistance parameters ρ_0 , A and $\delta n_{\text{rms}}/n$ are determined by fitting the magnetoresistance (Figure 3.11) to Equation 3.1.

Significant magnetoresistance was observed, wherein the longitudinal resistance R_{xx} varied with magnetic field B . Fig. 3.11 shows the normalized longitudinal resistivity, $\rho_{xx}(B)/\rho_0$, as a function of B for samples 1 to 3. We observe a quadratic dependence of ρ_{xx}

versus B at high field, and a weak-localization peak at low field. Omitting the low field regions ($|B| < 0.6$ T, $|B| < 1$ T and $|B| < 2$ T for samples 1-3, respectively), the magnetoresistivity was fit to the quadratic form as,

$$\rho_{xx}(B) = \rho_0 [1 + A(\mu B)^2]. \quad (3.1)$$

following the effective medium theory of Ping et al. [58] introduced in Section 2.3. Here, A is a dimensionless coefficient and ρ_0 is the inferred zero-field resistivity $\rho_{xx}(0)$ in the absence of the quantum effects, namely weak-localization. Using $A = 0.5(n/\delta n_{\text{rms}})^{-2}$, the rms density fluctuation, δn_{rms} , the rms density fluctuation can be inferred [58]. The fit parameters are summarized in Table 3.2. This approximation yields $\delta n_{\text{rms}}/n = 0.6 - 1.3$ for samples 1-3, indicating the presence of significant charge carrier density fluctuation. However, charge density fluctuation is unlikely to be well described by a Gaussian distribution at high Cs adsorbate coverage, where phenomena including: i) adsorbate aggregation, ii) spatial variation in charge carrier scattering rates, and iii) localized regions crossing the density threshold for the Lifshitz transition, greatly complicate the analysis of magnetoresistance.

3.3.3 Weak Localization in Ultra-High Doped Graphene

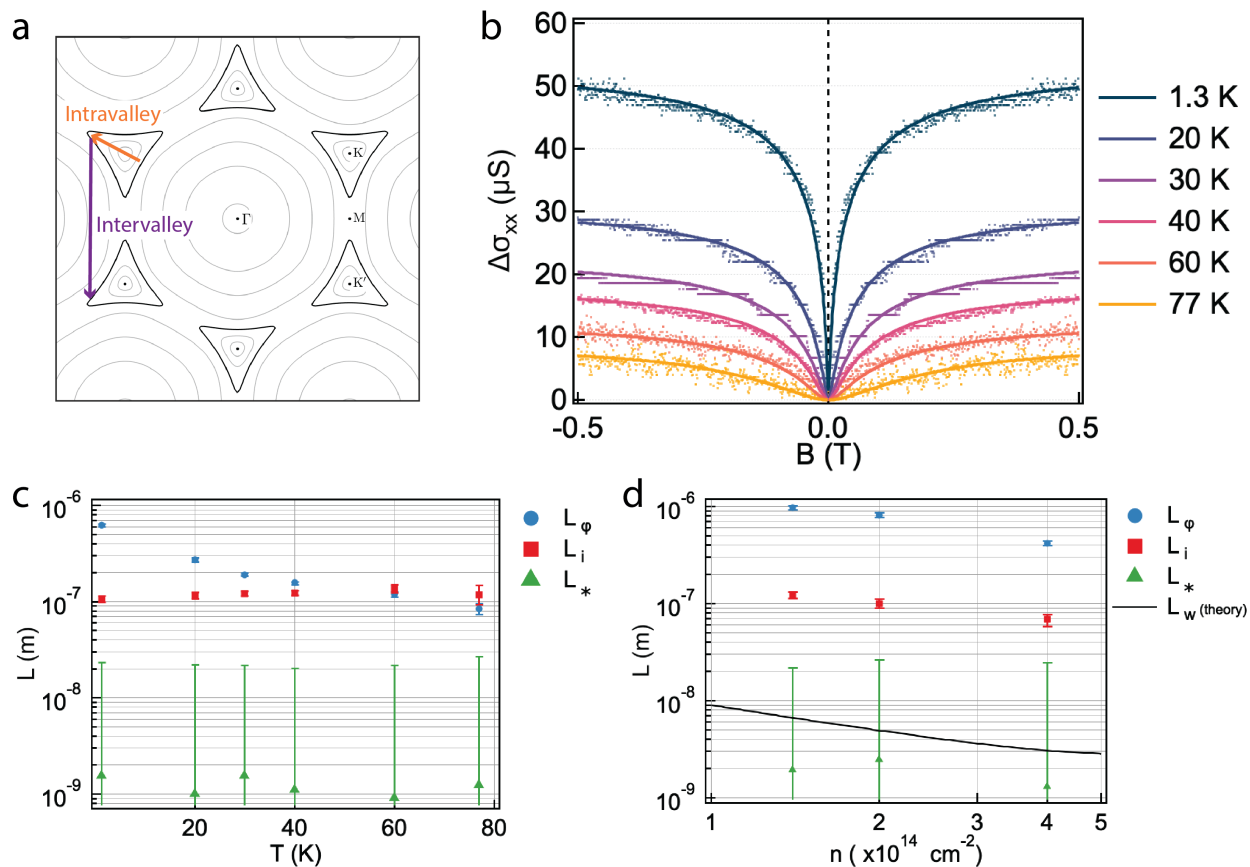


Figure 3.12: Weak-localization in ultra-high doped graphene. (a) Schematic of intervalley scattering and intravalley scattering processes in momentum space, associated with L_i and L_* , respectively. (b) Conductivity $\Delta\sigma_{xx}$ vs. B of sample 2, $n = 2.0 \times 10^{14} \text{ cm}^{-2}$, for different temperatures T . Experimental measurements (points) and fit to Eq. 2.24 (solid line) are shown. (c) Scattering lengths L_ϕ , L_i and L_* vs. density n for samples 1-3 at temperature $T = 1.3 \text{ K}$. The theoretical prediction for trigonal warping scattering length L_w agrees with the experimental intravalley scattering length L_* . (d) Scattering lengths L_ϕ , L_i and L_* of sample 2, $n = 2.0 \times 10^{14} \text{ cm}^{-2}$, vs. temperature T , with the characteristic decrease of L_ϕ with temperature increase.

All samples exhibited a weak localization (WL) peak in R_{xx} versus B in the low-field regime, shown in normalized form $\rho_{xx}(B)/\rho_0$ versus B in Figure 3.11 for samples 1-3. The temperature dependence of WL from $T = 1.2 - 77$ K was measured for sample 2 at $n = 2 \times 10^{14} \text{ cm}^{-2}$ and is presented in Figure 3.12b. The intervalley and intravalley scattering processes are illustrated schematically in Figure 3.12a at an energy where trigonal warping is prominent. For magnetic field $|B| < 0.5$ T, $\rho_{xy}(B) \ll \rho_{xx}(B)$ and thus $\sigma_{xx}(B) \approx \rho_{xx}^{-1}(B)$, therefore in the analysis of WL, the quadratic magnetoresistance background can be ignored. Numerical fit of the experimentally determined $\Delta\sigma_{xx}$ over $|B| < 0.5$ T to equation 2.24 was used to determine the scattering lengths versus doping density n at $T = 1.3$ K, presented in Figure 3.12c and versus temperature T at doping density $n = 2 \times 10^{14} \text{ cm}^{-2}$ presented in Figure 3.12d. The magnetoresistance $\rho_0 A \mu^2 B^2$ is less than 3% of the magnitude of the WL peak for $|B| < 0.5$ T, and error bars were determined by the fit parameter deviation that increases the sum of squares error between fit and measurement two-fold over that at optimum fit value.

The extracted scattering lengths and corresponding scattering times are listed in Table 3.3 for different carrier densities and in Table 3.4 for different temperatures. At $T = 1.3$ K, the phase coherence length $L_\phi = 0.4 - 1.0 \text{ } \mu\text{m}$, and the intervalley scattering length $L_i = 70 - 120 \text{ nm}$, in agreement with previous reports of WL in graphene [64,65,68]. The intervalley scattering length $L_* = 1.3 - 2.8 \text{ nm}$, at the lower limit of what can be determined by fit of Eq. 2.24 to the experimental $\Delta\sigma_{xx}$. The shortening of intravalley scattering length L_* , as

	n (10^{14} cm $^{-2}$)	L_ϕ (10^{-7} m)	L_i (10^{-7} m)	L_* (10^{-9} m)	τ_ϕ (10^{-11} s)	τ_i (10^{-13} s)	τ_* (10^{-16} s)
Sample 1	1.4	9.68	1.23	1.93	4.16	6.72	1.65
Sample 2	2.0	8.11	1.00	2.45	2.73	4.15	2.50
Sample 3	4.0	4.17	0.69	1.30	1.10	3.03	1.07

Table 3.3: Scattering parameters at different carrier densities. Scattering lengths obtained from fits and the corresponding scattering times for Cs doped graphene samples 1-3 at $T = 1.3$ K at different carrier densities.

well as L_ϕ and L_i with increasing carrier density n over the range $10^{11} - 1.5 \times 10^{13}$ cm $^{-2}$ has been previously observed in monolayer graphene [68]. The intravalley scattering rate is expressed as a combination of two scattering mechanisms: the scattering induced by chirality breaking defects and scattering induced by trigonal warping of the Dirac cones (Equation 2.25) [69]. Chirality breaking defects were identified as the dominant intravalley scattering mechanism in previous experiments with carrier density $n = 10^{11} - 1.5 \times 10^{13}$ cm $^{-2}$, with the prediction that trigonal warping is the dominant source of intravalley scattering at densities of $n \approx 10^{14}$ cm $^{-2}$ [68]. Indeed, L_* was sufficiently short to be neglected in the analysis of WL in Li-doped graphene monolayers at $n = 0.5 - 2.0 \times 10^{14}$ cm $^{-2}$ [96] and Li-doped bilayers at $n = 2.0 \times 10^{14}$ cm $^{-2}$ [27]. We compare our the observed intravalley scattering length L_* with the analytic form of Equation 2.27. As seen in Figure 3.12c, the experimentally observed intravalley scattering length is in good agreement with the analytical model of McCann et al. [62] for trigonal warping, $L_* \approx L_w$. Notice that this model is based on a 1NN approximation and limited to low Fermi energies near the Dirac cone. A theoretical explanation of scattering

T(K)	L_ϕ (m)	L_i (m)	L_* (m)	τ_ϕ (s)	τ_i (s)	τ_* (s)
1.3	6.24×10^{-7}	1.05×10^{-7}	1.55×10^{-9}	1.61×10^{-11}	4.55×10^{-13}	9.96×10^{-17}
20	2.72×10^{-7}	1.16×10^{-7}	1.00×10^{-9}	3.06×10^{-12}	5.57×10^{-13}	4.13×10^{-17}
30	1.91×10^{-7}	1.21×10^{-7}	1.55×10^{-9}	1.50×10^{-12}	6.02×10^{-13}	9.91×10^{-17}
40	1.58×10^{-7}	1.24×10^{-7}	1.10×10^{-9}	7.94×10^{-13}	6.32×10^{-13}	4.98×10^{-17}
60	1.20×10^{-7}	1.35×10^{-7}	9.12×10^{-10}	5.97×10^{-13}	7.59×10^{-13}	3.47×10^{-17}
77	8.47×10^{-8}	1.18×10^{-7}	1.23×10^{-9}	3.02×10^{-13}	5.87×10^{-13}	6.37×10^{-17}

Table 3.4: Scattering parameters at different temperatures. Scattering lengths obtained from WL fits to the measured $\Delta\sigma_{xx}(B)$ and the corresponding scattering times for sample 2 at different temperatures.

lengths near the vHS is yet to be developed. Finally, we note that the reduction in WL amplitude with increasing temperature T is attributable to the shortening of the phase coherence length L_ϕ , while L_i and L_* show comparatively weak temperature dependence, in accord with previous experimental observations [27, 64–66, 68, 69, 96].

3.4 Raman Spectroscopy of Ultra-High Doped Graphene

Beyond charge transport measurements, Raman spectroscopy provides an independent experimental probe of charge carriers in graphene via electron-phonon coupling. Raman Stokes spectra were measured after Cs doping was completed and sample cavities sealed for an independent series of samples. A Renishaw inVia Raman microscope with 1800 l/mm grating and an Innovative Photonic Solutions laser at 785 nm with 90 mW output was

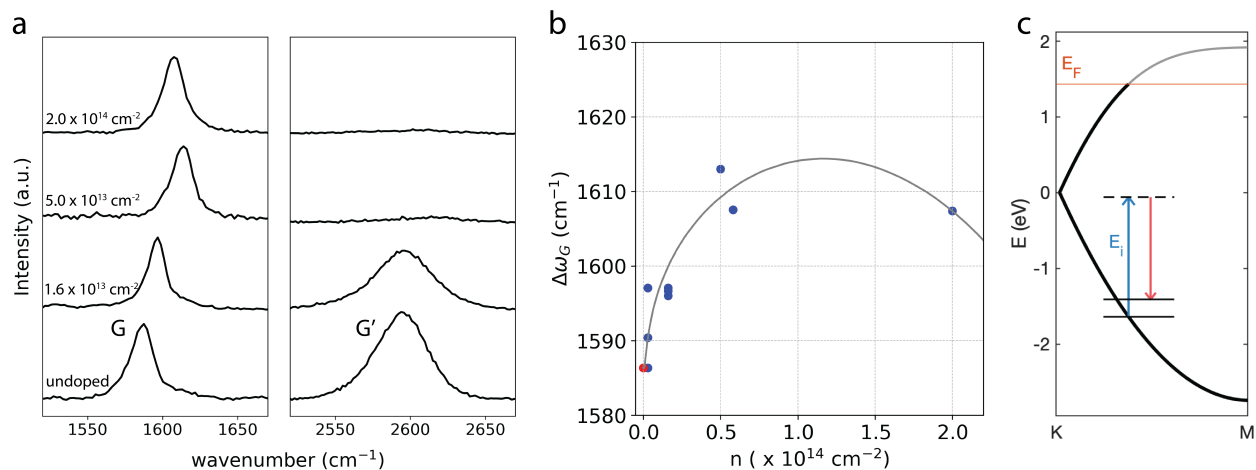


Figure 3.13: Raman spectroscopy of ultra-high doped graphene (a) Raman spectra of doped graphene samples with varying carrier densities in the spectral regions of the G -peak and $G'(2D)$ -peak regions. (b) Evolution of the experimentally measured G -peak position ω_G vs. carrier density n (dots, blue for Cs doped samples and red for native doping). The theoretical model of G -peak shift $\Delta\omega_G$ given by Eq. 3.2 (grey line) with $\alpha = 0.36$ is in good agreement with experiment (c) Illustration of the non-resonant Raman scattering process, with Fermi level E_F corresponding to a carrier density $n = 2.0 \times 10^{14} \text{ cm}^{-2}$ (orange line), and the corresponding occupied electronic states highlighted (black) with a 3NNTB model of electronic structure. The non-resonant Raman scattering process with an incident photon energy $E_i = 1.58 \text{ eV}$ is illustrated.

used. For each measurement 5 accumulations were taken with 1 second exposure at full laser power. Fig. 3.13a presents the room temperature Raman spectra, obtained with $\lambda = 785 \text{ nm}$ ($\hbar\omega_i = 1.580 \text{ eV}$) excitation, of several samples with different doping densities n determined from AC Hall measurements. The Raman G -peak position, initially at 1586 cm^{-1} for pristine samples with native doping, shifts up with doping and reaches a peak value of 1613 cm^{-1} , followed by a slight downshift with further doping (Fig. 3.13b) in

qualitative agreement with previous experimental observations of ionic liquid gated graphene [71, 74, 107], Rb-doped graphene on SiO₂ [26], and Cs-doped graphene on Ir [77], and first-principles calculations of the E_{2g} Γ phonon hardening / softening [78]. Further insight can be obtained by comparison of the observed G -peak shift, $\Delta\omega_G$, relative to pristine samples with the model of Hell et al. [77] introduced in Section 2.4.

$$\Delta\omega_G = \alpha\Delta\omega_S + \Delta\omega_D, \quad (3.2)$$

where the static contribution, $\Delta\omega_S$, is associated with lattice expansion and adiabatic electron-phonon coupling, α is the ratio of static G -peak shift of graphene in the presence of graphene-substrate interactions to that of an ideally decoupled graphene, and the dynamic contribution, ω_D , is associated with non-adiabatic electron-phonon coupling effects. The static contribution $\Delta\omega_S$ is estimated with an analytic approximation to numerical calculation and the dynamic contribution $\Delta\omega_D$ is determined by numerical calculation of the electron-phonon coupling, [78], using 3NNTB electronic structure [52] and the deformation potential, $D^2 = 63.1 \text{ eV}^2/\text{\AA}^2$ derived from ARPES analysis of Cs doped graphene [77] (see Section 2.4). A fit of the experimentally observed $\Delta\omega_G$ to the model of equation 3.2, shown in Fig. 3.13b gives agreement with $\alpha = 0.36$. In comparison with Cs doped graphene on Ir (111), where $\alpha = 0.18$ was found for the G -peak shift with doping [77], the interaction of graphene transferred to quartz suppresses lattice expansion

to a lesser degree than epitaxial graphene on Ir (111).

The high charge carrier density also results in a change in the Raman peak intensities. As shown in Fig. 3.2a, increased Cs-doping suppresses the $G'(2D)$ peak intensity relative to the G peak intensity. This trend has been previously observed in ionic liquid gated doped graphene [74, 94] and Rb-doped graphene [26]. We used pump excitation at $\lambda = 785$ nm ($E_i = \hbar\omega_i = 1.580$ eV) to minimize fluorescence, as the graphene Raman spectrum was collected through the 500 μm thick quartz substrate. At this pump excitation, $E_i < 2|E_F|$ as illustrated in Fig. 3.2c, and Raman scattering is strongly detuned from resonance. Under the highly detuned conditions of our experiments, the $G'(2D)$ peak intensity is expected to be diminished to a greater extent than the G peak intensity as detuning increases with doping, since the $G'(2D)$ and G processes are 2nd order and 1st order, respectively. In summary, Raman spectroscopy provides an independent confirmation of the high doping achieved in Cs doped graphene produced in this study.

3.5 Conclusion

We have demonstrated a comparatively facile method utilizing an inert glove box environment for doping graphene to a high charge carrier density, up to 4×10^{14} cm^{-2} , achieved by encapsulating an alkali vapour source in a flip-chip assembly. The method permits *in situ* charge transport characterization during alkali doping, and enables further experimental characterization by methods such as magnetotransport and Raman

spectroscopy. The charge carrier density reached outside of a UHV environment by this method exceeds previous reports, and is thus anticipated to enable studies of highly doped few-layer materials, complementing ARPES studies of highly doped systems on metallic substrates. The charge transport properties of highly doped graphene at the Lifshitz transition has not been fully investigated despite predictions of non-trivial many-body phenomena [82]. The extension of the doping method presented here to other alkali dopants and target materials and devices may provide a new means of exploring the physics of highly doped low-dimensional systems: such as heavily doped black phosphorus which have been shown to exhibit bandgap modulation, closure, and inversion owing to an unusually strong Stark effect [108, 109] or alkali doped C_{60} to synthesize high critical temperature superconductors [110]. In terms of commercial applications, the flip-chip method can be implemented to dope microfabricated ion traps designed for quantum computing [111].

Chapter 4

Franckeite Review

We now turn to the second part of this bipartite thesis, concerned with the material franckeite. Franckeite is a naturally occurring sulfosalt mineral found in Bolivia and first described by Stelzner [112]. This van der Waals superlattice is composed of alternating incommensurate 2D layers, specifically the Q layer with a lead sulfide-like (PbS) structure and the H layer with a tin disulfide-like (SnS₂) structure. Franckeite has garnered interest as a natural vdW superlattice that can be exfoliated down to few layers offering a more straightforward avenue for fabricating 2D superlattices, in contrast to layer by layer assembly. Within this chapter, we present a brief review of prior studies about franckeite, to provide context for the original experiments detailed in Chapter 5.

4.1 Crystal Structure of Franckeite

Makovicky et al. investigated the crystal structure of franckeite using X-ray diffraction [113]. The layered structure of franckeite consists of alternating H and Q layers as shown in Figure 4.1. Q layers are tetragonal PbS slabs with SnS, SbS substitutions and are 4 unit layers thick. On the other hand, H layers are hexagonal SnS₂ slabs with FeS₂ substitutions and are 1 unit layer thick. From the energy-dispersive X-ray spectroscopy of franckeite [114] the chemical composition of the H and Q layers have been estimated.



The lattice parameters describing the Q and H sublattices [113] are given in Table 4.1 where a , b and c are the unit cell lengths in the crystallographic directions \mathbf{a} , \mathbf{b} and \mathbf{c} , respectively. The angles α , β and γ are the the angles between \mathbf{b} and \mathbf{c} , \mathbf{a} and \mathbf{c} , and, \mathbf{a} and \mathbf{b} directions, respectively. The directions of the \mathbf{a} and \mathbf{b} vectors are reported to be parallel for the sublattices, while \mathbf{c}_Q and \mathbf{c}_H are different. The stacking direction is perpendicular to the $(\mathbf{a} \times \mathbf{b})$ plane.

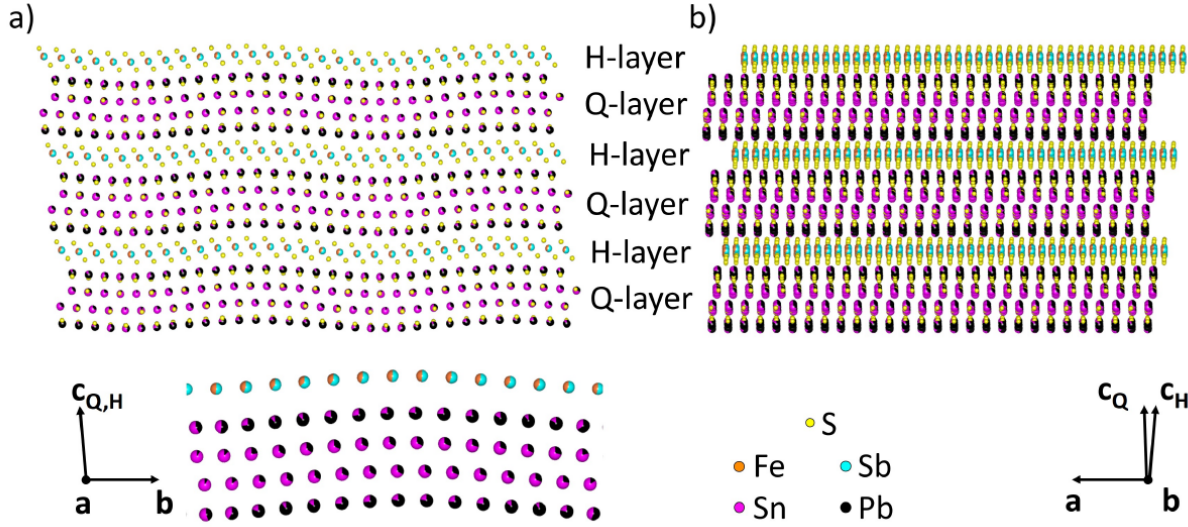


Figure 4.1: Crystal structure of franckeite as described by Makovicky et al. [113]. Projections along \mathbf{a} and \mathbf{b} directions are given in panels (a) and (b), respectively. The anisotropic displacive modulation is shown.

Q layer	H layer
$a_Q = 5.815 \text{ \AA}$	$a_H = 3.672 \text{ \AA}$
$b_Q = 5.873 \text{ \AA}$	$b_H = 6.275 \text{ \AA}$
$c_Q = 17.366 \text{ \AA}$	$c_H = 17.447 \text{ \AA}$
$\alpha_Q = 94.98^\circ$	$\alpha_H = 95.26^\circ$
$\beta_Q = 88.43^\circ$	$\beta_H = 95.45^\circ$
$\gamma_Q = 89.97^\circ$	$\gamma_H = 89.97^\circ$

Table 4.1: Lattice parameters of H and Q layers from [113]

Vertical stacking of the hexagonal and tetragonal layers results in an incommensurate structure. The commensurate supercell has a length of $15.5b_Q = 13.5b_H = 91\text{\AA}$. A common displacive modulation with wavevector in the \mathbf{b} direction and displacement in the \mathbf{c} direction is identified and it presents as a wave-like corrugation as seen in Figure 4.1a. The modulation vector is given as $q \approx 0.128b_Q^* \approx 0.137b_H^*$ with a modulation length of $1/q \approx 45.8\text{\AA}$. Notice that the length of the supercell is approximately double the modulation length. The correlation suggests that the incommensurability and the displacive modulation are related.

The source of the displacive common modulation is attributed by Frisenda et al. [115] to the spatial modulation of the van der Waals interaction that emerges from the incommensurability of the franckeite lattice. Strain analysis of the HRTEM measurements reveal a spatially modulated in-plane strain with a periodicity that matches the out-of-plane rippling of the lattice.

4.2 Band Structure of Franckeite

Determining the band structure of franckeite poses significant difficulties. Firstly, addressing the lattice mismatch between the H and Q layers necessitates the consideration of a sizable supercell, leading to significant computational costs. Introducing substitutional defects that are present in both layers to the model further compounds these challenges. Given that franckeite contains heavy atoms, accounting for the influence of spin-orbit coupling becomes

imperative. Additionally, accommodating the displacive modulation is crucial. As of now, a comprehensive calculation of franckeite's band structure that encompasses these aspects remains pending.

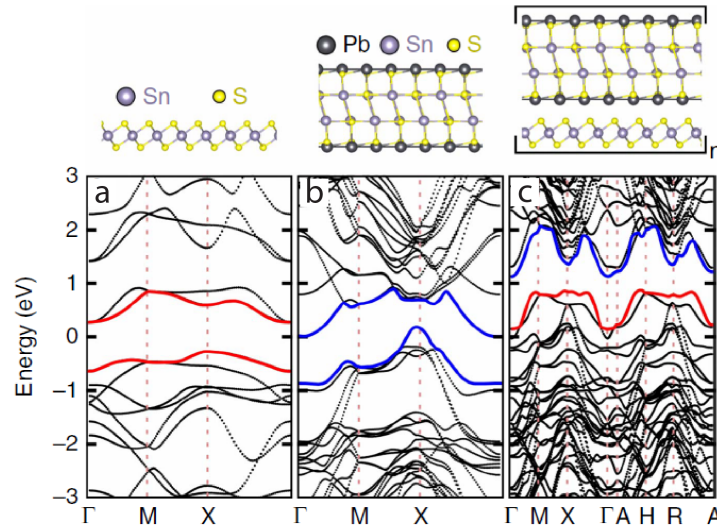


Figure 4.2: DFT calculated band structure of an H layer (a), a Q layer (b) and bulk franckeite (c). Reprinted with permission from Ref [116].

Some qualitative predictions of the band structure of franckeite have been reported by Molina-Mendoza et al. using density functional theory (DFT) calculations [116]. The bands for the individual H and Q layers, as well as the composite franckeite superlattice, are depicted in Figure 4.2. Intriguingly, the wavefunctions for the valence and conduction bands are attributed respectively to the H and Q layers, resembling a type-II staggered gap multiple quantum well structure. In addition to an indirect fundamental gap, franckeite is predicted to be heavily p-type doped to the point of being described as metallic. While the presented

DFT studies capture crucial characteristics of the franckeite band structure, the lattice structure was simplified for the sake of computational efficiency. In this approach, however, the incommensurability of the lattice, the prevalent out-of-plane modulation, substitutional defects, and the impact of spin-orbit coupling are ignored.

4.3 Optical Properties of Franckeite

Various research groups have measured the optical characteristics of franckeite. Absorption spectra of franckeite have been documented within the near infrared range ($\lambda = 500\text{-}3000$ nm) [116]. In these experiments, samples were prepared by liquid phase exfoliation. The observed absorption spectrum (Figure 4.3a) shows a reduction in absorption as wavelength increases with a distinctive absorption band centered at 2900 nm. In the same study, a photoresponsivity of 100 mA W^{-1} for 30 mW cm^{-2} laser intensity was recorded for a few layer franckeite based photodetector, produced by mechanical exfoliation from a bulk franckeite crystal.

The photoluminescence analyses of franckeite [117, 118] reveal two peaks at 590 nm (2.1 eV) and 740 nm (1.66 eV) as shown in Figure 4.3b. The studies have noted the agreement of these emission peaks with the optical band gaps of SnS_2 and Sb_3S_2 , respectively, but a definitive attribution of the latter spectral feature requires further experimental study. Notably, the optical absorption spectrum appears to be dominated direct optical transitions in the SnS_2 layer [116–118].

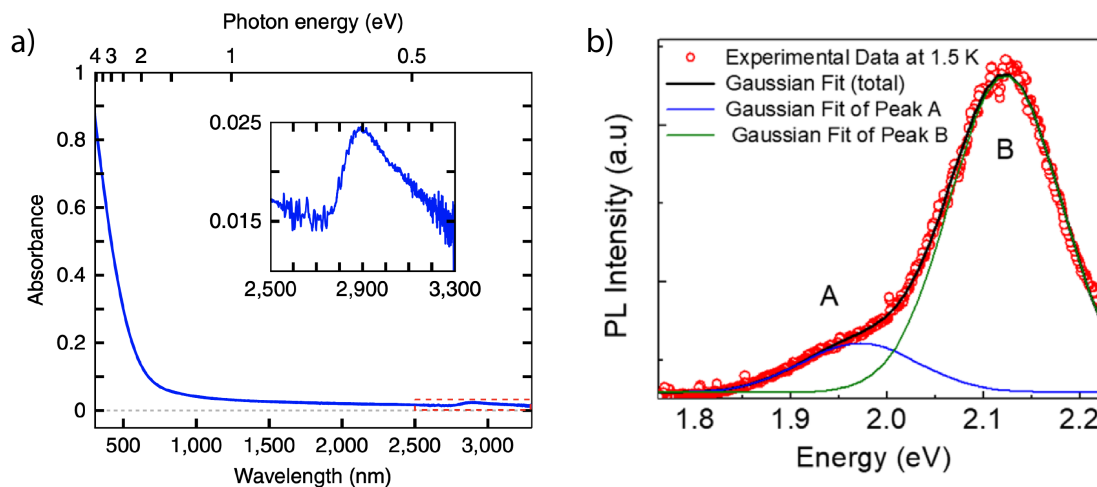


Figure 4.3: (a) Absorption spectra of franckeite showing a distinctive absorption band at 2900 nm. Reprinted with permission from Ref [116]. (b) Photoluminescence spectra of franckeite showing two peaks at 590 nm (2.1 eV) and 740 nm (1.66 eV). Reprinted with permission from Ref [117].

Flake thickness dependent optical contrast study of franckeite has unveiled refractive index components $n = 2.5 - 4$ and $\kappa = 0.4 - 1.5$ in the visible spectrum ($\lambda = 450-750$ nm) [119]. No sharp features such as exciton peaks were observed in the visible spectrum, in contrast to the sharp excitonic features often observed in transition metal dichalcogenides [119].

Moreover, the anisotropic franckeite structure due to the displacive modulation in the **b** direction is expected to impart optical anisotropy. Differential reflectance measurements using linearly polarized light at varying angles reveal linear dichroism in franckeite, with greater optical absorption observed for polarization is aligned parallel to the wavevector of the displacive modulation [115]. These experiments were conducted by direct comparison of

optical reflectance spectra and HRTEM of exfoliated franckeite flakes.

4.4 Charge Transport in Franckeite

Electronic transport in few layer franckeite was investigated by Velicky et al. [114]. Attempts to measure the electrical conductivity of single layer franckeite (one H/Q pair) have been unsuccessful to date. Nevertheless, experiments on bilayer and few layer franckeite devices demonstrate field effect. The bilayer devices present higher conductivity dependence to gate voltage. Nonlinear current-bias characteristics observed in some samples suggest the presence of a Schottky barrier between franckeite and the metallic contacts. Temperature dependence of conductivity have also been probed by Velicky et al. [114] and Ray et al. [118]. Clear Arrhenius behaviour was observed with activation energies that decrease with increasing number of franckeite layers. The behaviour is attributed to dopant impurities that introduce states in the band gap and electronic transport through hopping conduction.

Anisotropy in the electronic properties of franckeite have been demonstrated in the experimental work of Frisenda et al [115]. For this purpose, they fabricated several pairs of electrical contacts at varying angles to the long edge of the exfoliated flake, the optical microscopy image of the device is shown in Figure 4.4a. Angle-dependent conductivity results show that the conductivity aligning with the long edge is nearly twice as high as the conductivity perpendicular to it (Figure 4.4b). The direction of ripples was identified to be parallel to the long edge of the flake via strain analysis of the HRTEM images. The results

suggest that carriers experience a higher scattering rate along the direction perpendicular to the ripples. These findings elegantly illustrate the influential role of spatial modulation anisotropy on the electronic transport of franckeite.

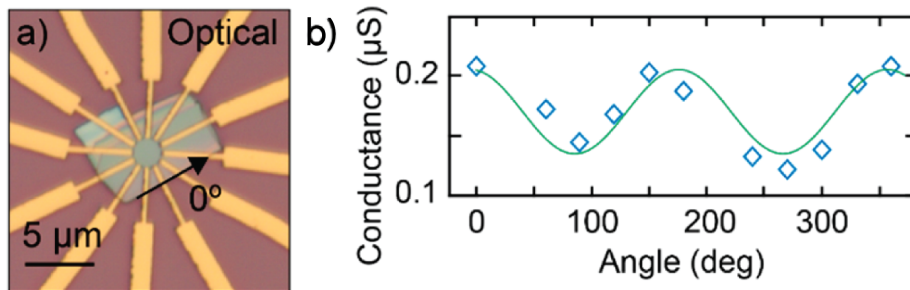


Figure 4.4: Anisotropic electronic transport in franckeite. (a) Optical microscopy image of the device. Several pairs of electrical contacts at varying angles to the long edge of the exfoliated flake are fabricated. (b) Angle-dependent conductance show anisotropy due to the modulation in the franckeite lattice. Reprinted with permission from Ref [115].

In summary, much remains unknown about the electronic structure and charge transport properties of van der Waals superlattices such as franckeite, motivating the original work described in Chapter 5.

Chapter 5

Characterization of the Electronic

Structure of Franckeite

Franckeite is a naturally occurring van der Waals superlattice structure. Franckeite has attracted attention due to its semiconducting and electrochemical properties, as well as the possibility of exfoliation into thin flakes. Exfoliated franckeite have been incorporated into p-n junction photodiodes [116], photodetectors [117, 118] and field effect devices [114].

The band structure of franckeite has been calculated by DFT [114, 116] under approximations necessary to reduce computational requirements which consequently neglects potentially important phenomena such as incommensurate lattice, displacive modulation and chemical ordering. There have been no experimental investigations of franckeite band structure to date.

The thermoelectric capabilities of nanoscale materials have been a subject of investigation. Hicks and Dresselhaus have proposed using quantum-well superlattice structures to enhance the performance of thermoelectric materials [120]. Additionally, enhanced thermoelectric figures of merit have been observed in thin-film thermoelectric superlattice structures in comparison to their bulk counterparts [121]. Thermoelectric figure of merit of franckeite constituent materials PbS [122] and SnS₂ [123] have been investigated, whereas, thermoelectric performance of franckeite, a 2D superlattice with a multiple quantum well structure, is yet to be explored.

In this chapter, we introduce a series of new experimental findings regarding franckeite. These include atomic structure measurement using state-of-the-art high-angle annular dark-field (HAADF) scanning transmission electron microscopy (STEM) and atom probe tomography (APT). The electronic structure of franckeite is investigated through angle-resolved photoemission spectroscopy (ARPES) and in-plane effective mass values resulting from an anisotropic valence band are presented. By examining the optical reflectance hyperspectra of franckeite with varying thickness, we are able to discern its reflectivity characteristics and identify a direct optical band gap. Furthermore, thermoelectric assessments of exfoliated franckeite demonstrate a Seebeck coefficient $S = +45 \mu\text{V}/\text{K}$, confirming the presence of intrinsic p-type carriers. Collectively, these results contribute to a more profound understanding of the fundamental properties of this natural van der Waals superlattice.

5.1 Characterization of Franckeite

The franckeite crystals employed in our investigations originate from a single mineral specimen extracted from the San José mine in Bolivia. As the crystals are of natural origin, it is crucial to thoroughly examine the properties of the sample before conducting any experiments. In the subsequent sections, we elaborate on the various techniques used for characterizing the franckeite samples

5.1.1 Atom Probe Tomography

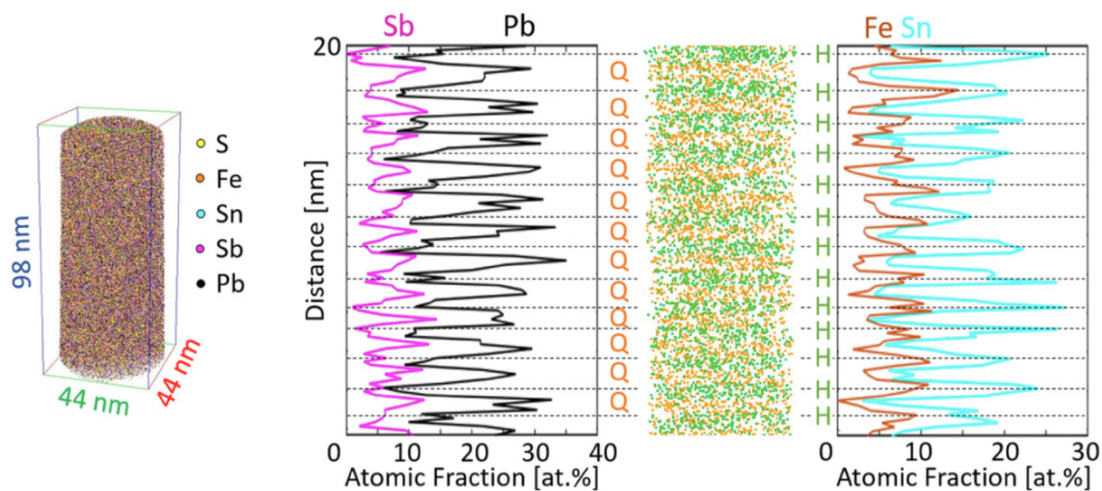


Figure 5.1: Atom probe tomography of franckeite. (a) Reconstructed volume of a franckeite tip prepared for APT. (b) The atomic fraction plots for elements Sb and Pb (on the left) and Fe and Sn (on the right). Reprinted with permission from Ref [124]

We start the characterization of franckeite by local electrode atom probe (LEAP) tomography, an advanced form of atom probe tomography (APT) analysis [125]. LEAP is a powerful APT variant that is used for compositional mapping of samples in three dimensions with good elemental sensitivity and spatial resolution approaching the atomic layer limit. For preparation of the franckeite samples, a Thermo Scientific Helios G4 UXe DualBeam Plasma-FIB [Xe⁺] and a Zeiss NVision 40 [Ga⁺] were used. Standard methods for obtaining cross-sectional samples were utilized, after which annular milling was employed to create needle-shaped tips. The samples were derived from flakes with surfaces parallel to the van der Waals gap plane so that the ultimate tip orientation would be perpendicular to this plane. In the reconstruction, the pole center and its diameter were picked manually to achieve spatial distributions of elements in agreement to the compositions of franckeite layers. Figure 5.1a shows the reconstructed volume of a franckeite tip.

The atomic maps were obtained using a LEAP 4000X HR at 24 K, under a vacuum of 3×10^{-11} Torr, with a UV pulse photoexcitation ($\lambda = 355$ nm, 5 pJ 50 kHz), delivering 0.002 ions/pulse. The atomic fraction plots for elements Sb and Pb (on the left) and Fe and Sn (on the right) are depicted in Figure 5.1b. The concentrations of (Pb, Sb) and (Fe, Sn) are spatially anticorrelated, identifying the Pb- and Sb-rich Q-layers and the Sn- and Fe-rich H-layers.

5.1.2 High-Angle Annular Dark-Field STEM

Scanning transmission electron microscopy (STEM) is an imaging technique that provides atomic resolution by combining the features of scanning and transmission electron microscopy. The utilization of a high-angle annular dark-field (HAADF) detector permits compositional analysis since high-angle electron scattering is proportional to the square of atomic number, Z^2 , per the elastic Rutherford scattering cross-section [126]. All STEM techniques are sensitive to specimen thickness, therefore, it is important to prepare an adequately thin sample to obtain electron transparent lamella.

Similar to the sample preparation for APT, a Thermo Scientific Helios G4 UXe DualBeam Plasma-FIB [Xe^+] and a Zeiss NVision 40 [Ga^+] were utilized. Perpendicular milling was applied to produce franckeite lamella, with a sample of 86 layer thickness used for the measurements reported here. HAADF-STEM images were collected using an FEI Titan 80-300 Cubed TEM operated at an acceleration voltage of 200 kV with a 19 mrad convergence semi-angle and a 64 mrad inner collection semi-angle of the dark-field detector. To avoid confusion that can stem from two different sublattice systems present in franckeite, the viewing directions are given in Cartesian coordinates. \mathbf{a} is defined along [100] and \mathbf{b} is assigned to [010] since the angle between \mathbf{a} and \mathbf{b} is 90° to within experimental accuracy in STEM imaging. As a result, the van der Waals stacking is approximately in the [010] direction.

Figure 5.2 shows the HAADF-STEM images of franckeite in two different viewing

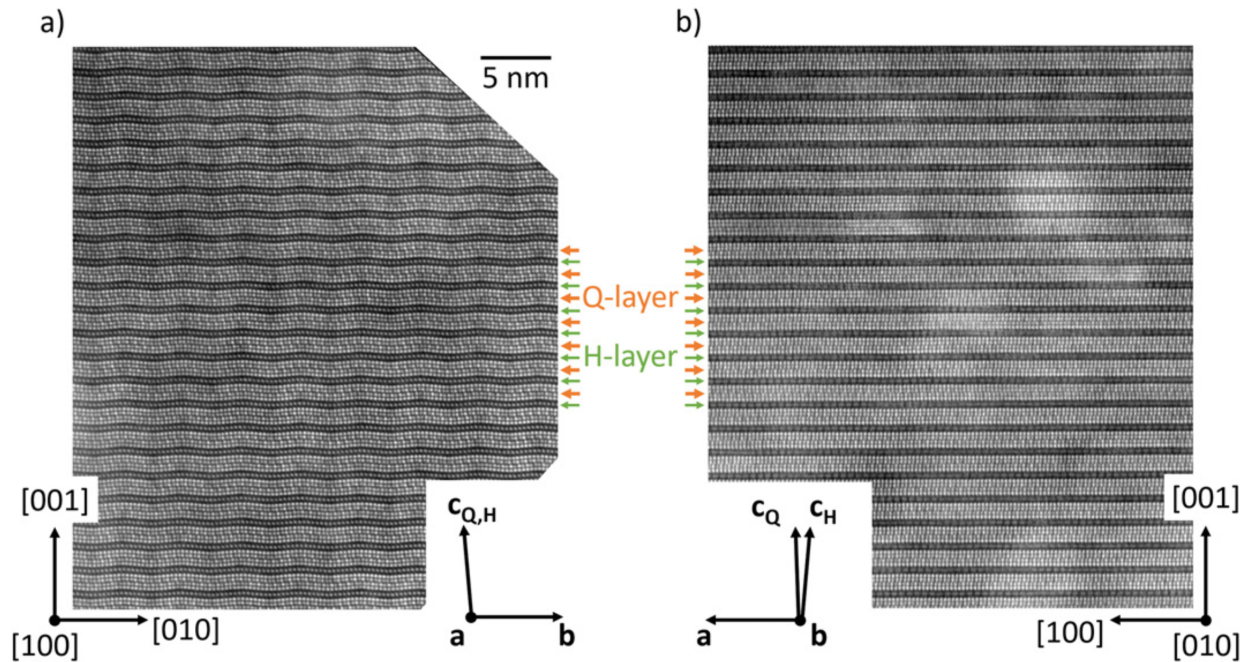


Figure 5.2: High-angle annular dark-field STEM of franckeite in viewing directions (a) [100] and (b) [010]. The displacive modulation with amplitude in [001] and wavevector along [010] is visible in the [100] viewing direction. Reprinted with permission from Ref [124].

directions. Repeating H and Q layers are distinguishable and the anisotropic displacive modulation is apparent in the [100] viewing direction. Next we take a closer look at the variation of contrast within the layers. Figure 5.3 shows each layer in a temperature contrast scale wherein shades of blue and yellow correspond to low and high electron intensity, respectively. Within the Q layer, intensity modulation correlated with displacive modulation is observed in the outer Q layers. Atomic columns exhibiting higher electron scattering intensity are evident in the convex domains (indicated by black arrows) of the displacive modulation, whereas the concave regions host atomic columns with

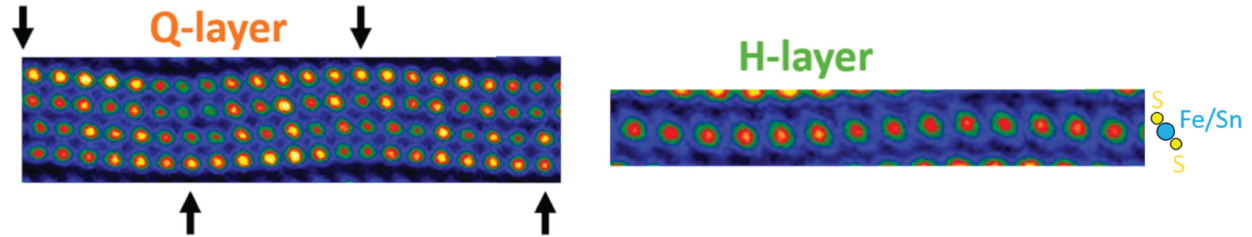


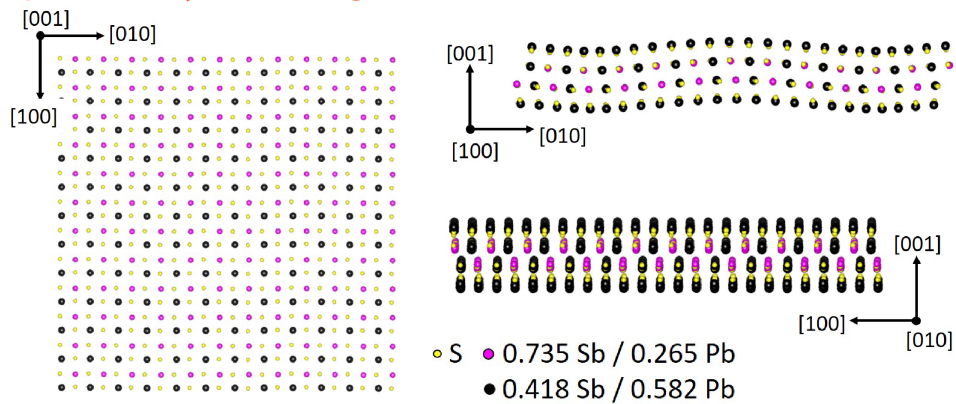
Figure 5.3: HAADF STEM of H and Q layers presented in temperature contrast scale wherein shades of blue and yellow correspond to low and high intensity, respectively. Modulation dependent intensities are present in both layers. The cartoon image shows the proposed model for the H layer. Reprinted with permission from Ref [124].

comparatively lower intensity. This observation implies that the convex regions possess elevated average Z and, consequently, are rich in Pb ($Z = 82$), with concave regions are rich in Sb ($Z = 51$).

Within the H layer two low intensity atomic columns can be spotted next to each high intensity column. These high and low intensity columns represent Fe/Sn and S columns, respectively, in agreement with the model proposed by Makovicky et al. [113].

An in depth analysis of franckeite HAADF STEM results can be found in Ref [124], including imaging along other directions, discussion regarding H and Q layer stacking and stacking faults, as well as a proposed atomic ordering model for H and Q layers arrived at by combining STEM and APT observations. The proposed atomic ordering is summarized in Figure 5.4.

Proposed Q-layer ordering



Proposed H-layer ordering

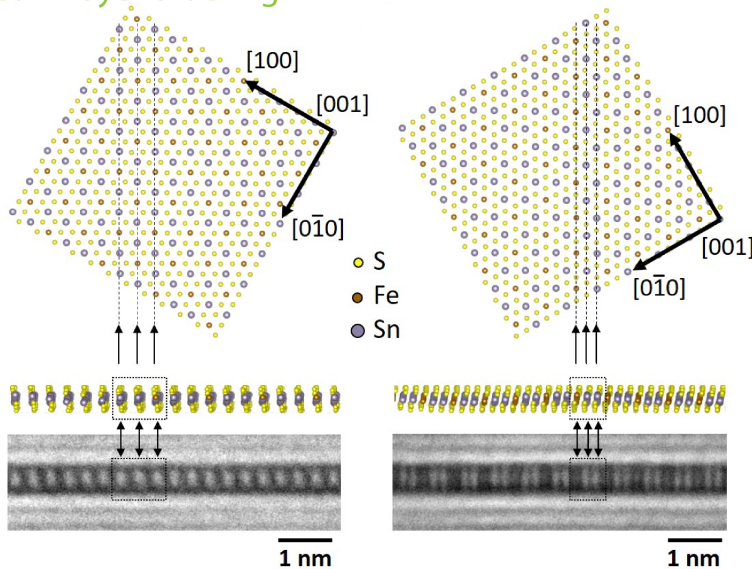


Figure 5.4: Proposed atomic ordering in Q (upper panel) and H (lower panel) layers. Reprinted with permission from Ref [124].

According to the refined atomic ordering model, the Q layer has Pb-rich cationic sites in the outer atomic layers, and Sb-rich cationic sites in the inner layers. The ordering of Pb-rich and Sb-rich sites of an inner Q layer is shown along the $[010]$ viewing direction in Fig. 5.4.

As for the H layer, an ordered array of Fe-rich and Sn-rich cationic sites is proposed, with the ordering corresponding to alternating cationic species, inferred from the modulation of electron scattering intensity as franckeite is rotated about the [001] axis, as shown in Fig. 5.4. The effects of this proposed chemical ordering on the electronic band structure of franckeite is yet to be investigated.

5.1.3 Angle Resolved Photoemission Spectroscopy

Angle resolved photoemission spectroscopy (ARPES) is a technique utilized to quantitatively map the electronic band structure of a material. ARPES is an extension of the photoelectric effect, wherein a sample is excited by photons, and through precise measurement of the emitted photoelectron kinetic energy and exit angle, the binding energy and momentum components of the electrons at the surface of the sample under study are deduced by application of conservation of energy and momentum. The detailed procedure by which band energy versus momentum $E(\mathbf{k})$ is inferred from the measured photoelectron kinetic energy E_{kin} and exit angle is described in [127]. In brief, the measured photoelectron kinetic energy E_{kin} is related to the wavevector \mathbf{K}_F via

$$E_{kin} = \frac{\hbar^2 \mathbf{K}_F^2}{2m_0}. \quad (5.1)$$

The relationship between E_{kin} , the incident photon energy $h\nu$, the workfunction Φ and the band energy $E(\mathbf{k})$ is given by

$$E_{kin} = h\nu - \Phi - E(\mathbf{k}). \quad (5.2)$$

The in-plane wavevectors are determined by momentum conservation to be

$$\mathbf{K}_{F,\parallel} = \mathbf{k}_{\parallel} = k_x \hat{\mathbf{x}} + k_y \hat{\mathbf{y}}. \quad (5.3)$$

ARPES experiments of bulk franckeite were performed at the Soleil Synchrotron in France on the ANTARES (**A**nalysis **N**ano-spo**T** **A**ngle **R**esolved photo**E**mission **S**pectroscopy) beam line [128]. A bulk franckeite crystal was analyzed at ANTARES, cleaved in an ultra-high vacuum environment (5×10^{-10} Torr) to present a clean surface for analysis. A Fresnel zone plate at the ANTARES beamline was used to focus the incident photon beam to a 120 nm spot size, ideal for measuring photoemission from a single domain in a polycrystalline bulk franckeite sample. A five-axis stage was used to scan the franckeite sample under the photon beam, adjusting position and angular orientation to identify a suitable crystalline domain. The high resistivity of franckeite which increases as temperature decreases (discussed further below), required measurement at room temperature to mitigate against sample charging.

ARPES spectra of franckeite were acquired at a photon energy of $h\nu = 100$ eV, an approximate photon flux of 10^{10} photons/sec/0.01% BW, with electron kinetic energy $E_{kin} = 86 - 96$ eV measured by a Scienta R4000 analyzer, presented in Figure 5.5. ARPES is a

measure of occupied electronic states, from which the presence of a valence band alone indicates that the franckeite surface is p-type. Even with the evidently low signal-to-noise ratio, which we attribute to a combination of low photon flux and low photoemission yield, we resolve an anisotropic valence band, with two valleys separated by a saddle point. The dispersion of E versus \mathbf{k} along the marked cuts 1, 2, and 3 are given in Figure 5.5.

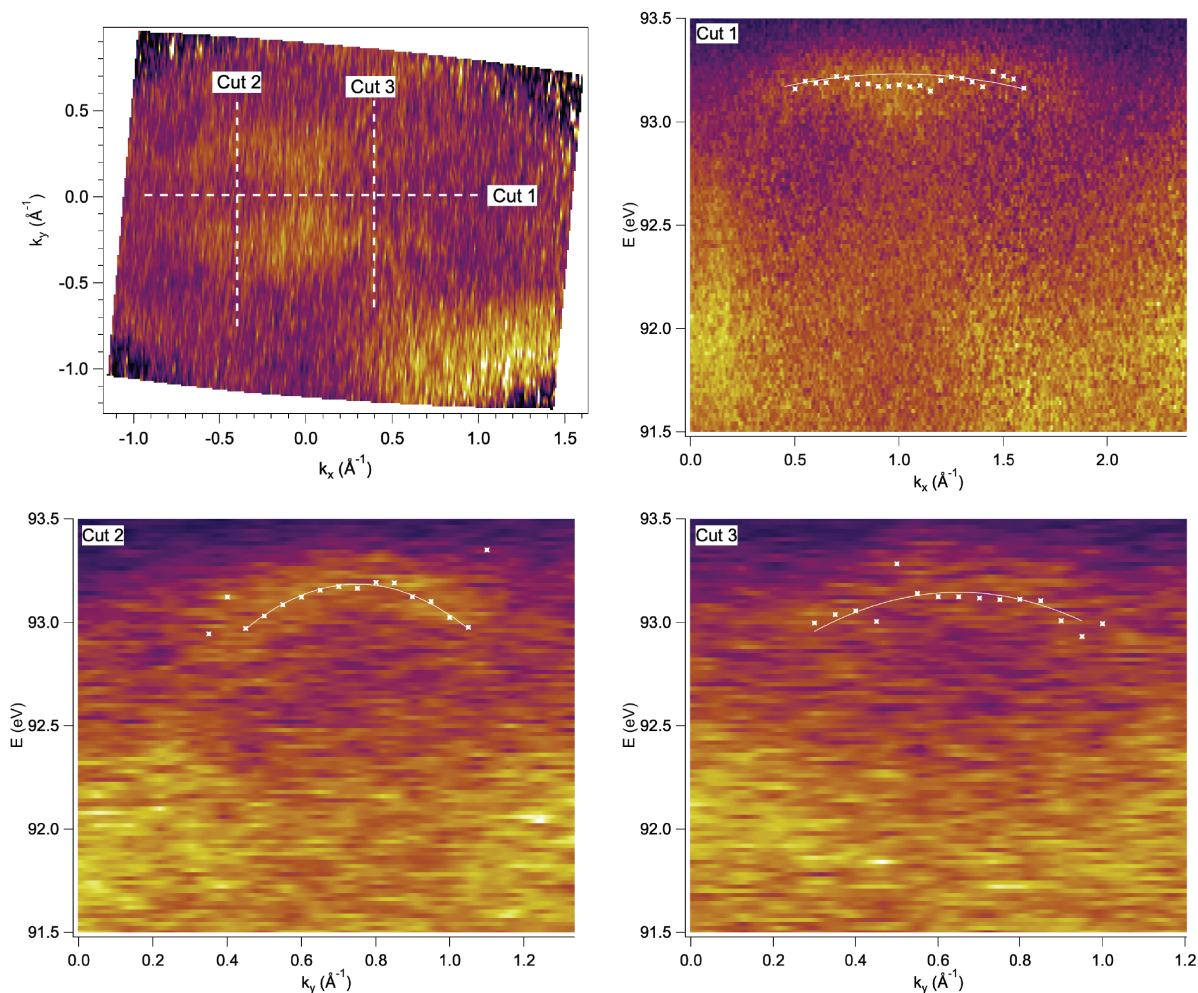


Figure 5.5: Franckeite ARPES. The slices along three different cuts are shown. Effective mass is extracted from the parabolic fits to the observed bands.

Effective masses are extracted from parabolic fits to the bands along these cuts using equation 5.4.

$$E = E_0 - \frac{\hbar^2}{2m^*}(k - k_0)^2 \quad (5.4)$$

where E_0 is the maxima of the parabola and k_0 is the corresponding momentum at the local band maximum. From the fits, the in-plane effective masses along cuts 1, 2 and 3 are found to be $19.1m_0$, $1.6m_0$ and $2.5m_0$, respectively. According to DFT calculations [116], the observed valence band states are attributable to the H-layer.

5.2 Reflectance Hyperspectra of Exfoliated Franckeite

5.2.1 Atomic Force Microscopy

To study the optical properties of franckeite, we prepared franckeite flakes using mechanical exfoliation. The flakes were exfoliated onto a silicon substrate with a 300 nm SiO₂ layer, using Nitto Denko thermal release tape. Our selection process specifically focused on flakes featuring diverse thickness regions, enabling an investigation into thickness dependent optical reflection. An optical microscopy image of representative exfoliated flakes is provided in Figure 5.6.

To quantify thickness variations in the exfoliated flakes, atomic force microscopy (AFM) was employed. We acquired AFM images of the flakes using the dynamic force mode of the Nanosurf FlexAFM system. The average thickness of the different plateaus, indicated with

different colour discs in Figure 5.6, were determined by calculating the average height over the plateau region relative to the substrate.

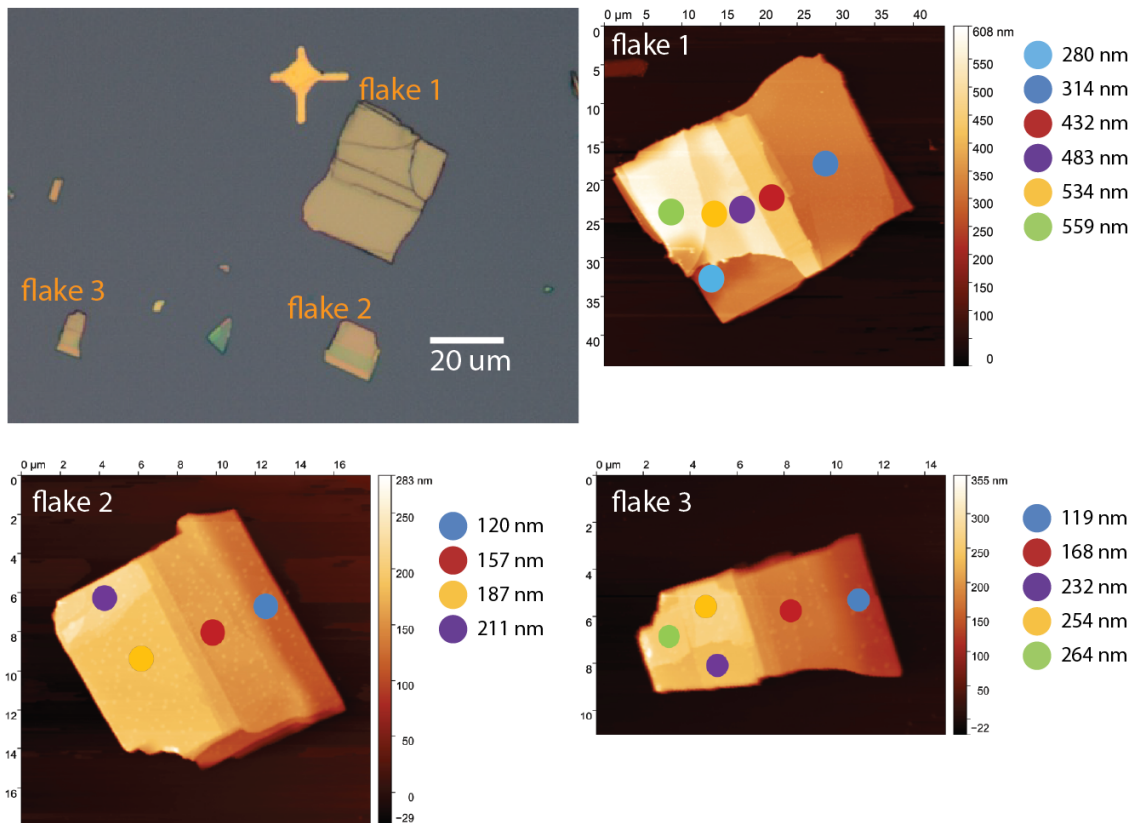


Figure 5.6: Optical microscopy and AFM images of exfoliated franckeite. The average thickness of the different plateaus of the flakes are shown.

5.2.2 Optical Reflection Spectroscopy

Hyperspectral imaging is a powerful tool for the analysis of optical properties of materials. It provides spectral signatures for each spatial location within the imaged sample area by either raster scanning or wavelength scanning. In the wavelength scanning method, volume

Bragg tunable filters are utilized to capture monochromatic images at a multitude of narrow (2-5 nm), contiguous spectral bands across the spectrum [129]. The output is a three-dimensional dataset known as a hyperspectral datacube which encapsulates spatial information along two dimensions and spectral information along the third dimension.

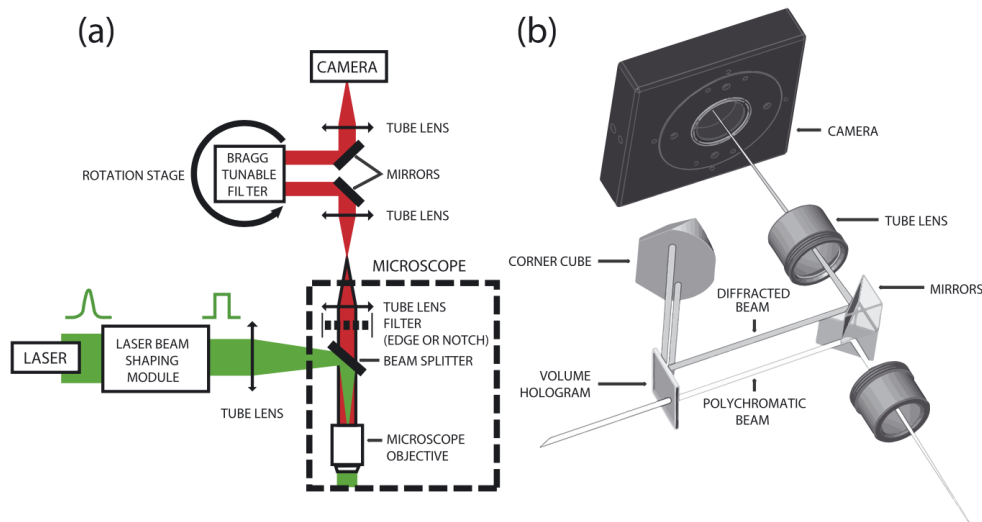


Figure 5.7: a) Schematic of a hyperspectral imaging system integrated with Raman spectroscopy. This system is analogous to the reflection hyperspectral imaging system that was used in our experiments. In our experiments, Raman laser source was replaced with a white light source. b) Design of the imaging Bragg tunable filter. Reprinted with permission from Ref [130].

Reflection hyperspectral imaging of our franckeite samples were carried out at Photon etc. using an IMA hyperspectral imaging system (analogous to the RIMA system shown in Figure 5.7) with a 50x objective giving 1 μm spatial resolution, over the wavelength range $\lambda = 400 - 1000$ nm with 2 nm spectral resolution. The hyperspectral images of reflected light intensity at 4 different representative wavelengths are illustrated in Figure 5.8, where

the reflection intensity of different franckeite plateaus is seen to be wavelength dependent.

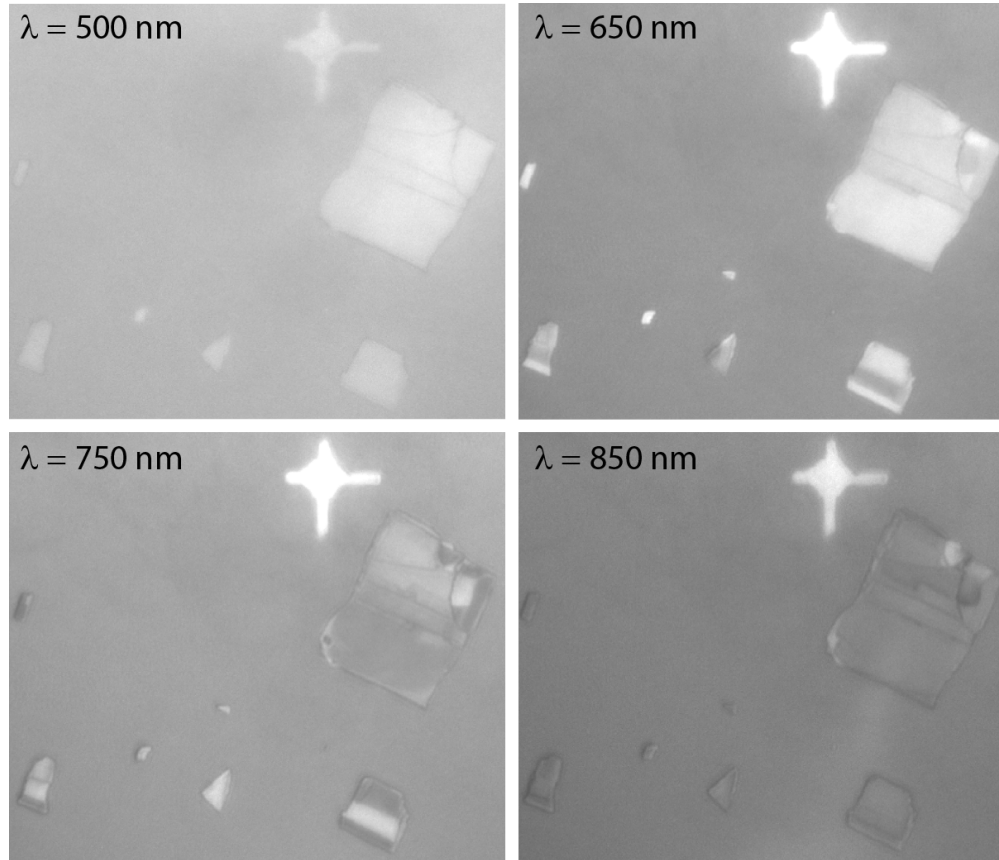


Figure 5.8: Reflection hyperspectra images of exfoliated franckeite acquired using Photon etc. IMA microscope at various representative wavelengths.

The intensity of light at wavelength λ reflected from the franckeite flakes $I_f(\lambda)$ and from the substrate $I_s(\lambda)$, can be expressed as,

$$I_s(\lambda) = R_s(\lambda)I_0(\lambda) \quad (5.5a)$$

$$I_f(\lambda) = R_f(\lambda)I_0(\lambda). \quad (5.5b)$$

where, $R_s(\lambda)$ and $R_f(\lambda)$ are the reflectivity of the substrate and franckeite flakes, respectively. $I_0(\lambda)$ is the optical reference intensity including the wavelength dependence of the power spectral density of the light source, and the wavelength dependence of instrument response, including the grating and photodetector response. In order to remove the spectral features of the measurement instrument, we work with the reflection contrast, $C(\lambda)$, defined similarly to Ref [131].

$$C(\lambda) = \frac{I_f(\lambda) - I_s(\lambda)}{I_s(\lambda)} \quad (5.6)$$

Using the reflection contrast, we extract the franckeite reflectivity $R_f(\lambda)$ using the theoretical calculated optical response of the Si/SiO₂ substrate R_{s0} .

$$R_f(\lambda) = R_{s0}(\lambda)(C(\lambda) + 1) \quad (5.7)$$

Here, $R_{s0}(\lambda)$ is calculated using the thin film Fresnel reflection coefficient for the substrate [132] and the measured Si [133] and SiO₂ [134] refractive indices. This process ensures that the calculated franckeite reflectivity $R_f(\lambda)$ is free from instrument related spectral variations. The calculated reflectivity $R_f(\lambda)$ for each flake is given in Figure 5.9 where each trace represents the reflectivity calculated using the average contrast from plateaus of the flake. A transition from absorption dominated response, where reflectivity is independent of plateau thickness, to interference dominated response, where oscillatory reflectivity is thickness dependent, occurs near 620 – 650 nm for all plateaus. This transition corresponds

to a direct optical absorption edge and direct optical band-gap at $\hbar\omega = E_g = 1.91 - 2.0$ eV, in agreement with previous observations at $\hbar\omega = 1.97 - 2.1$ eV in PL experiments [117]. The observed direct optical band gap is attributed to optical transitions in the H-layer.

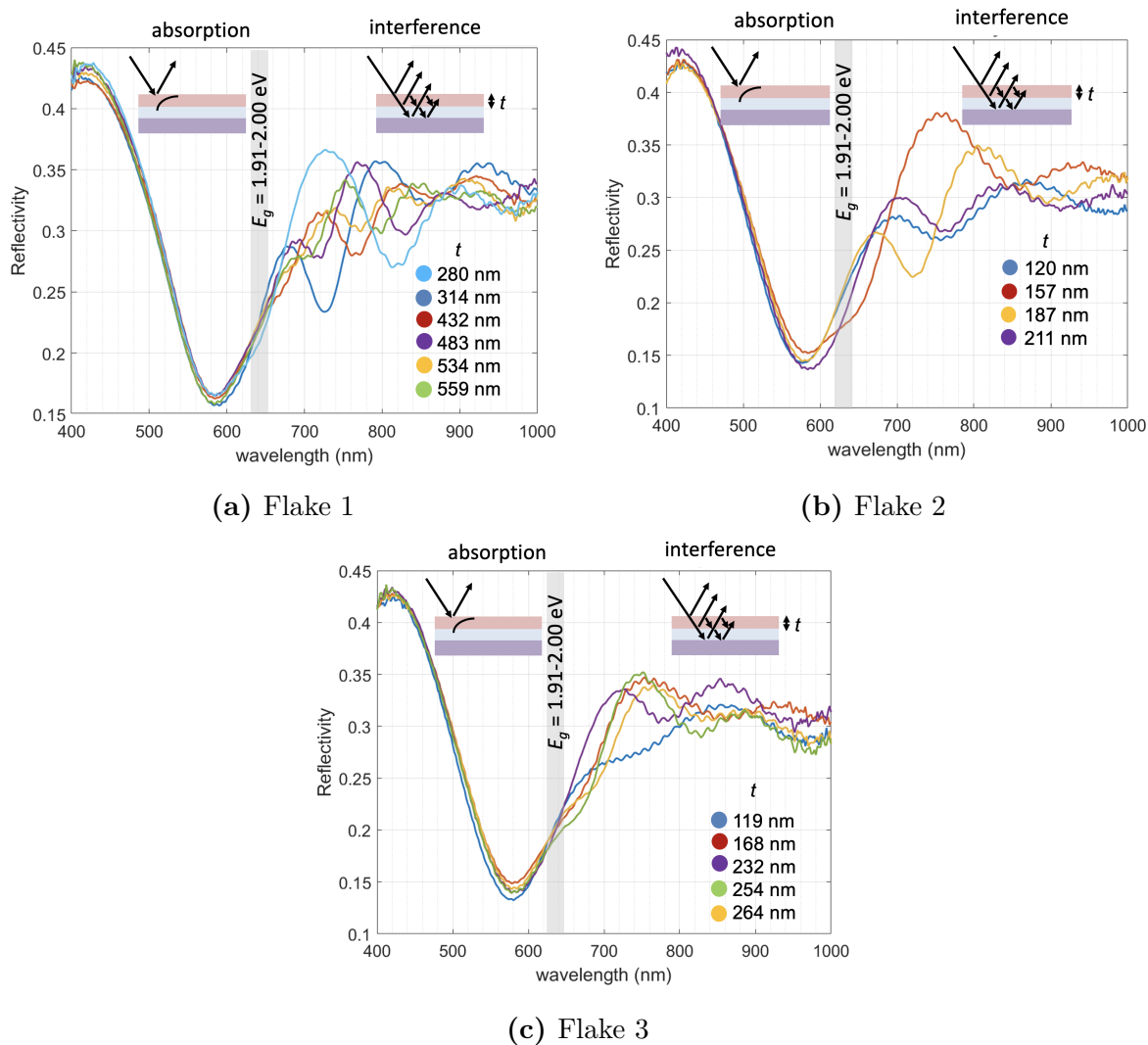


Figure 5.9: Reflectivity with respect to wavelength is presented for three different flakes. The AFM images of the corresponding flakes are given in Figure 5.6. The coloured traces represent regions of the flake with thickness t .

5.3 Thermoelectric Effect in Exfoliated Franckeite

Finally, thermoelectric transport measurements were conducted on franckeite to complement electronic structure and optical absorption measurements. Franckeite flakes were mechanically exfoliated on a Si substrate with a 300 nm SiO₂ layer using Nitto Denko thermal release tape. Electrical contacts were placed near the flake in a similar geometry utilized in previous thermoelectric measurements of 2D materials [135, 136]. An optical microscopy image of a thermoelectric franckeite device is shown in Figure 5.11. In this setup, one metallic strip placed near the flake is used as an electrical heater to create a temperature gradient along the franckeite flake. Two metallic strips on both ends of the flake are utilized as thermometers. By measuring the 4-point resistance across these thermometer strips, the local temperature can be deduced.

The heater, thermometers and franckeite contacts were defined using electron beam lithography conducted with a Raith e-Line system. A polymethylmethacrylate (PMMA) in anisole at 4 wt % (A4) electron beam resist was patterned at an acceleration voltage of 20 kV using an areal dose of 280 $\mu\text{C}/\text{cm}^2$ for finer features and 160 $\mu\text{C}/\text{cm}^2$ for larger features. After exposure, samples were developed using a 1:3 mixture of isopropyl alcohol and methyl isobutyl ketone. 50/50 nm Pd/Au contacts were evaporated on the samples, followed by a standard acetone lift-off process.

The two point resistances across franckeite contacts were in the 1.6 – 2.1 M Ω range at room temperature in our devices. In temperature dependent franckeite resistivity

measurements, we observed insulating behaviour in franckeite at low temperatures as shown in Figure 5.10. The insulating behaviour is attributed to charge carrier freeze out indicating that the franckeite is non-degenerately doped, in contrast to the DFT calculations presented in [114, 116]. The insulating behaviour also explains the surface charging that precluded low temperature ARPES measurements.

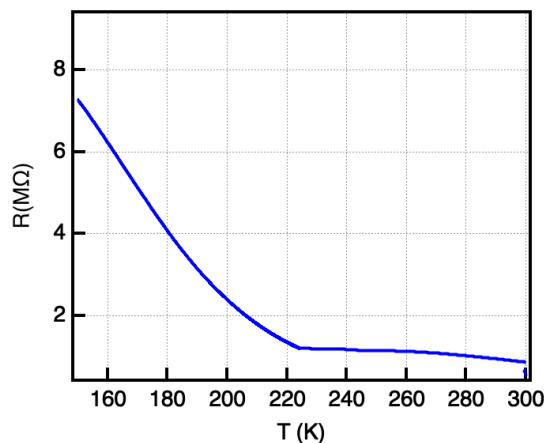


Figure 5.10: Temperature dependence of franckeite resistance. 2 point resistance measured by lock-in amplifier at ≈ 13 Hz, demonstrating insulating behaviour.

Before thermopower experiments, thermometer resistances were calibrated. During the simple calibration procedure, 4-point resistances of the thermometers are recorded as the sample temperature is changed from room temperature to 40 °C using a hot-plate. A linear dependence of the thermometer resistances with temperature is observed. Typical thermometer resistance changes with temperature were 1.7 – 2.3% per K. Following calibration experiments, the open-circuit voltage between two franckeite electrodes and the

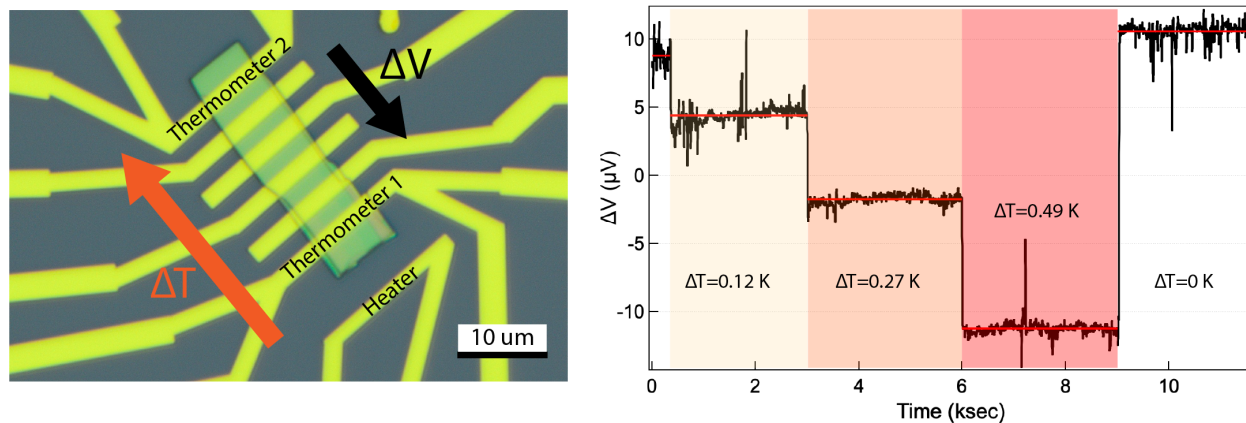


Figure 5.11: Thermoelectric experiments of exfoliated franckeite. Left panel shows the optical microscopy image of a franckeite device prepared for thermoelectric measurements. Right panel shows the voltage pick-up across franckeite contacts at different temperature gradients created by applying 4, 6 and 8 mA to the heater.

4-point resistances of the thermometers were measured while a high current was applied to the heater strip. Figure 5.11 shows the measured voltage across franckeite contacts at different heater currents from 0 to 8 mA. The resulting temperature gradient at each heater current level, is calculated assuming a linear temperature gradient across the sample. At heater current levels of 4, 6 and 8 mA, the temperature gradient between franckeite contacts is calculated as 0.12, 0.27 and 0.49 K, respectively. Comparing the open circuit voltage versus temperature change, the Seebeck coefficient is then,

$$S = -\frac{\Delta V}{\Delta T} = +45 \mu\text{V/K}. \quad (5.8)$$

The sign of the induced voltage and the Seebeck coefficient confirms the intrinsic p-type carriers in franckeite, in agreement with previous studies [114, 118]. The magnitude of the franckeite Seebeck coefficient is significantly lower than the Seebeck coefficients of its constituent compounds, +3200 $\mu\text{V}/\text{K}$ for PbS [122] and -200 $\mu\text{V}/\text{K}$ for SnS₂ [123]. Our findings indicate that despite predictions that quantum confinement in superlattice structures can greatly enhance Seebeck coefficient as noted in the seminal work of Hicks and Dresselhaus [120], such an enhancement is not evident in franckeite. We hypothesize that disorder and its influence on both electron and phonon transport contributes to the modest Seebeck coefficient and notes that thermoelectric effect in disordered systems remains challenging to describe theoretically [137]. Interestingly, in misfit layer compounds with alternating n and p layers similar to franckeite, the low Seebeck coefficient observed was ascribed to the counteractive effects of the n and p layers on the overall contribution to the Seebeck coefficient [138]. While ARPES reveals strictly p-type character, ARPES is a surface sensitive technique which may not reveal the doping state of the interior of the material. Further experimental work is required to elucidate these questions.

5.4 Conclusion

We offer an examination of franckeite's structural properties, reflectivity and thermoelectric performance. We provide insights into the atomic ordering within the Q and H layers, backed by evidence from STEM and APT measurements. The findings suggest

ordered placement of the substitutional defects in the Q and H layers. The effects of this ordering on the band structure of franckeite is still an open question. The band structure of franckeite was probed with ARPES and we resolve an anisotropic two-valley valence band. The in-plane effective mass values are reported as 19.1 and 1.6 m_0 . Optical reflection spectroscopy of franckeite flakes with different thicknesses have been presented. A transition from absorption dominated response to interference dominated response occurs near 620 – 650 nm, corresponding to a direct optical absorption edge near a band-gap $E_g = 1.91 - 2.0$ eV in agreement with previous observations at $\hbar\omega = 1.97 - 2.1$ eV in PL experiments [117].

Thermoelectric measurements of exfoliated franckeite flakes reveal a Seebeck coefficient of $S = +45$ $\mu\text{V}/\text{K}$. We confirm the intrinsic p-type carriers in franckeite, in agreement with previous studies [114, 118]. The estimated Seebeck coefficient is significantly lower than the Seebeck coefficients of franckeite's constituent compounds, +3200 $\mu\text{V}/\text{K}$ for PbS [122] and -200 $\mu\text{V}/\text{K}$ for SnS₂ [123]. Further investigations to understand the origin of the modest Seebeck coefficient of franckeite is required.

Chapter 6

Conclusions and Future Work

In the first part of this bipartite thesis we have demonstrated a comparatively facile method utilizing an inert glove box environment for doping graphene to a high charge carrier density by encapsulating an alkali vapour source in a flip-chip assembly. The flip-chip method permits in-situ charge transport characterization during alkali doping, and enables further experimental characterization by methods such as magnetotransport and Raman spectroscopy. Using this method, monolayer graphene samples were doped up to electron densities of $4 \times 10^{14} \text{ cm}^{-2}$ outside of a UHV environment, which exceeds previous reports. We presented electronic transport and non-resonant Raman spectroscopy measurements of ultra-high doped graphene on quartz substrate, complementing previous ARPES studies of highly doped systems on metallic substrates.

The charge transport properties of highly doped graphene at the Lifshitz transition has

not been fully investigated despite predictions of non-trivial many-body phenomena [82]. We anticipate our method to enable studies of graphene at the Lifshitz transition. Higher doping densities may be achieved by using different species of adsorbates, for example Ca, which donates more electrons per adatom compared to Cs. Sample cleaning following microfabrication may be improved to provide a cleaner surface for dopants to promote more efficient doping. A bilayer graphene device may prove to be a better host material, due to the ability of alkali dopants to intercalate in between graphene layers, resulting in higher doping densities per monolayer. Lastly, the effect of the glovebox environment is yet to be investigated. Using an Ar environment instead of N_2 , may improve the inertness of the environment resulting in better doping conditions.

The flip-chip method is highly versatile. The extension of the flip-chip method to other dopants and target materials and devices may provide a new means of exploring the physics of highly doped low-dimensional systems. For example, heavily doped black phosphorus have been shown to exhibit band-gap modulation, closure, and inversion owing to an unusually strong Stark effect [108, 109]. Real-time doping experiments of black phosphorus and characterization of heavy doped black phosphorus might provide a better understanding of such effects. Alkali doped C_{60} have been proposed as high critical temperature superconductor [110]. The effect of higher carrier densities in the critical temperature of this superconductor is yet to be seen. In a similar fashion, carbon nanotube devices can be heavily doped using the flip-chip method to explore rich physics present in

one dimensional systems. In terms of commercial applications, the flip-chip method can be potentially implemented to dope microfabricated ion traps designed for quantum computing [111].

The second part of this thesis presents the experimental characterization of several electronic properties of franckeite. We offer a comprehensive examination of franckeite's structural properties and provide insights into the atomic ordering within the Q and H layers, backed by evidence from STEM and APT measurements. The findings suggest ordered placement of the substitutional defects in the Q and H layers. The effects of this ordering on the band structure of franckeite is an open question. Computational simulations using Density Functional Theory (DFT) to consider factors such as displacive modulation, appropriate commensurate supercell dimensions, and orderly interstitial defects are yet to be conducted. Notably, the potential ordering of Fe substitutionals within the H layer might unveil magnetic properties that have not been experimentally demonstrated to date.

Angle-resolved photoemission spectroscopy (ARPES) measurements of the band structure reveal an anisotropic two-valley valence band with in-plane effective mass values, 19.1 and 1.6 m_0 . Our initial attempts using bulk franckeite were hindered by challenges stemming from charging effects and surface unevenness, rendering the acquisition of results challenging. A more promising avenue might involve repeating the ARPES experiments using exfoliated crystals.

Optical reflection spectroscopy of franckeite flakes with different thicknesses have been presented. A transition from absorption dominated response to interference dominated response occurs near 620 – 650 nm, corresponding to a direct optical absorption edge near a band-gap $E_g = 1.91 - 2.0$ eV in agreement with previous observations at $\hbar\omega = 1.97 - 2.1$ eV in PL experiments [117]. Further analysis of thickness dependent reflectivity may reveal refractive index estimations of franckeite.

Thermoelectric measurements of exfoliated franckeite flakes reveal a Seebeck coefficient of $S = +45$ $\mu\text{V}/\text{K}$. We confirm the intrinsic p-type carriers in franckeite, in agreement with previous studies [114, 118]. The estimated Seebeck coefficient is significantly lower than the Seebeck coefficients of franckeite's constituent compounds, +3200 $\mu\text{V}/\text{K}$ for PbS [122] and -200 $\mu\text{V}/\text{K}$ for SnS₂ [123]. This result comes as a surprise, since Hicks and Dresselhaus predicted that multiple quantum well structures should deliver enhanced thermoelectric performance [120] and franckeite superlattice is analogous to a multiple quantum well structure. According to DFT results, HOMO and LUMO bands in franckeite are confined to alternating layers [114, 116], meaning Q and H layers are n- and p-type doped, respectively. In misfit layer compounds with alternating pattern of n and p layers similar to franckeite, the low Seebeck coefficient was ascribed to the counteractive effects of the n and p layers on the overall contribution to the Seebeck coefficient [138].

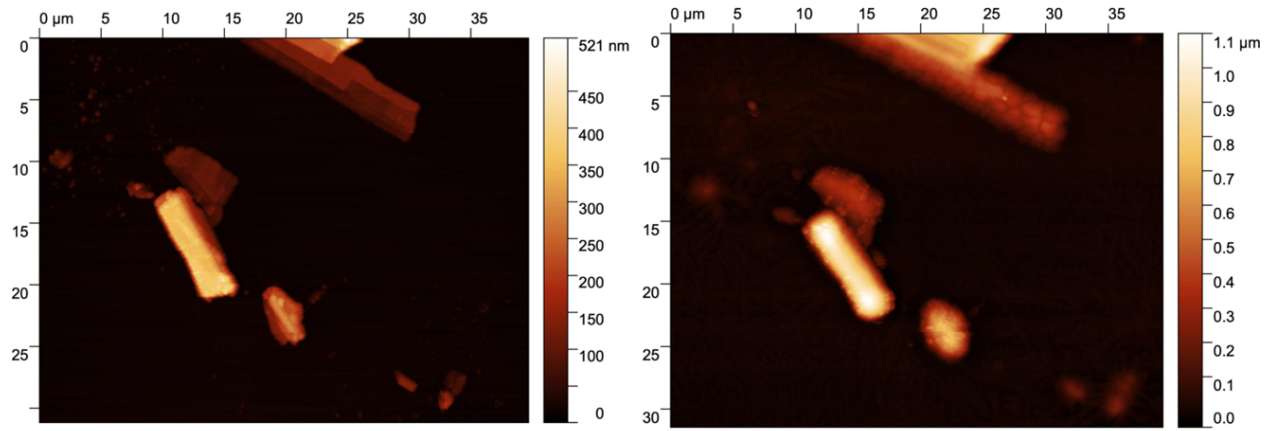


Figure 6.1: AFM images of exfoliated franckeite flakes before (left) and after (right) Cs exposure

The introduction of dopants into franckeite could offer a potential strategy to reduce resistivity, leading to potential enhancements in thermoelectric performance. The van der Waals structure of franckeite is suitable for intercalation. Nevertheless, our initial attempts to introduce Cs dopants into franckeite using the flip-chip method did not yield successful outcomes. As depicted in Figure 6.1, we present atomic force microscopy (AFM) images of exfoliated franckeite flakes both before and after exposure to Cs. Notably, we observed an overall increase in flake thickness, which could imply the intercalation of Cs between the franckeite layers. Regrettably, we also observed a deterioration in the crystal structure. The previous distinct layered structure of the franckeite plateaus appeared to transform into islands of deposits, suggesting an unintended reaction between Cs and franckeite. Further research into alternative dopant species that would intercalate in between franckeite layers is required. The results emphasize the need for further research on

alternative dopant species that could intercalate between the franckeite layers and improve the electronic and thermoelectric performance. The potential unique properties that comes with intercalated franckeite, due to increased interlayer spacing and ordered dopant layers are yet to be discovered.

Bibliography

- [1] Geim, A. K. & Novoselov, K. S. The rise of graphene. *Nature Materials* **6**, 183–91 (2007).
- [2] Grasso, V. *Electronic Structure and Electronic Transitions in Layered Materials*. Physics and Chemistry of Materials with Layered Structures (Springer Dordrecht, 1986).
- [3] Lieth, R. M. A. *Preparation and Crystal Growth of Materials with Layered Structures*. Physics and Chemistry of Materials with Layered Structures (Springer Dordrecht, 1977).
- [4] Wieting, T. J. & Schlüter, M. *Electrons and Phonons in Layered Crystal Structures*. Physics and Chemistry of Materials with Layered Structures (Springer Dordrecht, 1979).
- [5] Guo, B., Xiao, Q., Wang, S. & Zhang, H. 2D layered materials: Synthesis, nonlinear optical properties, and device applications. *Laser and Photonics Reviews* **13** (2019).

-
- [6] Novoselov, K. S. *et al.* Electric field effect in atomically thin carbon films. *Science* **306**, 666–669 (2004).
- [7] Moon, J. Y. *et al.* Layer-engineered large-area exfoliation of graphene. *Science Advances* **6** (2020).
- [8] Li, Z. *et al.* Mechanisms of liquid-phase exfoliation for the production of graphene. *ACS Nano* **14**, 10976–10985 (2020).
- [9] Wang, L. *et al.* One-dimensional electrical contact to a two-dimensional material. *Science* **342**, 614–7 (2013).
- [10] Fang, H. *et al.* High-performance single layered WSe₂ p-FETs with chemically doped contacts. *Nano Letters* **12**, 3788–92 (2012).
- [11] Liu, C. *et al.* Small footprint transistor architecture for photoswitching logic and in situ memory. *Nature Nanotechnology* **14**, 662–667 (2019).
- [12] Desai, S. B. *et al.* MoS₂ transistors with 1-nanometer gate lengths. *Science* **354**, 99–102 (2016).
- [13] Liu, L. *et al.* Ultrafast non-volatile flash memory based on van der Waals heterostructures. *Nature Nanotechnology* **16**, 874–881 (2021).
- [14] Wu, L. *et al.* Atomically sharp interface enabled ultrahigh-speed non-volatile memory devices. *Nature Nanotechnology* **16**, 882–887 (2021).

-
- [15] Jiang, J., Xu, L., Qiu, C. & Peng, L. M. Ballistic two-dimensional InSe transistors. *Nature* **616**, 470–475 (2023).
- [16] Li, W. *et al.* Uniform and ultrathin high- κ gate dielectrics for two-dimensional electronic devices. *Nature Electronics* **2**, 563–571 (2019).
- [17] Ge, J. F. *et al.* Superconductivity above 100 K in single-layer FeSe films on doped SrTiO₃. *Nature Materials* **14**, 285–9 (2015).
- [18] Mak, K. F., Lee, C., Hone, J., Shan, J. & Heinz, T. F. Atomically thin MoS₂: A new direct-gap semiconductor. *Physical Review Letters* **105**, 136805 (2010).
- [19] Zhang, W. *et al.* Ultrahigh-gain photodetectors based on atomically thin graphene-MoS₂ heterostructures. *Scientific Reports* **4**, 3826 (2014).
- [20] Nassiri Nazif, K. *et al.* High-specific-power flexible transition metal dichalcogenide solar cells. *Nature Communications* **12**, 7034 (2021).
- [21] Li, L. *et al.* Direct observation of the layer-dependent electronic structure in phosphorene. *Nature Nanotechnology* **12**, 21–25 (2017).
- [22] Liu, Y. *et al.* Gate-tunable giant stark effect in few-layer black phosphorus. *Nano Letters* **17**, 1970–1977 (2017).
- [23] Deng, Y. *et al.* Gate-tunable room-temperature ferromagnetism in two-dimensional Fe₃GeTe₂. *Nature* **563**, 94–99 (2018).

- [24] Fakih, I. *et al.* Large area graphene ion sensitive field effect transistors with tantalum pentoxide sensing layers for Ph measurement at the nernstian limit. *Applied Physics Letters* **105** (2014).
- [25] Schedin, F. *et al.* Detection of individual gas molecules adsorbed on graphene. *Nature Materials* **6**, 652–5 (2007).
- [26] Parret, R. *et al.* In situ Raman probing of graphene over a broad doping range upon rubidium vapor exposure. *ACS nano* **7**, 165–173 (2013).
- [27] Kühne, M. *et al.* Ultrafast lithium diffusion in bilayer graphene. *Nature Nanotechnology* **12**, 895 (2017).
- [28] McChesney, J. L. *et al.* Extended van Hove singularity and superconducting instability in doped graphene. *Physical Review Letters* **104**, 136803 (2010).
- [29] Lee, D. *et al.* Remote modulation doping in van der Waals heterostructure transistors. *Nature Electronics* **4**, 664–670 (2021).
- [30] Chang, L. L., Esaki, L., Howard, W. E. & Ludeke, R. The growth of a GaAs–GaAlAs superlattice. *Journal of Vacuum Science and Technology* **10**, 11–16 (1973).
- [31] Esaki, L. Long journey into tunneling. *Science* **183**, 1149–55 (1974).
- [32] Schomburg, E. *et al.* Millimeter wave oscillator based on a quasiplanar superlattice electronic device. *Applied Physics Letters* **71**, 401–403 (1997).

- [33] Winnerl, S. *et al.* A GaAs/AlAs superlattice autocorrelator for picosecond thz radiation pulses. *Superlattices and Microstructures* **25**, 57–60 (1999).
- [34] Faist, J. *et al.* Quantum cascade laser. *Science* **264**, 553–6 (1994).
- [35] Taniguchi, T. *et al.* High thermoelectric power factor realization in Si-rich SiGe/Si superlattices by super-controlled interfaces. *ACS Applied Materials and Interfaces* **12**, 25428–25434 (2020).
- [36] Ryu, Y. K., Frisenda, R. & Castellanos-Gomez, A. Superlattices based on van der Waals 2D materials. *Chemical Communications* **55**, 11498–11510 (2019).
- [37] Masubuchi, S. *et al.* Autonomous robotic searching and assembly of two-dimensional crystals to build van der Waals superlattices. *Nature Communications* **9**, 1413 (2018).
- [38] Vishwanath, S. *et al.* Controllable growth of layered selenide and telluride heterostructures and superlattices using molecular beam epitaxy. *Journal of Materials Research* **31**, 900–910 (2016).
- [39] Zhao, B. *et al.* High-order superlattices by rolling up van der Waals heterostructures. *Nature* **591**, 385–390 (2021).
- [40] Makovicky, E. & Hyde, B. G. Non-commensurate (misfit) layer structures. In *Inorganic Chemistry*, 101–170 (Springer Berlin Heidelberg, 1974).

- [41] Dresselhaus, M. S. & Dresselhaus, G. Intercalation compounds of graphite. *Advances in Physics* **30**, 139–326 (1981).
- [42] Wan, C. *et al.* Ultrahigh thermoelectric power factor in flexible hybrid inorganic-organic superlattice. *Nature Communications* **8**, 1024 (2017).
- [43] Li, Q. *et al.* Discrete graphitic crystallites promise high-rate ion intercalation for KC_8 formation in potassium ion batteries. *Advanced Energy Materials* **12** (2022).
- [44] Xiong, P., Ma, R. Z., Sakai, N., Nurdiwijayanto, L. & Sasaki, T. Unilamellar metallic MoS_2 /graphene superlattice for efficient sodium storage and hydrogen evolution. *ACS Energy Letters* **3**, 997–1005 (2018).
- [45] Li, G. *et al.* Observation of van Hove singularities in twisted graphene layers. *Nature Physics* **6**, 109–113 (2009).
- [46] Cao, Y. *et al.* Unconventional superconductivity in magic-angle graphene superlattices. *Nature* **556**, 43–50 (2018).
- [47] Dean, C. R. *et al.* Hofstadter’s butterfly and the fractal quantum hall effect in moire superlattices. *Nature* **497**, 598–602 (2013).
- [48] Novoselov, K. S. Nobel lecture: Graphene: Materials in the flatland. *Reviews of Modern Physics* **83**, 837–849 (2011).

- [49] Geim, A. K. Nobel lecture: Random walk to graphene. *Reviews of Modern Physics* **83**, 851–862 (2011).
- [50] Wallace, P. R. The band theory of graphite. *Physical Review* **71**, 622–634 (1947).
- [51] Slonczewski, J. C. & Weiss, P. R. Band structure of graphite. *Physical Review* **109**, 272–279 (1958).
- [52] Grüneis, A. *et al.* Tight-binding description of the quasiparticle dispersion of graphite and few-layer graphene. *Physical Review B* **78**, 205425 (2008).
- [53] Novoselov, K. S. *et al.* Two-dimensional gas of massless Dirac fermions in graphene. *Nature* **438**, 197–200 (2005).
- [54] Sarma, S. D., Adam, S., Hwang, E. & Rossi, E. Electronic transport in two-dimensional graphene. *Reviews of Modern Physics* **83**, 407 (2011).
- [55] Yu, P. Y. & Cardona, M. *Fundamentals of Semiconductors*. Graduate Texts in Physics (2010).
- [56] Ariel, V. & Natan, A. Electron effective mass in graphene (2012).
- [57] Kittel, C. *Introduction to Solid State Physics* (John Wiley & Sons, 2004), 8 edn.
- [58] Ping, J. *et al.* Disorder-induced magnetoresistance in a two-dimensional electron system. *Phys Rev Lett* **113**, 047206 (2014).

-
- [59] Martin, J. *et al.* Observation of electron–hole puddles in graphene using a scanning single-electron transistor. *Nature Physics* **4**, 144–148 (2007).
- [60] Bergmann, G. Weak localization in thin-films - a time-of-flight experiment with conduction electrons. *Physics Reports* **107**, 1–58 (1984).
- [61] Hikami, S., Larkin, A. I. & Nagaoka, Y. Spin-orbit interaction and magnetoresistance in the two dimensional random system. *Progress of Theoretical Physics* **63**, 707–710 (1980).
- [62] McCann, E. *et al.* Weak-localization magnetoresistance and valley symmetry in graphene. *Physical Review Letters* **97**, 146805 (2006).
- [63] Fal'ko, V. I. *et al.* Weak localization in graphene. *Solid State Communications* **143**, 33–38 (2007).
- [64] Ki, D.-K., Jeong, D., Choi, J.-H., Lee, H.-J. & Park, K.-S. Inelastic scattering in a monolayer graphene sheet: A weak-localization study. *Physical Review B* **78** (2008).
- [65] Morozov, S. V. *et al.* Strong suppression of weak localization in graphene. *Physical Review Letters* **97**, 016801 (2006).
- [66] Tikhonenko, F., Horsell, D., Gorbachev, R. & Savchenko, A. Weak localization in graphene flakes. *Physical Review Letters* **100**, 056802 (2008).

- [67] Tikhonenko, F. V., Kozikov, A. A., Savchenko, A. K. & Gorbachev, R. V. Transition between electron localization and antilocalization in graphene. *Phys Rev Lett* **103**, 226801 (2009).
- [68] Baker, A. M. R. *et al.* Weak localization scattering lengths in epitaxial, and CVD graphene. *Physical Review B* **86** (2012).
- [69] Tikhonenko, F., Horsell, D., Wilkinson, B., Gorbachev, R. & Savchenko, A. The effect of inter-valley scattering on weak localisation in graphene. *Physica E: Low-dimensional Systems and Nanostructures* **40**, 1364–1366 (2008).
- [70] Jorio, A., Dresselhaus, M. S., Saito, R. & Dresselhaus, G. *Raman Spectroscopy in Graphene Related Systems* (John Wiley & Sons, 2011).
- [71] Froehlicher, G. & Berciaud, S. Raman spectroscopy of electrochemically gated graphene transistors: Geometrical capacitance, electron-phonon, electron-electron, and electron-defect scattering. *Physical Review B* **91** (2015).
- [72] Ferrari, A. C. *et al.* Raman spectrum of graphene and graphene layers. *Physica Review Letters* **97**, 187401 (2006).
- [73] Basko, D. M., Piscanec, S. & Ferrari, A. C. Electron-electron interactions and doping dependence of the two-phonon Raman intensity in graphene. *Physical Review B* **80** (2009).

- [74] Das, A. *et al.* Monitoring dopants by Raman scattering in an electrochemically top-gated graphene transistor. *Nat Nanotechnol* **3**, 210–5 (2008).
- [75] Cancado, L. G. *et al.* Quantifying defects in graphene via Raman spectroscopy at different excitation energies. *Nano Lett* **11**, 3190–6 (2011).
- [76] Tuinstra, F. & Koenig, J. L. Raman spectrum of graphite. *The Journal of Chemical Physics* **53**, 1126–1130 (1970).
- [77] Hell, M. G. *et al.* Resonance Raman spectrum of doped epitaxial graphene at the Lifshitz transition. *Nano Letters* **18**, 6045–6056 (2018).
- [78] Lazzeri, M. & Mauri, F. Nonadiabatic Kohn anomaly in a doped graphene monolayer. *Physical Review Letters* **97**, 266407 (2006).
- [79] Kravets, V. *et al.* Spectroscopic ellipsometry of graphene and an exciton-shifted van Hove peak in absorption. *Physical Review B* **81**, 155413 (2010).
- [80] Mak, K. F., Shan, J. & Heinz, T. F. Seeing many-body effects in single- and few-layer graphene: observation of two-dimensional saddle-point excitons. *Physical Review Letters* **106**, 046401 (2011).
- [81] Mak, K. F. *et al.* Tuning many-body interactions in graphene: The effects of doping on excitons and carrier lifetimes. *Physical Review Letters* **112**, 207401 (2014).

- [82] Profeta, G., Calandra, M. & Mauri, F. Phonon-mediated superconductivity in graphene by lithium deposition. *Nature Physics* **8**, 131–134 (2012).
- [83] Ludbrook, B. *et al.* Evidence for superconductivity in Li-decorated monolayer graphene. *Proceedings of the National Academy of Sciences* **112**, 11795–11799 (2015).
- [84] Nandkishore, R., Levitov, L. S. & Chubukov, A. V. Chiral superconductivity from repulsive interactions in doped graphene. *Nature Physics* **8**, 158–163 (2012).
- [85] Kaganov, M. I. & Lifshits, I. M. Electron theory of metals and geometry. *Soviet Physics Uspekhi* **22**, 904 (1979).
- [86] Ehlen, N. *et al.* Origin of the flat band in heavily Cs-doped graphene. *ACS Nano* **14**, 1055–1069 (2020).
- [87] Rosenzweig, P., Karakachian, H., Marchenko, D., Küster, K. & Starke, U. Overdoping graphene beyond the van Hove singularity. *Physical Review Letters* **125**, 176403 (2020).
- [88] Zaarour, A. *et al.* Flat band and Lifshitz transition in long-range-ordered supergraphene obtained by erbium intercalation. *Physical Review Research* **5**, 013099 (2023).
- [89] Bao, C. *et al.* Coexistence of extended flat band and kekulé order in Li-intercalated graphene. *Physical Review B* **105**, L161106 (2022).

-
- [90] Ichinokura, S. *et al.* Van Hove singularity and Lifshitz transition in thickness-controlled Li-intercalated graphene. *Physical Review B* **105**, 235307 (2022).
- [91] Jugovac, M. *et al.* Clarifying the apparent flattening of the graphene band near the van Hove singularity. *Physical Review B* **105**, L241107 (2022).
- [92] Efetov, D. K. & Kim, P. Controlling electron-phonon interactions in graphene at ultrahigh carrier densities. *Physical Review Letters* **105**, 256805 (2010).
- [93] Ye, J. *et al.* Accessing the transport properties of graphene and its multilayers at high carrier density. *Proceedings of the National Academy of Sciences* **108**, 13002–13006 (2011).
- [94] Chen, C. F. *et al.* Controlling inelastic light scattering quantum pathways in graphene. *Nature* **471**, 617–20 (2011).
- [95] Kühne, M. *et al.* Reversible superdense ordering of lithium between two graphene sheets. *Nature* **564**, 234–239 (2018).
- [96] Khademi, A. *et al.* Weak localization measurements of electronic scattering rates in Li-doped epitaxial graphene. *Physical Review B* **100**, 161405 (2019).
- [97] Chen, J. H. *et al.* Charged-impurity scattering in graphene. *Nature Physics* **4**, 377–381 (2008).

-
- [98] Adam, S., Hwang, E. H., Galitski, V. M. & Das Sarma, S. A self-consistent theory for graphene transport. *Proceedings of the National Academy of Sciences of the United States of America* **104**, 18392–18397 (2007).
- [99] Chandni, U., Henriksen, E. A. & Eisenstein, J. P. Transport in indium-decorated graphene. *Physical Review B* **91** (2015).
- [100] Elias, J. A. & Henriksen, E. A. Electronic transport and scattering times in tungsten-decorated graphene. *Physical Review B* **95** (2017).
- [101] Ashcroft, N. W. & Mermin, N. D. *Solid State Physics*, (Holt Saunders International, 1976).
- [102] Lau, J. H. Recent advances and new trends in flip chip technology. *Journal of Electronic Packaging* **138** (2016).
- [103] Davis, E. M., Harding, W. E., Schwartz, R. S. & Corning, J. J. Solid logic technology - versatile high-performance microelectronics. *Ibm Journal of Research and Development* **8**, 102–114 (1964).
- [104] P.J.A., M. & R.D., P. Flip-chip semiconductor devices. *Electrical Communication* **41**, 431–437 (1966).
- [105] Wong, C. P., Luo, S. & Zhang, Z. Flip the chip. *Science* **290**, 2269–70 (2000).

- [106] Chen, Y., Yi, H. & Podzorov, V. High-resolution AC measurements of the hall effect in organic field-effect transistors. *Physical Review Applied* **5**, 034008 (2016).
- [107] Pisana, S. *et al.* Breakdown of the adiabatic Born-Oppenheimer approximation in graphene. *Nature Materials* **6**, 198–201 (2007).
- [108] Kim, J. *et al.* Observation of tunable band gap and anisotropic Dirac semimetal state in black phosphorus. *Science* **349**, 723–726 (2015).
- [109] Ehlen, N. *et al.* Direct observation of a surface resonance state and surface band inversion control in black phosphorus. *Physical Review B* **97**, 045143 (2018).
- [110] Zong, L.-N., Wang, R.-S., Peng, D. & Chen, X.-J. Superconductivity in nonstoichiometric rubidium-doped C_{60} . *The Journal of Physical Chemistry C* **126**, 2912–2919 (2022).
- [111] Auchter, S. *et al.* Industrially microfabricated ion trap with 1 eV trap depth. *Quantum Science and Technology* **7** (2022).
- [112] Stelzner, A. W. *Ueber franckeit, ein neues erz aus Bolivia*, 114 (E. Schweizerbart'sche Verlagshandlung, 1893).
- [113] Makovicky, E., Petricek, V., Dusek, M. & Topa, D. The crystal structure of franckeite, $Pb_{21.7}Sn_{9.3}Fe_{4.0}Sb_{8.1}S_{56.9}$. *American Mineralogist* **96**, 1686–1702 (2011).

- [114] Velicky, M. *et al.* Exfoliation of natural van der Waals heterostructures to a single unit cell thickness. *Nature Communications* **8**, 14410 (2017).
- [115] Frisenda, R. *et al.* Symmetry breakdown in franckeite: Spontaneous strain, rippling, and interlayer moire. *Nano Letters* **20**, 1141–1147 (2020).
- [116] Molina-Mendoza, A. J. *et al.* Franckeite as a naturally occurring van der Waals heterostructure. *Nature Communications* **8**, 14409 (2017).
- [117] Z. Costa, V. *et al.* Observation of photoluminescence from a natural van der Waals heterostructure. *Applied Physics Letters* **120** (2022).
- [118] Ray, K. *et al.* Photoresponse of natural van der Waals heterostructures. *ACS Nano* **11**, 6024–6030 (2017).
- [119] Gant, P. *et al.* Optical contrast and refractive index of natural van der Waals heterostructure nanosheets of franckeite. *Beilstein J Nanotechnol* **8**, 2357–2362 (2017).
- [120] Hicks, L. D. & Dresselhaus, M. S. Effect of quantum-well structures on the thermoelectric figure of merit. *Physical Review B* **47**, 12727–12731 (1993).
- [121] Venkatasubramanian, R., Siivola, E., Colpitts, T. & O’Quinn, B. Thin-film thermoelectric devices with high room-temperature figures of merit. *Nature* **413**, 597–602 (2001).

- [122] Pei, Y. L. & Liu, Y. Electrical and thermal transport properties of Pb-based chalcogenides: PbTe, PbSe, and PbS. *Journal of Alloys and Compounds* **514**, 40–44 (2012).
- [123] Lee, M. J. *et al.* Thermoelectric materials by using two-dimensional materials with negative correlation between electrical and thermal conductivity. *Nature Communications* **7**, 12011 (2016).
- [124] Zschiesche, H., Aygar, A. M., Langelier, B., Szkopek, T. & Botton, G. A. Atomic scale chemical ordering in franckeite-a natural van der Waals superlattice. *Journal of Physics: Condensed Matter* **34**, 055403 (2021).
- [125] Larson, D. J., Prosa, T. J., Ulfig, R. M., Geiser, B. P. & Kelly, T. F. *Local Electrode Atom Probe Tomography* (Springer, 2013).
- [126] Goldstein, H. *Classical Mechanics* (Addison-Wesley, 1980).
- [127] Damascelli, A. Probing the electronic structure of complex systems by ARPES. *Physica Scripta* **T109**, 61–74 (2004).
- [128] Avila, J. *et al.* ANTARES, a scanning photoemission microscopy beamline at SOLEIL. *Journal of Physics: Conference Series* **425** (2013).

- [129] Verhaegen, M., Lessard, S. & Blais-Ouellette, S. Narrow band SWIR hyperspectral imaging: a new approach based on volume Bragg grating. *Next-Generation Spectroscopic Technologies V* **8374** (2012).
- [130] Gaufrès, E. *et al.* Hyperspectral Raman imaging using Bragg tunable filters of graphene and other low-dimensional materials. *Journal of Raman Spectroscopy* **49**, 174–182 (2017).
- [131] Blake, P. *et al.* Making graphene visible. *Applied Physics Letters* **91** (2007).
- [132] Diebold, A. & Hofmann, T. *Optical and Electrical Properties of Nanoscale Materials*. Springer Series in Materials Science (Springer, 2021).
- [133] Aspnes, D. E. & Studna, A. A. Dielectric functions and optical parameters of Si, Ge, GaP, GaAs, GaSb, InP, InAs, and InSb from 1.5 to 6.0 eV. *Physical Review B* **27**, 985–1009 (1983).
- [134] Malitson, I. H. Interspecimen comparison of the refractive index of fused silica. *Journal of the Optical Society of America* **55**, 1205–1209 (1965).
- [135] Small, J. P., Perez, K. M. & Kim, P. Modulation of thermoelectric power of individual carbon nanotubes. *Physical Review Letters* **91**, 256801 (2003).
- [136] Zuev, Y. M., Chang, W. & Kim, P. Thermoelectric and magnetothermoelectric transport measurements of graphene. *Physical Review Letters* **102**, 096807 (2009).

-
- [137] Rowe, D. M. *CRC Handbook of Thermoelectrics* (CRC Press, 1995).
- [138] Li, Z. *et al.* Cross-plane Seebeck coefficient measurement of misfit layered compounds $(\text{SnSe})_{(n)}(\text{TiSe}_2)_{(n)}$ ($n = 1,3,4,5$). *Nano Letters* **17**, 1978–1986 (2017).